5-2005

Charge transport measurements of vertically aligned carbon nanofiber

Lan Zhang
University of Tennessee - Knoxville

To the Graduate Council:

I am submitting herewith a dissertation written by Lan Zhang entitled "Charge transport measurements of vertically aligned carbon nanofiber." I have examined the final electronic copy of this dissertation for form and content and recommend that it be accepted in partial fulfillment of the requirements for the degree of Doctor of Philosophy, with a major in Materials Science and Engineering.

Michael L. Simpson, Major Professor

We have read this dissertation and recommend its acceptance:

Douglas H. Lowndes, Anthony J. Pedraza, Syed K. Islam

Accepted for the Council:

Carolyn R. Hodges

Vice Provost and Dean of the Graduate School

(Original signatures are on file with official student records.)

To the Graduate Council:

I am submitting herewith a dissertation written by Lan Zhang entitled "Charge transport measurements of vertically aligned carbon nanofiber." I have examined the final electronic copy of this dissertation for form and content and recommend that it be accepted in partial fulfillment of the requirement for the degree of doctor of Philosophy, with a major in Materials Science and Engineering.

Michael L. Simpson
Major Professor

We have read this dissertation
and recommend its acceptance:

Douglas H. Lowndes

Anthony J. Pedraza

Syed K. Islam

Accepted for the Council:

Anne Mayhew
Vice Chancellor and Dean of Graduate Studies

(Original signatures are on file with official student records.)

Charge transport measurements of vertically aligned carbon nanofibers

A Dissertation

Presented for the

Doctor of Philosophy Degree

The University of Tennessee, Knoxville

Lan Zhang

May 2005

Dedication

This dissertation is dedicated to my family,

especially to my son, Kevin, and my parents-in-law.

Acknowledgements

I am most grateful to my advisor Dr. Michael Simpson for his invaluable advice, support and patience. This work would have never been completed without his guidance. I would also like to thank my committee Dr. Douglas Lowndes, Dr. Anthony Pedraza, and Dr. Syed Islam, for their time, assistance, and valuable suggestions.

I am also deeply indebted to Dr. Vladimir Merkulov, whose fundamental work on carbon nanofibers has provided the opportunity for this work. I would also like to thank Dr. John Caughman of Oak Ridge National Laboratory and Dr. Lance Delzeit of NASA Ames Center for providing carbon nanofiber samples.

I am very grateful to our MENT group members, especially Dr. Anatoli Melechko for his excellent advice and help through the whole work. I would also like to thank Derek Austin for his AFM training and assistance on charge transport measurements, and Kate Klein for her help on TEM and STEM. I would also like to thank Dale Hensley, Richard Kasica, and Darrell Thomas for their help on the clean room use. I am also deeply indebted to Dr. Michael Guillorn, who has left for Cornell Nanofabrication Facility, for his training, invaluable suggestions and most timely help.

I am very thankful to Dr. Rong-Ying Jin for her most important help in the temperature dependence measurements, and Pamela Fleming for her assistance in metal deposition. I would also like to thank Dr. Harry Meyer for the help on AES, and Dr. Larry Allard for TEM training. The administrative support from Dr. Gary Alley, Kathy Martin and Gayle Jones is also appreciated.

In particular, I would like to thank Dr. Laura Morris Edwards, who provided priceless help on my dissertation writing.

Abstract

Vertically aligned carbon nanofibers (VACNFs) have found a variety of electronic applications. To further realize these applications, a good understanding of the charge transport properties is essential. In this work, charge transport properties have been systematically measured for three types of VACNF forests with Ni as catalyst, namely VACNFs grown by direct current PECVD, and inductively coupled PECVD at both normal pressure (3.6 Torr) and low pressure (50 mTorr).

The structure and composition of these nanofibers have also been investigated in detail prior to the charge transport measurements. It has been found that the dc VACNF body consists of three parts: a 10-15 nm thick graphitic outer layer, cross-struts, and a layer with darker contrast in between. Carbon, nitrogen, silicon, nickel and oxygen are all present in the dc VACNF body. Ni is distributed along the entire dc VACNF body, as first reported in this work. Auger electron spectroscopy results indicate that Ni is primarily located in fiber walls, not in the center catalytic part.

Four-probe I-V measurements on individual nanofibers have been enabled by the fabrication of multiple metal ohmic contacts on individual fibers that exhibited resistance of only a few kΩ. An O_2 plasma reactive ion etch method has been used to achieve ohmic contacts between the nanofibers and Ti/Au, Ag/Au, Cd/Au, and Cr/Au electrodes. Dc VACNFs exhibit linear I-V behavior at room temperature, with a resistivity of approximately 4.2×10^{-3} Ω·cm. Gate effect is not observed when the heavily doped Si substrate is used as a back gate. Our measurements are consistent with a dominant transport mechanism of electrons traveling through intergraphitic planes in the dc

VACNFs. The resistivity of these fibers is almost independent of temperature, and the contact resistance decreases as temperature increases.

Further studies reveal that the 10-15 nm thick graphitic outer layer dominates the charge transport properties of dc VACNFs. This is demonstrated by comparison of charge transport properties of as-grown VACNFs and VACNFs with the outer layer partially removed by oxygen plasma reactive ion etch. The linear I-V behavior of the fibers does not vary as this outer layer becomes thinner, but displays a drastic shift to a rectifying behavior when this layer is completely stripped away from some regions of the nanofiber. This shift may be related with the compositional differences in the outer layer and the inner core of the nanofibers. Our results imply that by varying the extent of graphitization and structure of the outer layer, it may be possible to achieve controllable charge transport properties for dc VACNFs.

VACNFs grown by inductively coupled PECVD at normal and low pressure both have a defective outer layer and a more crystalline inner core. The composition of these fibers is predominately carbon, and Ni is not observed along the fiber body. Nitrogen is present possibly as a result of sample storage in air. Two-probe charge transport measurements indicate linear I-V behavior, and the resistivity of both types of inductively coupled PECVD grown VACNFs is on the order of 10^{-3} to 10^{-4} Ω·cm.

Table of contents

Chapter Page

1. Introduction: charge transport properties of carbon nanotubes and related carbon materials ……..1
1.1 Charge transport properties of graphite…….1
1.2 Charge transport properties of carbon nanotubes……..4
1.2.1 Electrical transport measurement techniques for carbon nanotubes……..4
1.2.2 Metallic carbon nanotubes...……10
1.2.3 Semiconducting carbon nanotubes……..11
1.2.4 Temperature dependence of charge transport properties of CNTs……..14
1.3 Charge transport properties of carbon fibers……...15
1.3.1 Different types of carbon fibers……15
1.3.2 Charge transport measurements of carbon fibers……16
1.4 Scope of dissertation……24

2. Growth of vertically aligned carbon nanofibers by plasma-enhanced chemical vapor deposition ……..26
2.1 Various growth techniques of VACNFs……..26
2.1.1 dc PECVD……27
2.1.2 Microwave PECVD……32
2.1.3 Inductively coupled PECVD……33
2.2 VACNF growth mechanisms..……35
2.3 Alignment mechanisms……39

3. Experiment……43
3.1 Growth of three types of VACNFs……..44
3.2 Characterization of VACNFs ……..46
3.3 E-beam lithography ……46
3.3.1 Overview……..46
3.3.2 Nanometer pattern generation system (NPGS)……47
3.3.3 Process……50
3.3.4 Problems presented in e-beam lithography……..51
3.4 Photolithography……..56
3.5 Charge transport measurements……...56

4. Structure and composition of dc VACNFs……59
4.1 Structure of dc VACNFs……...59
4.1.1 Interior structure of dc VACNFs……59
4.1.2 Tip of dc VACNFs……...66
4.1.3 Wavy dc VACNFs……...66
4.2 Composition of dc VACNFs……...71

5. Intrinsic charge transport properties of dc VACNFs……80
5.1 Define ohmic contacts between dc VACNFs and various metals……...80
5.1.1 Overview of various techniques to define ohmic contacts on carbon nanotubes.....80
5.1.2 Define ohmic contacts between dc VACNFs and metal electrodes……82
5.1.3 Various dc VACNF/metal contacts……88
5.2 Four probe charge transport measurements of dc VACNFs……91
5.2.1 I-V characteristics of dc VACNFs……...91
5.2.2 Charge transport model of dc VACNFs……..94
5.3 Outer layer-determined charge transport properties of dc VACNFs……...97
5.3.1 I-V characteristics of dc VACNFs before and after RIE……97
5.3.2 Structure difference of dc VACNFs before and after RIE……99
5.4 Temperature dependence of dc VACNF resistivity……...104
6. Inductively coupled PECVD VACNFs……...107
6.1 Structure of ICP VACNFs……107
6.2 Composition of ICP VACNFs……...115
6.3 Charge transport measurements of ICP VACNFs……120
6.4 Comparison of dc and ICP PECVD VACNFs……...123
6.4.1 Structure……123
6.4.2 Composition……...124
6.4.3 Charge transport properties……125

7. Conclusions and future work……...126
7.1 Conclusions……126
7.2 Future work……129

List of references……130

Vita……...135

List of figures

Figure page

Fig. 1.1 Crystal structure of hexagonal graphite…….....2

Fig. 1.2 (a) Schematic honeycomb structure of a graphene sheet. Single-walled carbon nanotubes can be formed by folding the sheet along lattice vectors. The two basis vectors $\mathbf{a}_1$ and $\mathbf{a}_2$ are shown. Folding of the (8,8), (8,0), and (10,-2) vectors lead to armchair (b), zigzag (c), and chiral (d) tubes, respectively.....5

Fig. 1.3 Atomic force microscope (AFM) image of a back-gated carbon nanotube FET (CNTFET). A single-walled CNT forms the FET channel connecting gold source and drain electrodes. The heavily doped wafer acts as the gate……6

Fig. 1.4 Schematic diagram of the liquid-metal method…….8

Fig. 1.5 A SEM image of a single multi-wall nanotube electrically contacted by four Au fingers from above. The separation between the inner two contacts is 2 μm…….9

Fig. 1.6 Ballistic transport through CNTs. (a) A SEM image of a MWCNT fiber above a liquid metal contact, before and after (inset) contact was made. (b) Conductance versus position of the nanotube fiber at room temperature. The steps correspond to different nanotubes coming into contact with the liquid metal as the fiber is lowered. At every step, the measured conductance appeared to be independent of the depth to which the tube was inserted into the metal……12

Fig. 1.7 Temperature dependence of the electrical resistivity for vapor grown carbon fibers. T_{HT} indicates the heat treatment temperatures of the fibers. The higher the curves, the larger the disorder. The curve with the lowest resistivity corresponds to crystalline graphite……17

Fig. 1.8 A schematic diagram of the PMMA suspended dispersion process. (a) PMMA suspended nanofibers spun-on top of a Si/SiO_2 substrate with a PMMA spacer layer. (b) Ends of nanofibers exposed by electron beam lithography and development. (c) Sputtered Nb electrodes encapsulating the ends of the nanofiber. (d) Current–voltage characteristics of the CNF. The nanofiber had a diameter of ~ 95 nm. The maximum current density was $1.8 \times 10^7 A/cm^2$. The bias voltage was swept from 0 to 20 V and back to 0 V. The measurement was performed in air at room temperature……..20

Fig. 1.9 SEM images of the initial VACNF array from dc hot-filament CVD (a) 45° view, and (b) top view, (c) cross section image of the array after TEOS CVD, (d) top view after mechanical polishing. The scale bars are 1 mm, 500 nm, 2 mm, and 500 nm, respectively. (e) and (f) I –V curves of individual CNFs in the embedded array

obtained with current-sensing AFM. The insets show four-probe station data corresponding to multiple parallel CNFs. (e) I –V curves of nanofibers from dc hot-filament CVD and (f) from inductively coupled PECVD……21

Fig. 1.10 Summary of the device fabrication process: (a) definition of the VACNF growth sites; (b) VACNF growth; (c) deposition of conformal SiO_2 layer; (d) planarization by chemical mechanical polishing; (e) reactive ion etching to uncover the nanofiber tip; (f) metallization via physical vapor deposition. (g) Typical I-V characteristics of the devices of (f) at four different temperatures (120°C, 90°C, 60°C and 20°C from left to right). These measurements show rectifying behavior with a high reverse-breakdown voltage. The forward bias current increased with temperature, consistent with the Schottky barrier junction model……23

Fig. 2.1 Schematic representation of the PECVD process for growing vertically aligned carbon nanofibers……28

Fig. 2.2 SEM image of (a) VACNF forest and (b) an isolated VACNF……..30

Fig. 2.3 (a) A SEM image of an array of carbon nanocones fabricated using dc PECVD. (b) and (c) Nanocone structures with the cone angle of 15° (b) and 5° (c). (d) Nanoscale cylinder-on-cone carbon tip synthesized by first growing a carbon nanocone with a higher C_2H_2/NH_3 ratio, followed by growing a carbon nanofiber with a relative low C_2H_2/ NH_3 ratio……31

Fig. 2.4 Schematic of an ICP reactor……34

Fig. 2.5 SEM images of carbon nanofibers showing forest of nanofibers grown in (a) hydrogen-rich plasma, (c) carbon-rich plasma, and (e) isolated nanofiber grown in hydrogen-rich plasma. TEM images taken near the catalyst base for the hydrogen-rich plasma (b) and the carbon-rich plasma (d)……36

Fig. 2.6 A TEM image of VACNFs showing a herringbone-like structure……..37

Fig. 2.7 Left SEM images were taken at (a) 0° and (b) 45° tilt angles, of an array of individual CNFs grown in the vicinity of the substrate/ sample holder edge. Right SEM images: (a) a forest of and (b) individual kinked CNFs (KCNFs)……...40

Fig. 2.8 Alignment mechanisms of carbon nanofibers. If a CNF grows vertically along the electric-field lines, electrostatic force *F* creates a uniform tensile stress across the entire catalyst particle/nanofiber interface, regardless of whether the particle is located at the tip (a) or at the base (b). If during the growth the CNF starts to bend due to spatial fluctuations in carbon precipitation at the particle/nanofiber interface, nonuniform stresses are created at the particle/nanofiber interface. For the nanoparticles at the tip (c) and at the base (d) the stresses are distributed in the opposite way, which leads to the nanofiber alignment in the first (c), but not in the

second (d) case. White ellipses indicate the interface regions where the stresses occur…….....41

Fig. 3.1 A schematic of experimental set up of NPGS……..48

Fig. 3.2 A flow chart of the e-beam lithography process performed in this work. (a) A SEM image of the as-grown dc PECVD VACNF forest. (b) A SEM image of VACNFs dropped onto a Si/SiO_2 substrate. (c) An AFM phase image of a VACNF after e-beam writing and development of PMMA. (d) A SEM image of a patterned VACNF device with 5 electrodes…….52

Fig. 3.3 A SEM image of the selected dc VACNF in Fig. 3.2 (b), with a higher magnification……..……..53

Fig. 3.4 Photomask design. (a) An overview of the 7x7 arrays. (b) The detailed layout of the unit in the square in (a)……57

Fig. 4.1 A SEM image of dc VACNF forest……..60

Fig. 4.2 TEM images of dc VACNF with a low (a) and a higher (b) magnification. (c) A high resolution TEM image of the detailed structure of a dc VACNF. (d) A high resolution TEM image. The open edges in the outer layer of VACNF can be readily observed……...61

Fig. 4.3 A HRTEM image of the central "cross-struts'. The "cross-struts" were often discontinuous……63

Fig. 4.4 A TEM image of a dc VACNF segment with a diameter of 120 nm. Region A: graphitic outer layer; region B: the layer with darker contrast; and region C: central "cross-struts"……64

Fig. 4.5 A schematic representation of dc VACNF structure. Region A is the outer layer, region B has darker contrast, and region C contains the so-called "cross-struts"….65

Fig. 4.6 (a) TEM image of a Ni particle at a dc VACNF tip. (b) HRTEM image of (a). Arrows indicate the regions that might be a compound of Ni and C……67

Fig. 4.7 TEM images of wavy dc VACNFs……...68

Fig. 4.8 Z-contrast STEM image of two wavy dc VACNFs. The white dots trapped in VACNFs are Ni……70

Fig. 4.9 EDX spectra for an individual dc VACNF from different points as indicated. Top image is a TEM image of the investigated VACNF. Top and bottom spectra were from point 1 and 3, respectively. Spectra from other points were similar to them……72

Fig. 4.10 Top image shows the dc VACNF studied for elemental distribution. Lower image presents the distribution of C (red), N (green), Si (blue) and Ni (purple) along the arrow direction in top image……...75

Fig. 4.11 EDX mapping of N, Ni and Si along a dc VACNF body……...76

Fig. 4.12 Auger linescan for C (blue) and Ni (red) across (a) a nanofiber sputtered for less than one minute and (b) a nanofiber sputtered for 4 mintues. Vertical black lines show the edges of nanofibers. A mask was placed over the sides of the image to highlight the nanofiber of interest……...79

Fig. 5.1 AFM images of a patterned electrode (a) before and (b) after 12 seconds of RIE……....83

Fig. 5.2 (a) A SEM image of a two-probe dc VACNF structure. (b) Typical I-V curves for two-probe VACNF structures experiencing no RIE (solid square) and excessive RIE (24 seconds) (solid triangle). (c) I-V curve of a two-probe dc VACNF structure subjected to RIE with optimized time (12 seconds). The resistance of the structure was 6.6 KΩ……..85

Fig. 5.3 An AFM image of a patterned dc VACNF ready for metal deposition. All the fiber segments are clearly visible……..86

Fig.5.4 (a) A SEM image of an individual dc VACNF with 6 electrodes, which underwent 11 seconds of RIE. (b) I-V curves measured between 3&4, 4&5, and 3&5 in (a).....87

Fig. 5.5 (a) A patterned dc VACNF with Cd/Au (200 nm each) electrodes. (b) I-V curve measured between electrodes 1 & 2 in (a). I-V curves measured between two electrodes in all possible combinations were all linear……...89

Fig. 5.6 A patterned dc VACNF with Mg/Au electrodes……..90

Fig. 5.7 SEM image of a completed dc VACNF structure with 5 metal electrodes (200 nm each of Ti/Au) contacting the nanofiber. Inset is a SEM image of the as-grown VACNF forest……92

Fig. 5.8 I-V curves for the 4-probe (electrodes 1, 2, 3 and 4 of the device in Fig. 5.7) and 2-probe (electrodes 2 and 3) measurements……..93

Fig. 5.9 Histogram of the 4-probe measured resistivity of 12 VACNFs. The resistivity ranged from 3.2×10^{-3} Ω·cm to 4.7×10^{-3} Ω·cm. The average resistivity was 4.2×10^{-3} Ω·cm……..95

Fig. 5.10 (a) A schematic representation of VACNF structure where α is the angle between the graphitic planes and the axis along fiber length. (b) The relationship between α and θ with θ = 90°-α.....96

Fig. 5.11 A patterned dc VACNF with four electrodes (200 nm Ti/Au).....98

Fig. 5.12 I-V curves for the four-probe measurements on the fiber in Figure 5.11 before and after O_2 plasma reactive ion etch.....100

Fig. 5.13 (a) TEM image of a dc VACNF segment with a diameter of ~120 nm. Region A: graphitic outer layer; region B: the layer with darker contrast; region C: central "cross-struts". (b) TEM image of a VACNF segment subjected to 5 seconds of O_2 plasma. This fiber segment had a diameter of ~120 nm. The arrows indicate the outer layer, which thickened along the fiber length. Inset shows a HRTEM image of the outer layer of this fiber. (c)-(d) TEM images of VACNF exposed to 10 seconds of RIE. Arrows indicate where the outer layer is completely (c) and partially (d) stripped off.....101

Fig. 5.14 (a)-(c): Schematic representations of dc VACNF structure with 0, 5 and 10 seconds of exposure to O_2 plasma etch respectively. Region A: graphitic outer layer; region B: the layer with darker contrast; region C: central "cross-struts".....103

Fig. 5.15 Temperature dependence of the four-probe resistance.....105

Fig. 5.16 Temperature dependence of the three-contact resistance.....106

Fig. 6.1 SEM images of ICP VACNFs grown at low pressure (a) and normal pressure (b).....108

Fig. 6.2 TEM images of ICP VACNFs grown at low pressure (a) and normal pressure (b). Inset in (a) shows the typical bamboo-like structure of low pressure ICP VACNFs.....109

Fig. 6.3 HRTEM images of low pressure ICP VACNFs. The open edges at the nanofiber surface are clearly visible.....110

Fig. 6.4 HRTEM images of normal pressure ICP VACNFs.....111

Fig. 6.5 A HRTEM image showing the interior structure of a normal pressure ICP VACNF.....113

Fig. 6.6 HRTEM images of a normal pressure ICP VACNF tip. (a) At the needle region, the graphitic planes follow the shape of the needle part of Ni. (b) Located between graphitic planes and Ni, region A may be some Ni carbide. (c) Graphitic planes end at the bottom of the cap.....114

Fig. 6.7 Compositional distribution of C (red), N (green), Si (blue) and Ni (purple) for a ICP VACNF (low pressure)……116

Fig. 6.8 Elemental mapping of N and Ni along ICP VACNFs (low pressure)……117

Fig. 6.9 Compositional distribution of C (red), N (green), Si (blue) and Ni (purple) for a ICP VACNF (normal pressure)……..118

Fig. 6.10 Elemental mapping of N and Ni along ICP VACNFs (normal pressure)……119

Fig. 6.11 (a)-(b) SEM images of a low pressure ICP VACNF before (a) and after (b) patterned with electrodes (200 nm Ti/Au). The unlabeled electrode had a bad contact with this nanofiber. (c) I-V characteristics measured between two electrodes. Resistance between electrodes 1&2, 2&3, 3&4 was 1.3 kΩ, 1.5 kΩ, and 2.7 kΩ respectively. The contact resistance of contact 2 can be calculated to be ~ 0.05 kΩ…….....121

Fig. 6.12 (a) SEM image of a patterned normal pressure ICP VACNF (Cd/Au, 200 nm each). (b) I-V curves measured from (a). The resistance between electrodes 1&2, 2&3, 4&5, 1&5 was 2.8 kΩ, 3.4 kΩ, 3.2 kΩ and 6.6 kΩ respectively……122

Chapter 1 Charge transport properties of carbon nanotubes and related carbon materials

Carbon nanostructures, such as carbon nanotubes and nanofibers, have properties that make them attractive for many electronic applications, and understanding the charge transport properties of these nanostructures is key for the realization of these applications. The charge transport properties are directly related to structures. Carbon nanotubes and nanofibers possess radically different structures, and it is expected that their charge transport properties vary as well. However, carbon nanotubes and nanofibers are composed of grapheme sheets or planes, and inevitably have very close connections to graphite. Bearing in mind the structural relationship and differences of carbon nanotubes and nanofibers, the structures and charge transport properties of graphite, carbon nanotubes and carbon nanofibers are addressed below.

1.1 Charge transport properties of graphite

Graphite is a free element form of carbon. Ideally, graphite is composed of planar hexagonal nets of carbon atoms, as shown in Fig. 1.1. Within each layer, a carbon atom is bonded with three others through sp^2 bonding, which stems from the sp^2 hybridization of three of the four valence electrons, and σ bonds are formed. Such sp^2 bonding has very high strength. The fourth electron lies in a p_z orbital normal to the σ bonding plane. These p_z orbitals form weak π bonds with adjacent p_z orbitals.

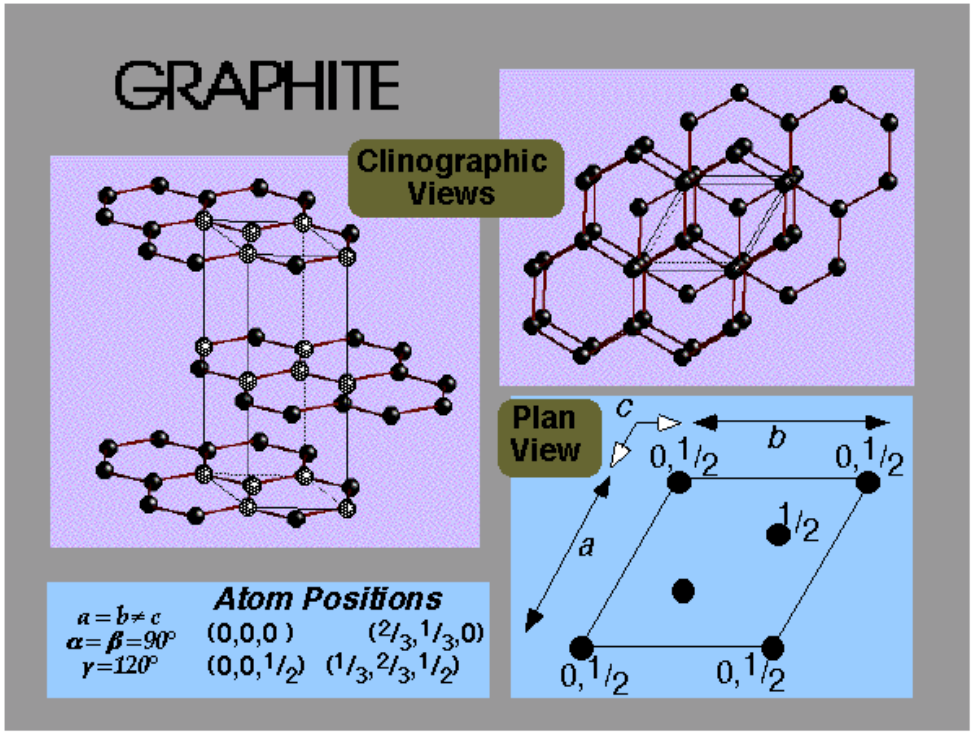

Fig. 1.1 Crystal structure of hexagonal graphite[1].

According to the sequences of the stacking of the planar layers, graphite can be classified into hexagonal and rhombohedral graphite. While hexagonal graphite has an –ABABAB- stacking order, rhombohedral graphite has an –ABCABCABC- stacking sequences. The crystal lattice parameters of hexagonal and rhombohedral graphite are: a_0 = 0.245 nm, c_0 = 0.6708 nm; and a_0 = 0.2256 nm, c_0 = 1.006 nm. Hexagonal graphite is the thermodynamically stable form of graphite, its structure is illustrated in Fig. 1.1. Natural graphite often contains both hexagonal and small amount of rhombohedral.

The peculiar crystal structure of graphite results in a considerable anisotropy that is reflected in the electrical properties of graphite. In the basal plane, graphite is a relatively good conductor with a resistivity (ρ_a) in the range of ~2.5×10^{-5} to ~5.0×10^{-4} Ω·cm; whereas in the c direction, the resistivity (ρ_c) may be 10,000 times higher than in the basal plane. Along a direction with an angle θ to the c axis,[2] the resistivity is given by

$$\rho(\theta) = \rho_a \sin^2\theta + \rho_a \cos^2\theta. \quad (1.1)$$

Similar to metals, the electrical resistivity of the graphite crystal in the basal plane increases with temperature, due to the decrease in the electron mean free path. The electrical resistivity in the c direction, however, decreases slightly with increasing temperature, possibly because electrons can jump or tunnel from one plane to another due to increased thermal activation.

1.2 Charge transport properties of carbon nanotubes

Single-wall carbon nanotubes (SWCNTs) are composed of a single graphene sheet wrapped into a cylinder along an (m,n) lattice vector (Fig. 1.2), whereas multi-wall carbon nanotubes consist of many concentric graphene sheets wrapped around a common center. Fig. 1.2 presents three types of SWCNTs with different chirality.

Many exceptional physical properties of CNTs, especially the electrical transport properties, stem from their unique structures. Defect-free CNTs can either be metallic or semiconducting, depending on both the diameter and chirality. For a single wall (n,m) tube (n,m are known as helicity indices), if n-m is a multiple of 3, the tube is metallic[4]; otherwise, it is semiconducting. Therefore, two-thirds of the tubes are semiconducting, and one-third are metallic. It is predicted that the bandgap of semiconducting tubes depends on the diameter, with a value of about 0.9 eV/D, where D is the nanotube outer diameter in nm.[5]

1.2.1 Electrical transport measurement techniques for carbon nanotubes

To date, electrical transport measurements of carbon nanotubes have been performed in three ways. Early knowledge of transport properties in CNT was obtained through a field-effect transistor (FET) scheme.[6,7] The basic carbon nanotube-FET structure consists of two metal electrodes designated as source and drain connected by a carbon nanotube. A third electrode, the gate, was separated from the CNT by a thin insulator film as shown in Fig. 1.3. Source and drain electrodes allow the conducting properties of the nanotube to be measured, and the gate electrode is used to control the nanotube carrier density. Typically, the heavily doped Si substrate is used as the gate. Alternatively, a scanning-

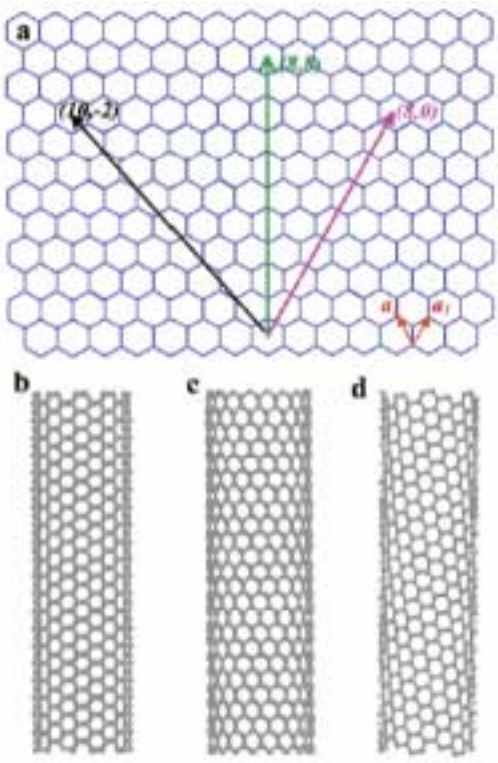

Fig. 1.2 (a) Schematic honeycomb structure of a graphene sheet. Single-walled carbon nanotubes can be formed by folding the sheet along lattice vectors. The two basis vectors $\mathbf{a}_1$ and $\mathbf{a}_2$ are shown. Folding of the (8,8), (8,0), and (10,-2) vectors lead to armchair (b), zigzag (c), and chiral (d) tubes, respectively.[3]

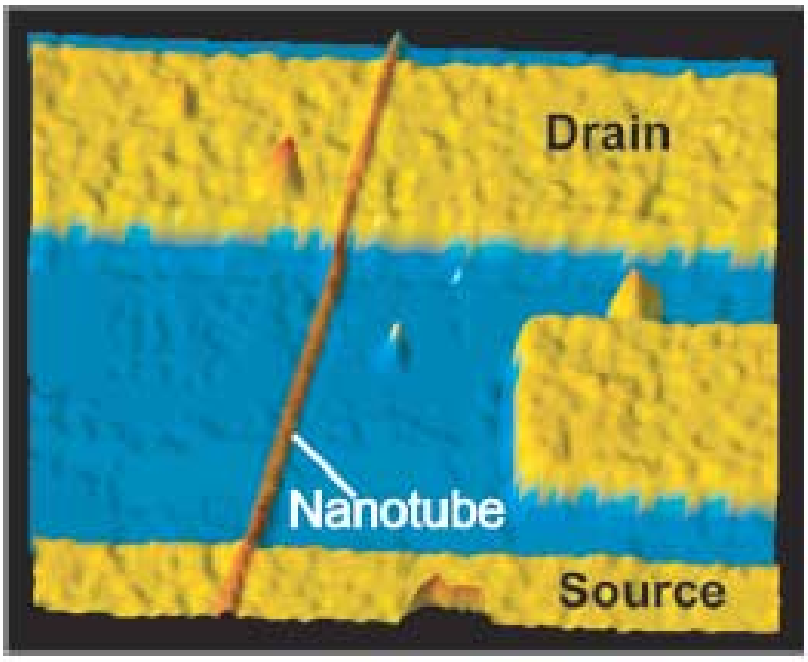

Fig. 1.3 Atomic force microscope (AFM) image of a back-gated carbon nanotube FET (CNTFET). A single-walled CNT forms the FET channel connecting gold source and drain electrodes. The heavily doped wafer acts as the gate. [8]

tunneling microscope tip can serve as the gate electrode, if positioned above a CNT.[9] This so-called scanned gate microscopy (SGM) allows local modification of conducting properties of the tube by measuring the conductance of the sample as a function of tip position. It also reveals individual scattering sites in the CNTs.

A second way for electrical transport measurements is the liquid-metal method (Fig. 1.4). First, the end of a macrobundle of CNTs is fixed on a moveable manipulator. While lowering and immersing the CNTs into a liquid metal, a single CNT makes contact with the liquid metal first, enabling conductance measurements on a single nanotube.[10] The advantage of this technique is that the length of the nanotube inserted into the liquid metal can be freely adjusted, without involving microfabrication technology.

However, in both methods described above, the measured transport properties include contributions from the nanostructure and the electrode-nanostructure junctions. The most reliable way to measure the intrinsic transport properties of CNTs is the four-probe technique, where four metal electrodes are attached to a single CNT, which is supported on an insulator layer on a Si substrate (refer to Fig. 1.5). Current runs from the two electrodes on both ends, the I-V characteristic can be readily measured from the middle two electrodes, and the resistance of the tube can be obtained without involving the contact resistances. Since two-terminal contact resistance can vary significantly, ranging from as small as 6 kΩ to several MΩ, and contact behavior can obscure or even conceal the intrinsic electrical properties of CNTs, the four-probe measurements are highly preferred. Unfortunately, most four-probe measurements have been performed on SWCNT ropes (nanotube bundles), not on an individual SWCNT.

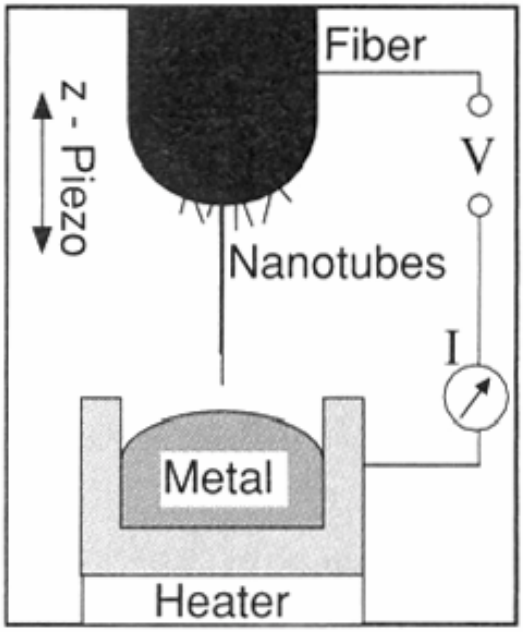

Fig. 1.4 Schematic diagram of the liquid-metal method.[10]

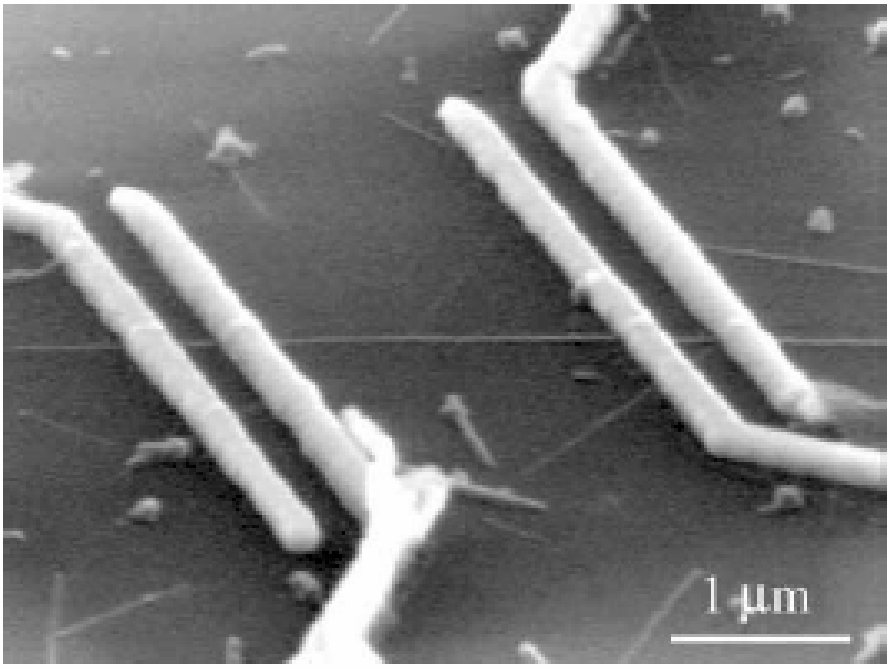

Fig. 1.5 A SEM image of a single multi-wall nanotube electrically contacted by four Au fingers from above. The separation between the inner two contacts is 2 μm. [11]

1.2.2 Metallic carbon nanotubes

In the carbon nanotube field effect transistor (CNTFET) scheme, when the conductance of the tube is measured as the gate voltage varies, two different transport behaviors can be discerned. In the case that the conductance of the tube is independent of the gate voltage, the nanotube is metallic; otherwise, it is semiconducting.

The small diameter and long length of SWCNTs makes them almost ideal 1-D systems. This in turn implies drastically reduced carrier scattering and the possibility of ballistic transport. In 1-D systems like SWCNTs, electrons can move in only two directions along the tube axis: forward and backward. The other two confinements of electrons are energy and momentum conservation. These three constraints lead to reduced scattering processes that are responsible for the electrical resistance of the metallic CNTs.[12, 13] Such reduced scatterings enable CNTs to carry remarkably high current density ~ 10^9A/cm^2,[10] which is orders of magnitude larger than current densities found in other electrical interconnects, and outperform the best metals. Electronic current in SWCNTs was found to saturate at ~ 20 μA,[14] while current of up to 1 mA was reported for low-defect arc-produced MWCNT.[15]

In the absence of scattering, the transport is ballistic. Ballistic behaviors at room temperature were observed in arc-produced metallic MWCNTs and catalytically produced SWCNTs.[9,10,15] Such behavior means that there is no electronic backscattering over length, the scale of which is on the order of many hundreds of nanometers or even micrometers at room temperature, as was first confirmed by experiments performed by de Heer's group at Georgia Tech.[10] They dipped a multi-wall carbon nanotube into liquid metal (mercury or gallium) and simultaneously measured the conductance of the tube. It

was found that the measured conductance appeared to be independent of the depth to which the tube was inserted into the metal (Fig. 1.6), suggesting that electronic transport occurs ballistically in nanotubes, even at room temperature. Other groups also observed ballistic transport in nanotubes with different experimental set-ups. Dai's group at Stanford University observed ballistic transport in metallic SWCNTs with Pd ohmic contacts[16], and confirmed that the mean free path for defect scattering in SWCNTs grown by chemical vapor deposition can be up to 4 μm.

Still, most CNTs, especially catalytically produced MWCNTs, are diffusive conductors. In these nanotubes, the disorder results in increased resistance. The defects also affect transport in arc-produced MWCNTs.

1.2.3 Semiconducting carbon nanotubes

Carbon nanotubes can be *n*-doped or *p*-doped. The first semiconducting SWCNT was reported by Tans *et al.* in 1998.[6] A SWCNT was positioned to bridge two metal electrodes, which acted as source and drain terminals. The tube conducted at negative Vg and turned off with a positive Vg in a manner analogous to a *p*-type FET, indicating that the dominant carriers were holes. The ON/OFF current ratio for this device was ~ 10^5.

As-grown semiconducting SWCNTs are typically *p*-type. A number of explanations have been proposed to explain this behavior, such as doping by oxygen in air, or charge transfer from high work-function metal electrodes.[17,18] Controlled chemical doping of tubes, both p- and n-type, has been achieved in a number of ways. One way to generate *n*-type CNTs is to dope *p*-type CNTs using electron donors, such as alkali metals.[18,19,20]

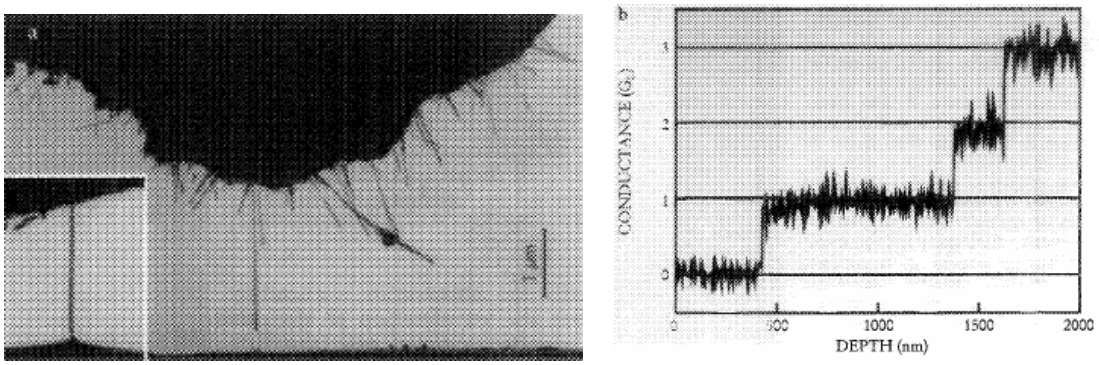

Fig. 1.6 Ballistic transport through CNTs. (a) An SEM image of a MWCNT fiber above a liquid metal contact, before and after (inset) contact was made. (b) Conductance versus position of the nanotube fiber at room temperature. The steps correspond to different nanotubes coming into contact with the liquid metal as the fiber is lowered. At every step, the measured conductance appeared to be independent of the depth to which the tube was inserted into the metal.[10]

Another way to perform the *p*- to *n*- transformation is by heating a *p*-type CNTFET under vacuum, a process designed to outgas the adsorbed oxygen. This process is reversible. By exposing an *n*-type CNTFET, which was annealed in vacuum, to oxygen, a *p*-type character was re-established.[18] Therefore, it is strongly suggested by the authors that oxygen is responsible for the *p*-type behavior of CNTs in air.

The *p*- to *n*- type transformation can be accomplished by both doping with alkali metals and exposure to oxygen, as mentioned above. However, it is likely that these two methods have achieved this through distinct mechanisms. Whereas the first method involves conventional doping on the bulk of CNTs with an electron donor, IBM workers proposed that the transformation was due to the effect of oxygen on the contact barriers, although oxygen may indeed lead to some doping of the bulk of the CNT.[21] They pointed out that for the Schottky junctions at the metal-CNT contacts, the outgasing of oxygen from the device changed the band-bending near the contacts, and the position of the Fermi level within the band-gap changed as a function of the amount of oxygen present at the contacts.

The properties of semiconducting CNTs addressed above are remarkable. The most impressive are the high mobilities obtained given the small channel width and the simplicity of the fabrication methods employed. The mobility of CNTs is typically in the range of 1000-10000 cm^2/V s for CVD-grown tubes. This value is significantly higher than those in Si MOSFETs, indicating that CNTs are a remarkably high-quality semiconducting material.

1.2.4 Temperature dependence of charge transport properties of CNTs

At low temperatures, SWCNTs exhibit a number of interesting quantum phenomena, such as single-electron tunneling, quantum interference, Luttinger liquid behavior, and Kondo effect. In addition to the quantum phenomena, superconductivity in SWCNTs has also been observed, but only at very low temperatures, with transition temperatures of ~ 0.55 K for 1.4-nm SWCNTs[23] and ~ 5 K for 0.5 nm SWCNTs grown in zeolites[24].

Although it is very difficult to separate an individual SWCNT, and in turn carry out transport property studies, it is relatively easier to work on MWCNTs due to their larger diameters. Four probe measurements on metallic MWCNTs have indicated that their resistivities have wide variations. Ebbesen *et al*. at NEC have done comprehensive studies on this subject.[25] They successfully deposited four tungsten wires on top of individual MWCNTs, which had been annealed at 2850^{o}C. Resistance measurements were reported for 8 different tubes and results differed widely. The room temperature resistivity values for the MWCNTs ranged from 0.8 Ω·cm to 5.1 μΩ·cm. The most common type of temperature dependence behavior of measured MWCNTs was, according to the authors, a consistent slight increase in resistivity with decreasing temperature. The authors did not consider that these tubes should be thought of as semiconducting, particularly in view of their low resistivities. Instead, they suggest that the tubes are essentially metallic. A similar trend was observed by Buitelaar *et al*.[13] However, they proposed that the MWCNTs were doped, either intrinsically or due to charge transfer from the metallic contact.

In summary, carbon nanotubes are found to have electrical properties that rival or exceed the best metals or semiconductors known. This clearly makes them very

promising candidates for electronic applications. For example, metallic tubes can serve as interconnects, and semiconducting tubes can be integrated into FET devices to minimize the size and optimize the performance of the device. However, this task remains challenging due to several issues. First, the chirality of CNTs cannot be controlled during any growth process known. Second, there are no reliable, rapid, and reproducible approaches to creating complex arrays of nanotube devices. This manufacturing issue is by far the most significant impediment to using nanotubes in electronics applications. It is expected, however, with the collaboration of engineers, materials scientists, physicists and chemists, that the technology of nanotubes may see significant progress in the near future.

1.3 Charge transport properties of carbon fibers

Carbon fibers represent an important class of graphite-related materials that are closely connected to carbon nanotubes, with regard to structure and properties. Carbon fibers can fall into three major categories: commercial mesophase pitch-based carbon fibers, vapor grown carbon fibers (fibers grown through chemical vapor deposition), and carbon nanofibers grown by plasma enhanced chemical vapor deposition.

1.3.1 Different types of carbon fibers

Commercial mesophase pitch-based carbon fibers, such as PAN (polyacrylonitrile) fibers, are grown based on polymer precursors. These fibers will not be discussed in detail, since their major applications are based on their marvelous mechanical properties. The preparation of another type of carbon fiber, the vapor grown fiber, is based on a

catalytic process, chemical vapor deposition. This approach is usually carried out through the decomposition of carbon-containing material on dispersed catalyst particles. The vapor grown carbon fiber typically consists of a MWCNT-like core and an epitaxially grown outer sheath. The diameters of such fiber are usually in the range of 10 nm to 100 μm. Heat treated at various temperatures, the morphologies of the vapor grown fibers can change from the "tree-ring" style to the facet-bearing morphology in the outer region. When the diameter of the vapor grown fibers is in the range of 10-100 nm, they are called nanofibers.

The third type of fibers, grown by plasma enhanced chemical vapor deposition (PECVD), have recently drawn much attention[26,27,28,29,30,31,32]. Compared with CVD, PECVD systems provide a highly reactive environment with low operating temperatures and high deposition rates. Most importantly, plasma enables an aligned growth of CNFs. The major advantage of PECVD fibers is that the orientation, locations, diameters, and compositions of these fibers can be well controlled, as demonstrated by the work of our group. [26,27,28,29,30] These fibers usually have diameters ~ 10 nm to 200 nm, and mostly possess a bamboo-like structure.

1.3.2 Charge transport measurements of carbon fibers

Resistivity measurements have been done on a variety of vapor grown carbon fibers, and the results are summarized in Fig. 1.7. For well-graphitized fibers, the results indicated an approximately linear temperature dependence for resistivity up to the melting point, and the resistivity increased with the increasing temperature. By contrast,

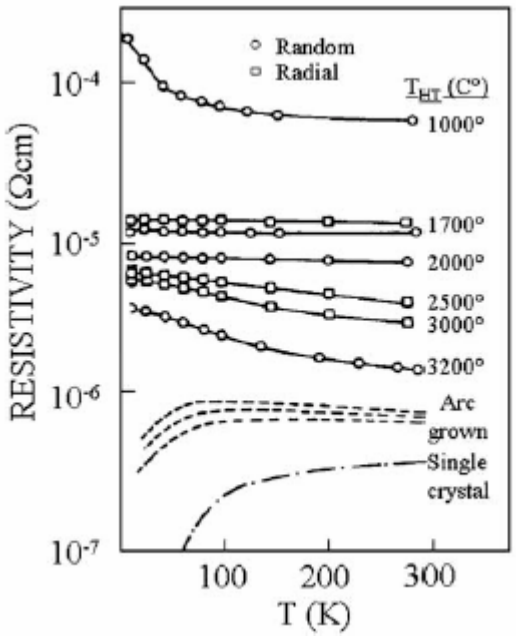

Fig. 1.7 Temperature dependence of the electrical resistivity for vapor grown carbon fibers. T_{HT} indicates the heat treatment temperatures of the fibers. The higher the curves, the larger the disorder. The curve with the lowest resistivity corresponds to crystalline graphite.[33]

the pre-graphitic vapor grown carbon fibers exhibited the opposite behavior, with the resistivity decreasing as the temperature increased.

Although charge transport properties of vapor grown carbon fibers have been extensively studied, the reports on those of PECVD carbon nanofibers are essentially lacking, with the exception of a few two-probe measurement results, in addition to our published four-probe charge transport measurements result.[34] Different approaches have been used to carry out two-probe charge transport measurements. One approach is to remove the CNFs from the growth substrate, drop them onto a chip with predefined alignment marks, and place electrodes on these fibers to perform electrical measurements. Another method is to fill the as-grown CNF arrays with SiO_2, followed by mechanical polishing to produce CNF arrays with only the tips exposed. A conductive AFM or a metal probe is then used to measure the I-V characteristics between the CNF tips and the substrate.

The Ahmed group at the University of Cambridge has employed the first approach to investigate the electrical characteristics of PECVD carbon nanofibers by suspending CNFs in a PMMA solution and using e-beam lithography to pattern two metal electrodes on an individual CNF.[35] The catalyst was a 3 nm thick Ni film, and a mixture of C_2H_2 and NH_3 was used as the feedstock and etching agent respectively. The PECVD-grown vertically aligned CNFs were removed from the substrate and dispersed in a solution of PMMA. Before spin-on of the CNF-PMMA solution onto the Si/SiO_2 chip with alignment marks, a thin layer PMMA without CNFs was spin coated onto the target substrate. Then, the positions of the randomly dispersed CNFs were mapped in reference to the markers, and e-beam lithography was used to define the positions of the electrical

contacts. Nb was then sputtered onto the substrate to make electrical contacts. The process is illustrated in Fig. 1.8 (a)-(c). They found that the CNFs were metallic and able to maintain a current density ~ $2x10^6 A/cm^2$ for more than 15 days with a maximum current density of ~$1.8x10^7 A/cm^2$ (Fig. 1.8 (d)) in air at room temperature. As to the hysterisis of the I-V curve, the authors considered it may have been due to successive electrical breakdown of the CNF outer shells during the voltage sweeping.

The advantages of this technique are: (1) the unwanted CNFs can be removed from the substrate after lift-off so that only those held by contacts remain on the substrate; and (2) the deposited metal may completely encapsulate the CNF ends, providing a strong contact. On the other hand, the drawbacks are also obvious. The CNFs are embedded in the PMMA, and it is not easy to tell the fiber is an individual one or in a bundle, not to mention the difficulty in discerning defects in the fiber, which may cause problems for subsequent electrical measurements. Another drawback is more troubling: the contact behaviors can never be excluded to reveal the true intrinsic properties of CNFs.

Another approach adopted by the Li *et al.* at NASA Ames Research Center is to directly measure the electronic properties of vertical carbon nanofiber arrays grown by inductively coupled PECVD and dc hot-filament PECVD. First, the as-grown CNF arrays were filled with conformal SiO_2 using chemical vapor deposition. Subsequent mechanical polishing yielded a flat surface with only the very ends of the CNF array exposed, as shown in Fig. 1.9. The electronic properties of individual CNFs were then measured using current-sensing atomic force microscopy. The resistance of the CNFs was about 300 kΩ. The I-V curves of a bundle of dc hot filament PECVD CNFs are linear, but those of inductively coupled PECVD fibers were non-linear.[36]

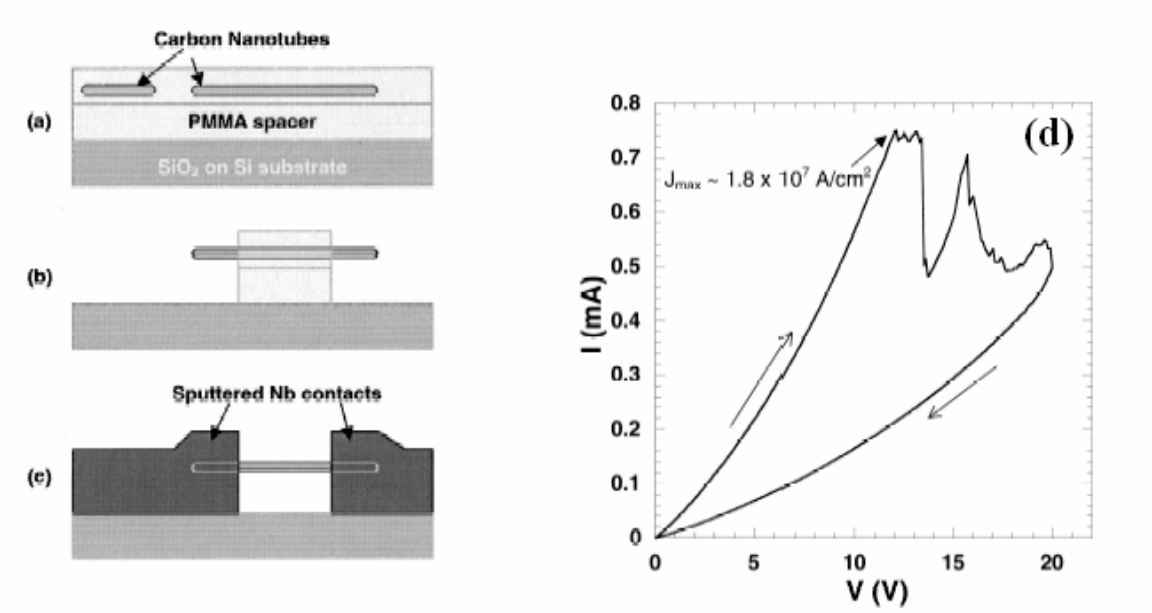

Fig. 1.8 A schematic diagram of the PMMA suspended dispersion process. (a) PMMA suspended nanofibers spun-on top of a Si/SiO_2 substrate with a PMMA spacer layer. (b) Ends of nanofibers exposed by electron beam lithography and development. (c) Sputtered Nb electrodes encapsulating the ends of the nanofiber. (d) Current–voltage characteristics of the CNF. The nanofiber had a diameter of ~ 95 nm. The maximum current density was $1.8x10^7 A/cm^2$. The bias voltage was swept from 0 to 20 V and back to 0 V. The measurement was performed in air at room temperature.[35]

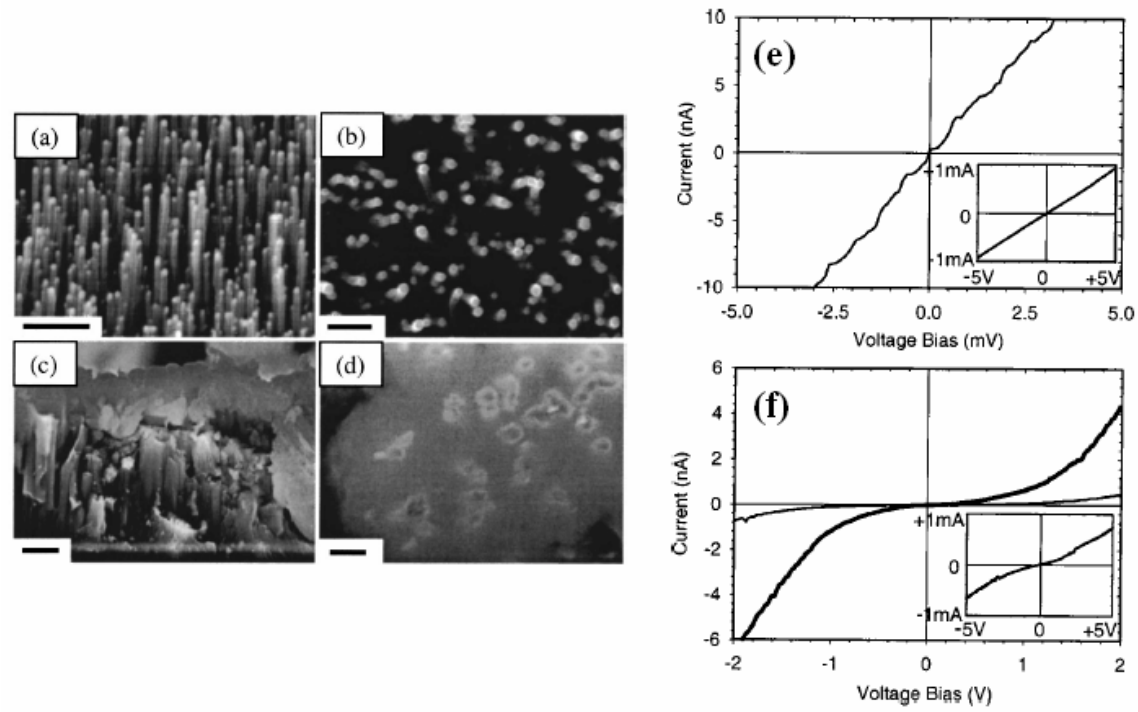

Fig. 1.9 SEM images of the initial VACNF array from dc hot-filament CVD (a) 45° view, and (b) top view, (c) cross section image of the array after TEOS CVD, (d) top view after mechanical polishing. The scale bars are 1 mm, 500 nm, 2 mm, and 500 nm, respectively. (e) and (f) I –V curves of individual CNFs in the embedded array obtained with current-sensing AFM. The insets show four-probe station data corresponding to multiple parallel CNFs. (e) I –V curves of nanofibers from dc hot-filament CVD and (f) from inductively coupled PECVD.

The reason for these different curves could be due to the junction effect between the substrate and CNFs. The ICP samples had a thin Al layer (10 nm) on the growth substrate before starting fiber growth, while the hot filament sample had a thick (200 nm) Ti or Mo layer. The junctions formed between different metals and CNFs may affect the I-V characteristics of the whole structure. In fact, this idea has been confirmed for dc PECVD grown VACNFs by Yang *et al.* in our group.[37]

Yang *et al.* demonstrated that a region of semiconducting SiC was formed directly beneath the VACNF during the growth, creating a Schottky-barrier junction between this semiconductor material and the metallic carbon nanofibers, which was responsible for the rectifying behavior presented by the electronic devices using single VACNFs. Summary of the device fabrication process is shown in Fig. 1.10 from (a) to (f). The dc current vs voltage (I-V) characteristics of the devices was investigated using the Si substrate as a bottom electrode. The typical I-V characteristics of the devices are shown in Fig. 1.10 (g).

The device fabrication process adopted by Yang *et al.* is similar to that by Li *et al*., except patterned catalyst was used by Yang *et al.* to produce spatially segregated nanofibers instead of the densely packed and randomly arranged VACNF forests used by Li *et al.*. As it is expected that devices will rely more on the deterministic arrangement used by Yang *et al.*, these measurements may be of more practical value.

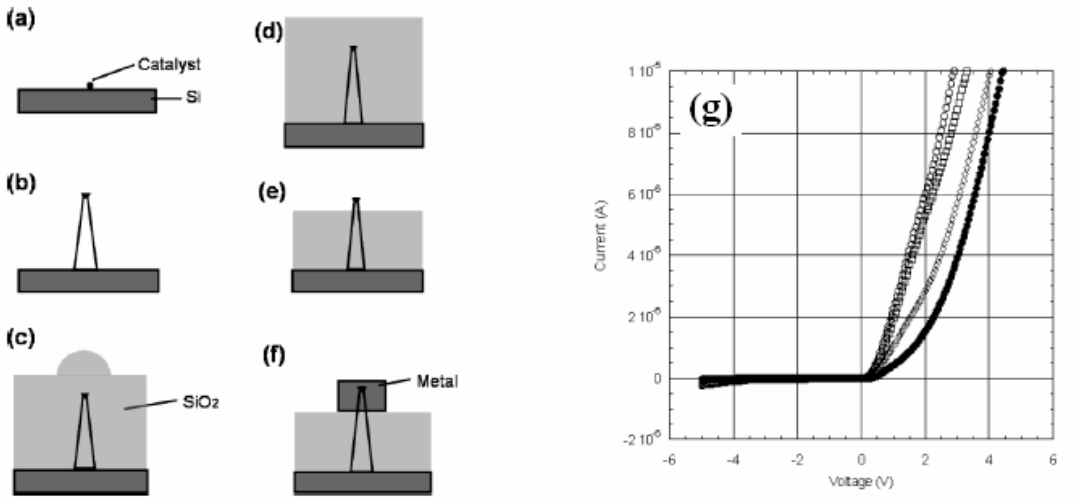

Fig. 1.10 Summary of the device fabrication process: (a) definition of the VACNF growth sites; (b) VACNF growth; (c) deposition of conformal SiO_2 layer; (d) planarization by chemical mechanical polishing; (e) reactive ion etching to uncover the nanofiber tip; (f) metallization via physical vapor deposition. (g) Typical I-V characteristics of the devices of (f) at four different temperatures (120^{o}C, 90^{o}C, 60^{o}C and 20^{o}C from left to right). These measurements show rectifying behavior with a high reverse-breakdown voltage. The forward bias current increased with temperature, consistent with the Schottky barrier junction model.[37]

1.4 Scope of dissertation

As mentioned above, while some two probe measurement results have been reported for PECVD CNFs, it is still a far cry from a good understanding of the intrinsic charge transport properties of these fibers. In this dissertation, the intrinsic charge transport properties of various PECVD carbon nanofibers have been studied through four-probe measurements. Three types of fibers, namely dc PECVD VACNFs and inductively coupled PECVD VACNFs grown with both normal and low pressure, respectively, are used in this work. They are all in the form of forests on Si chips. Ni serves as the catalyst for all these fibers. Particular attention is given to dc PECVD fibers.

Since the charge transport properties are closely related to the growth conditions, structure, and composition of the fibers, Chapter 2 is devoted to describing the growth mechanism of vertically aligned carbon nanofibers. Various growth techniques of VACNFs, including dc PECVD, inductively coupled PECVD and microwave PECVD, are briefly reviewed. The growth model of bamboo-like structures is described, and several critical alignment mechanisms are discussed.

Chapter 3 describes experimental details of this work. It begins with introducing growth conditions of the three types of fibers used in this work, followed by a brief description of techniques employed to characterize these fibers. E-beam lithography was used to pattern electrodes on fibers and is a critical step of this work which is discussed in detail. Photolithography, which is used to define big contact pads, is briefly discussed.

Structure and composition of dc VACNFs are discussed in detail in Chapter 4. TEM, EDX and elemental mapping results of these fibers are presented. Detailed structure of the outer layer of dc VACNFs is given particular attention. Elemental distributions of Ni,

Si, N, and C along dc VACNFs are discussed, and Ni distribution in various layers of fiber structure is presented. This chapter concludes with a proposed growth model that describes Ni incorporation in the fiber body.

Chapter 5 details experimental results from intrinsic charge transport measurements of dc VACNFs. In the first part of this chapter, a simple and reliable technique to form ohmic contacts on carbon nanofibers is presented. In the second and third part, four probe charge transport measurements of dc VACNFs are discussed, and I-V characteristics of dc VACNFs are presented along with a simple model for charge transport of dc VACNFs. Since the outer layer of dc VACNFs plays a critical role in charge transport behavior, the method to etch away the outer layer and the subsequent I-V characteristics are detailed in the second part of this chapter. Temperature dependence of charge transport properties of these fibers are discussed in the fourth part.

Chapter 6 presents experimental results from inductively coupled PECVD (ICP) VACNFs. Structure and composition of two types of inductively coupled PECVD VACNFs, namely VACNFs grown at normal pressure and low pressure, are described. Charge transport properties of these fibers are also discussed. Comparisons of dc and ICP VACNFs in structure, composition and charge transport properties are described in detail.

Conclusions drawn from this work and suggested future work are provided in Chapter 7.

Chapter 2 Growth of vertically aligned carbon nanofibers by plasma-enhanced chemical vapor deposition

Growth of vertically aligned CNFs is of prime importance to enable both fundamental studies and potential applications of these fibers. Aligned CNFs are fabricated mainly by plasma-enhanced chemical vapor deposition (PECVD). PECVD systems provide a highly reactive environment with low operating temperatures and high deposition rates. The plasma systems are very stable and reproducible because of the controllability of the process parameters: gas flow, discharge frequency, pumping speed, input power, and pressure. Most importantly, plasma enables the vertically aligned growth of CNFs. Merkulov *et al*. have proposed the mechanism of nanofiber alignment in PECVD processes.[29]

2.1 Various growth techniques of VACNFs

A variety of plasma sources have been reported for successful growth of VACNFs. The sources include direct-current (dc PECVD), hot filament dc PECVD, microwave (MPECVD), inductively coupled plasma (IC PECVD), radio-frequency (RF PECVD), electron cyclotron resonance (ECR PECVD), magnetron-type radio frequency, and hollow cathode plasma. MPECVD, dc PECVD and ICP PECVD are discussed in detail in the following text, as they are mostly used to fabricate VACNFs.

2.1.1 dc PECVD

Among all the PECVD techniques, dc PECVD has been most widely used to produce VACNFs on both chip and wafer scales. Catalysts adopted for this method are typically Ni, Fe and Co, because these transition metals possess a high activity and form a moderately low temperature eutectic with carbon. The growth substrate usually serves as the cathode; therefore a conductive substrate must be used to keep the plasma on. Growth of VACNFs on insulating materials, such as SiO_2, can be achieved by putting a thin metal film under the catalyst film to make contact between the substrate (cathode) and the metal film. Acetylene gas is generally used as the carbon source and ammonia gas is used as the etching agent. The operating parameters (the power input, C_2H_2/NH_3 gas ratio, flow rate, growth time, etc.) distinctly influence the diameter, morphology and uniformity of the VACNFs.

Our group at the Oak Ridge National Laboratory has carried out extensive studies on vertically aligned CNF (VACNFs) growth by dc PECVD. A schematic representation of the PECVD process for growing VACNFs is shown in Figure 2.1. The substrate is pre-patterned with catalyst film or particles. The sample is then mounted directly on a heater plate, which serves as a cathode. After the chamber has reached the base pressure, ammonia is introduced into the chamber and the sample is pretreated with the ammonia plasma and temperature. As the result of this treatment, catalyst nanoparticles are formed from the deposited catalyst dots. These nanoparticles act as the necessary seeds for catalytic growth of isolated VACNFs. After the pre-etching step, with the ammonia plasma still on, acetylene is introduced into the chamber and the VACNF growth begins.

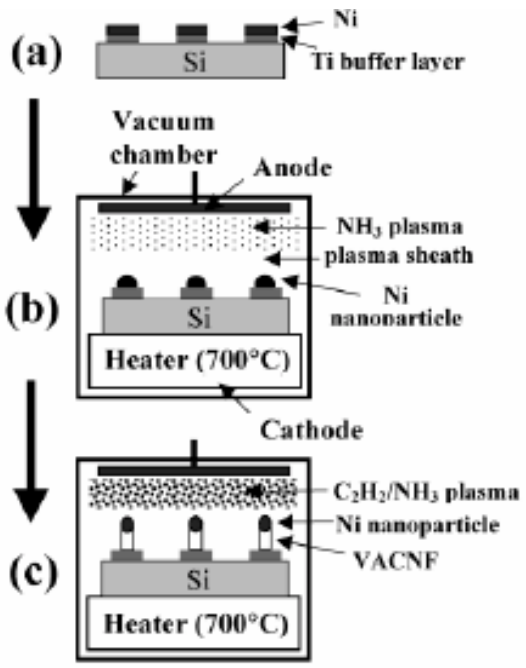

Fig. 2.1 Schematic representation of the PECVD process for growing vertically aligned carbon nanofibers.[28]

One advantage of dc PECVD is that the VACNFs can be grown either in the form of forests (Fig. 2.2 (a)) or discrete and isolated individual VACNFs (Fig. 2.2 (b)) on pre-determined locations, with the spacing varying from tens of nanometers to several microns. Merkulov *et al*. have demonstrated that by sputtering a blanket coating of catalyst film onto the growth substrate, VACNF forests can be grown; if the catalyst films are in the form of pre-patterned dots, a single nanofiber is formed as the size of the dot approaches a critical value.[26]

Another benefit of dc PECVD technique is that the shape of VACNFs can be controlled during the synthesis process. Structures can be nearly cylindrical, conical or combinations of the two shapes can be dynamically created.[27,29] By adjusting the C_2H_2/NH_3 gas ratio it is possible to precipitate carbon along the outer walls of VACNF, creating conical VACNFs, or vertically aligned carbon nanocones (VACNCs) (Fig. 2.3 (a), (b), and (c)). Dynamic control of C_2H_2/NH_3 gas ratio can even lead to the formation of VACNFs with multiple geometrically distinguishable regions. For instance, a so-called cylinder-on-cone geometry can be achieved, which has a conical base and a sharp cylindrical tip (Fig. 2.3 (d)). The conical base offers mechanically strong bonding between the whole structure and the substrate, and the sharp cylindrical tip can be used for field emission.

However, the dc PECVD technique possesses a number of drawbacks when employed for VACNF growth. The major disadvantage is that the requirement for a conductive substrate largely limits the choice of substrate materials. Plasma instability is another problem commonly observed in the growth process. Non-uniformity in the substrate

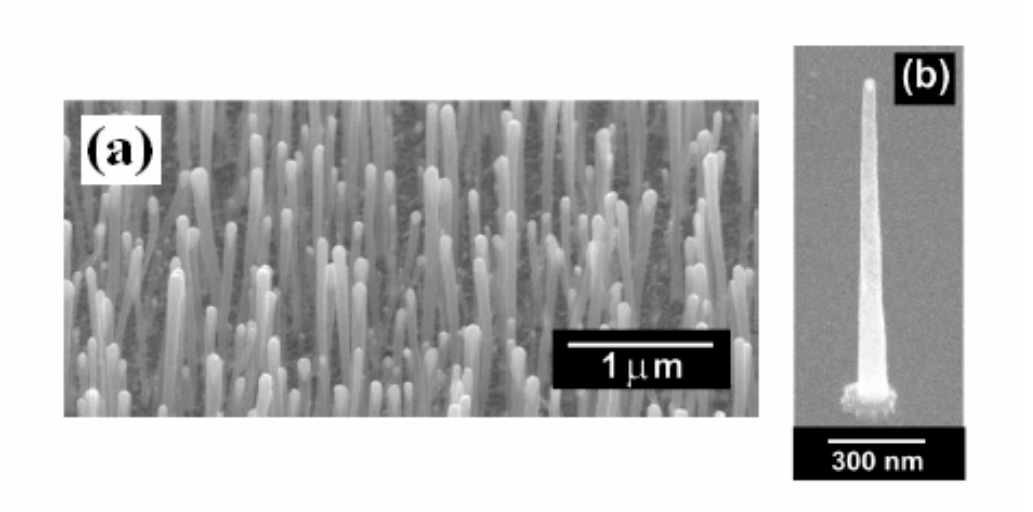

Fig. 2.2 SEM image of (a) VACNF forest and (b) an isolated VACNF. [27]

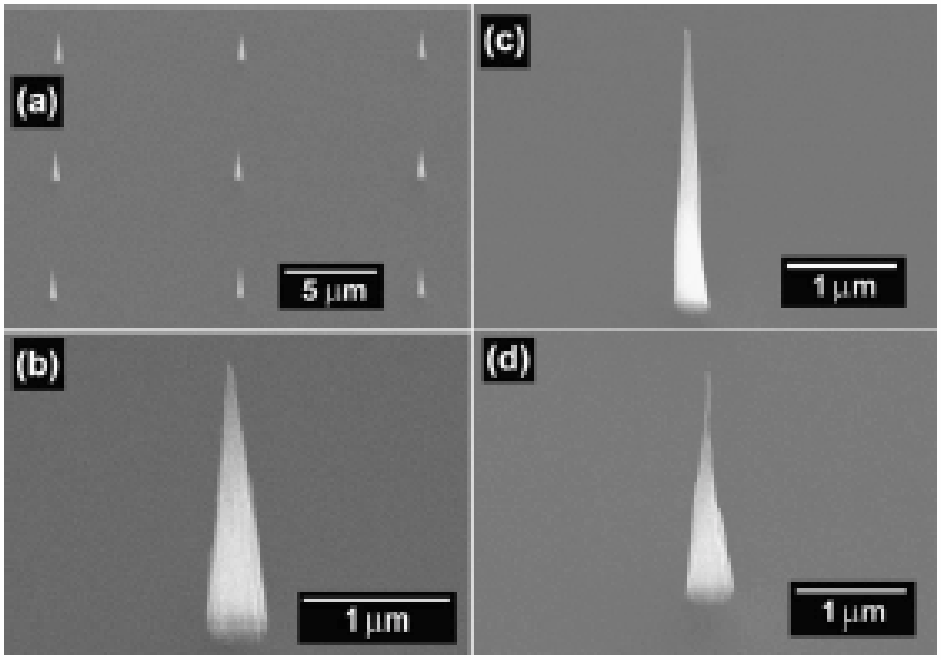

Fig. 2.3 (a) A SEM image of an array of carbon nanocones fabricated using dc PECVD. (b) and (c) Nanocone structures with the cone angle of 15° (b) and 5° (c). (d) Nanoscale cylinder-on-cone carbon tip synthesized by first growing a carbon nanocone with a higher C_2H_2/NH_3 ratio, followed by growing a carbon nanofiber with a relative low C_2H_2/ NH_3 ratio. [29]

surface and materials may localize power dissipation through arcs instead of the glow discharge.

2.1.2 Microwave PECVD

MPECVD is another common approach to fabricate VACNFs. In microwave discharges, the plasma takes on the character of a free electron gas, offering a high density of high energy electrons, and dissociating CH_4 with a high degree of conversion.

Choi *et al*. have reported the growth of VACNFs on Ni-coated Si substrates by MPECVD with a mixture of methane and hydrogen gases at about 700^{o}C.[38] The preparation of high-density VACNF forests on silicon, quartz and ceramic substrates has also been reported by using a microwave plasma at about 700^{o}C with the aid of iron oxide particles. Cui *et al*., have also reported successful growth of CNFs via MPECVD.[31]. The deposition system used in this study was a 915 MHZ MPECVD reactor. The substrates were prepared by sputter depositing a 10 nm thick iron film onto oxidized Si wafers. Prior to deposition, the iron-coated substrates were pretreated in ammonia gas plasma for four minutes. Following the pretreatment, methane gas was introduced into the reactor for the start of the deposition stage. The nanofibers were well aligned with a high aspect ratio and the growth direction normal to the substrate. The fibers possessed a bamboo-like structure, and the interbamboo-layer distance varied as the growth temperature and methane/ammonia ratio changed.

It is worth noting that although forests and towers of VACNFs have been grown by MPECVD, there is still no report for the growth of isolated individual VACNFs by this method. The reason remains unclear at this point.

2.1.3 Inductively coupled PECVD

Inductively coupled PECVD chambers are relatively simple to construct (no external magnets) and offer high ionization efficiency compared to dc or rf capacitive discharges. This approach uses an inductively coupled plasma source with an independent rf power supply to the electrode holding the substrate. Fig. 2.4 gives an example of the experimental set-up for this technique, which was constructed by Delzeit *et al*. [32] This ICP reactor has a pair of electrodes. The upper electrode consists of a six-turn copper coil, which is connected to the RF power source as a part of a high Q network. Resonance currents circulating through the coil produces a magnetic field that induces electron currents in the plasma. The lower electrode is heated by a resistive coil heater and its temperature is controllable. Both the lower electrode and inductive coil are powered by a rf generator.

Delzeit *et al*. have been using such a system and have successfully fabricated VACNFs. Methane and hydrogen gas mixtures were employed during the process, and the chamber pressure was kept at 3 Torr. Thin layers of Al/Fe were used as the catalyst. A detailed parametric study varying inductive power, pressure, temperature, gas composition, catalyst thickness, and power to the substrate was conducted. It was observed that the power in the lower electrode holding the substrate influenced the morphology of growth products and results in a transition from MWCNTs to nanofibers as the power was increased. Optical emission spectra taken during the process indicated that as the hydrogen emission intensity increased, VACNFs were obtained.

Caughman et al. have also explored the growth of VACNFs using this technique, but at a significantly lower pressure (below 100 mTorr).[39] Low pressure operation is considered

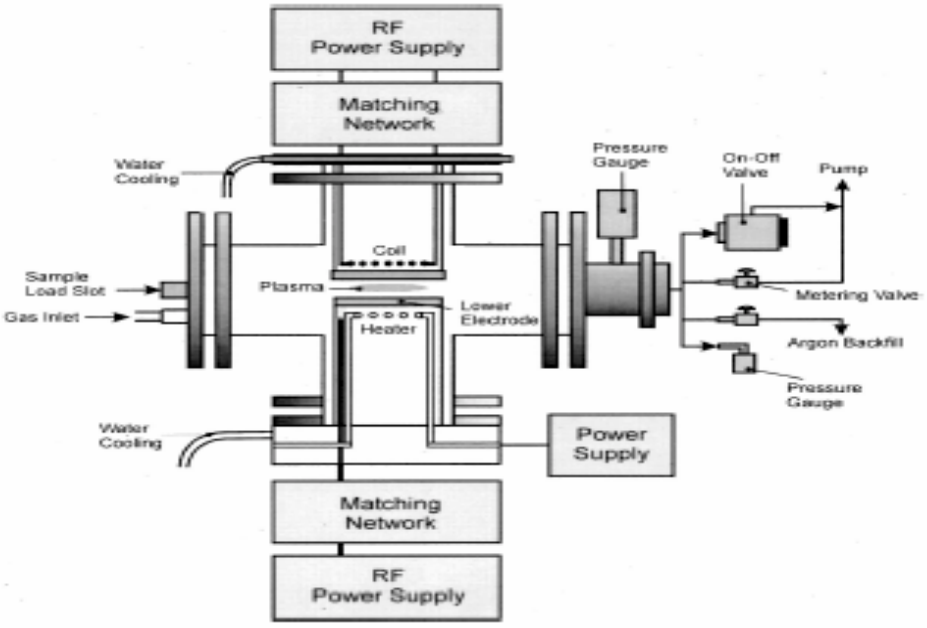

Fig. 2.4 Schematic of an ICP reactor.

to be potentially advantageous, since, in this case, plasma uniformity is increased as the pressure is decreased. The experimental set-up was very similar to that of Delzeit and coworkers, except that a mixture of acetylene (C_2H_2) and hydrogen (H_2) was used as the carbon source and etchant gases, respectively, and Ni served as the catalyst. In this case, both forests of nanofibers and isolated nanofibers were successfully grown, as shown in Fig. 2.5. Continuous nickel thin films (~15 nm thick), deposited on a buffer layer of tungsten–titanium alloy, and a pattern of 100 nm diameter nickel dots (~10 nm thick) with a titanium buffer, were used for forest and isolated VACNF growth, respectively.

Since the operating pressure maintained for Caughman's experiments is significantly lower than that for most PECVD processing (~2-10 Torr), there is a considerable difference in the plasma chemistry. For example, the mean free path for acetylene neutral collisions at lower pressure is much less than that at normal pressure. This in turn results in slower reaction rates for gas-phase interaction and slower growth rate of VACNFs. In addition, there is no apparent effect of bias voltage on the plasma chemistry for the low pressure case, which is in sharp contrast to what has been observed by Mayyappan *et al.*.[32] Still, in both cases, the plasma conditions were directly related to growth results.

2.2 VACNF growth mechanisms

Most PECVD grown carbon nanofibers possess herringbone or bamboo-like structures, as shown in Fig. 2.6. Tip growth mode, in which the catalyst particle is encapsulated in the tip of the fiber, is seen most often.

A few basic aspects have been widely acknowledged about the growth of VACNFs. It is understood that acetylene, methane and a variety of other carbonaceous gases play the

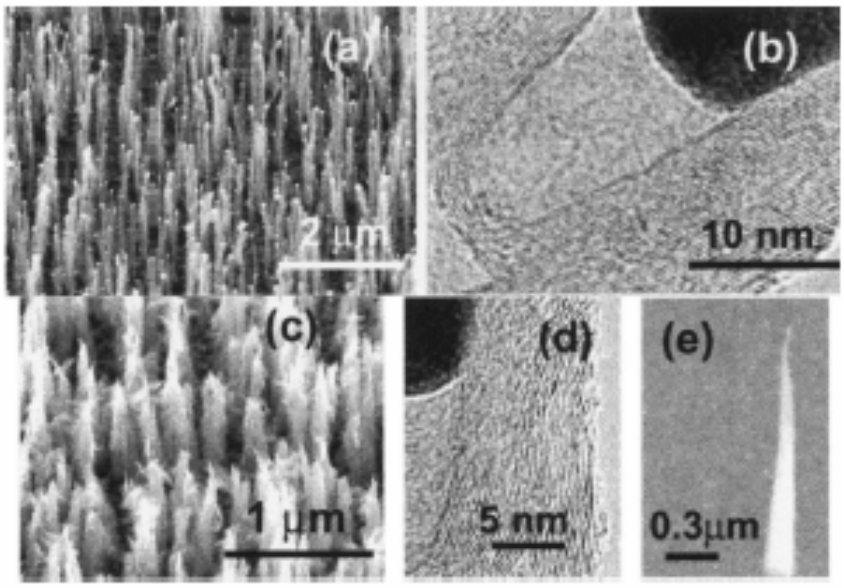

Fig. 2.5 SEM images of carbon nanofibers showing forest of nanofibers grown in (a) hydrogen-rich plasma, (c) carbon-rich plasma, and (e) isolated nanofiber grown in hydrogen-rich plasma. TEM images taken near the catalyst base for the hydrogen-rich plasma (b) and the carbon-rich plasma (d).[39]

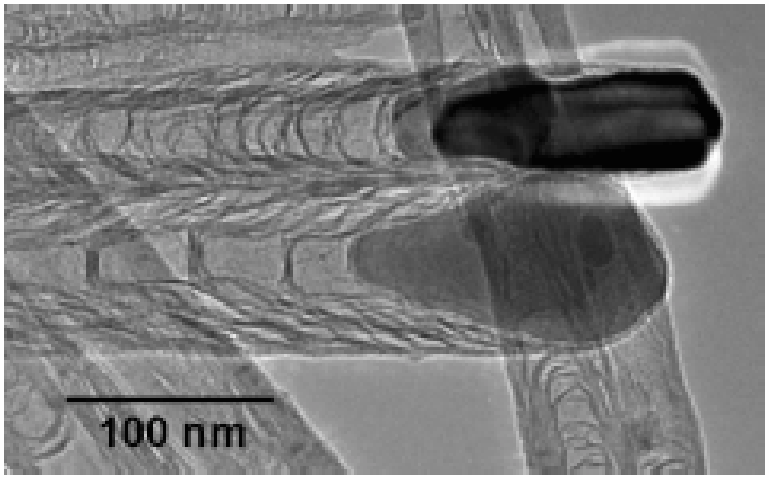

Fig. 2.6 A TEM image of VACNFs showing a herringbone-like structure.[26]

role of carbon feedstock, while ammonia and hydrogen act as etchant gases. As the gases are disassociated, carbon radicals with positive charge are accelerated towards the substrate, diffuse through the negatively charged catalyst particles, and start precipitating out after the particles become supersaturated with carbon. If the interaction between the catalyst and substrate is weak enough, the catalyst particle is lifted off the substrate, and VACNFs start growing. The carbon layers formed beneath the catalyst usually resemble the shape of the catalyst particle. As the diffusion and precipitation process continues, the VACNFs grow taller. The catalyst particle functions as an etch mask preventing degradation of the VACNFs during growth.

Still, various growth models of bamboo-like structures have been proposed in a variety of works. Saito suggested an intermittent growth model whereby layers of graphite would form on the catalyst surface until the accumulated stresses in the system would propel the nanofibers (or catalyst particles) away from each other creating a fresh surface for subsequent graphite nucleation.[40] An alternate proposal by Kivaleski suggested that a bamboo-like structure could form when the new graphitic sheath grows more quickly than the catalyst moves away from the existing fiber.[41] The growth mechanisms of such bamboo-like structures remain controversial despite all efforts made to both experimentally and theoretically validate competing theories. More information, such as the composition variation along the CNFs, and detailed catalyst particle-graphite interface studies, is necessary for a more knowledgeable explanation of this bamboo-like structure growth.

2.3 Alignment mechanisms

The alignment of carbon nanofibers can be controlled by several mechanisms, as proposed by different research groups.

Our group has demonstrated that the CNF alignment is mainly controlled by the direction of the electric field lines during the synthesis process.[42] Guided by this model, controlled alignment of catalytically grown CNFs at a variable angle to the substrate during a plasma-enhanced chemical vapor deposition process was achieved. Off-normal CNF orientations were also achieved by positioning the sample in the vicinity of geometrical features of the sample holder, where bending of the electric field lines occurred. The controlled growth of kinked CNFs that consist of two parts aligned at different angles to the substrate normal also was demonstrated. Figure 2.7 shows SEM images of such fibers.

In addition, the alignment of CNFs is also affected by the growth mode (base or tip) of the nanofiber.[29] In this case, the alignment mechanism of VACNFs is proposed as a feedback mechanism associated with a non-uniform stress (part tensile, part compressive) that is created across the interface of the catalyst particle with the CNF due to electrostatic forces, regardless of where the particle is located (tip or base) (Fig. 2.8). When the particle is at the top, such a feedback process equalizes the growth rate everywhere, and vertical orientation is maintained . By contrast, if the particle is at the base, this feedback process accelerates the growth on one side of the nanofiber, causing further bending of the structure.

The shielding effect of neighboring VACNFs also plays a role in helping the aligned growth of CNFs by affecting both the diffusion of carbon through the catalyst

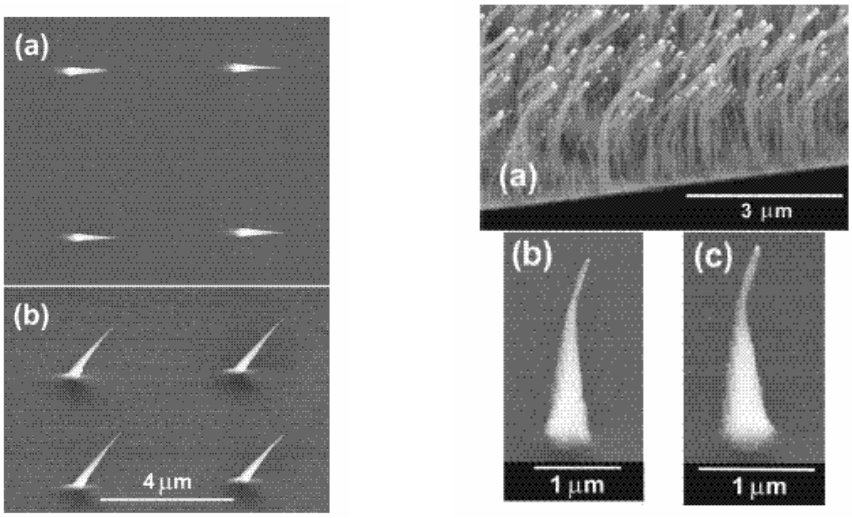

Fig. 2.7. Left SEM images were taken at (a) 0^{o} and (b) 45^{o} tilt angles, of an array of individual CNFs grown in the vicinity of the substrate/ sample holder edge. Right SEM images: (a) a forest of and (b) individual kinked CNFs (KCNFs).[42]

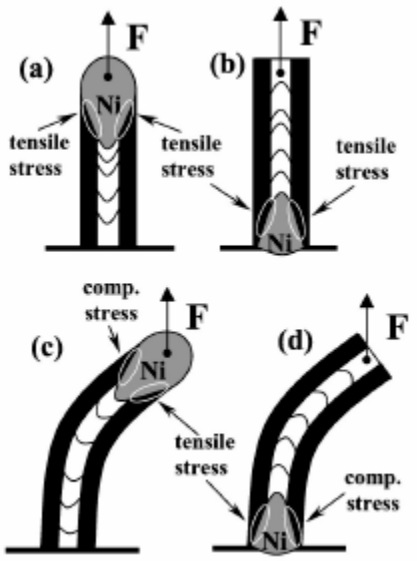

Fig. 2.8 Alignment mechanisms of carbon nanofibers. If a CNF grows vertically along the electric-field lines, electrostatic force *F* creates a uniform tensile stress across the entire catalyst particle/nanofiber interface, regardless of whether the particle is located at the tip (a) or at the base (b). If during the growth the CNF starts to bend due to spatial fluctuations in carbon precipitation at the particle/nanofiber interface, nonuniform stresses are created at the particle/nanofiber interface. For the nanoparticles at the tip (c) and at the base (d) the stresses are distributed in the opposite way, which leads to the nanofiber alignment in the first (c), but not in the second (d) case. White ellipses indicate the interface regions where the stresses occur.[29]

nanoparticle and subsequent precipitation at the nanofiber and nanoparticle interface. Moreover, it has been proposed by Dai and coworkers that the crowding effect helps the alignment in some dense CNF films.[43]

In summary, growth of vertically aligned CNFs is of prime importance to enable both fundamental studies and potential applications of these fibers. Different techniques for growing aligned CNFs are briefly surveyed in this chapter. Accomplishing large-scale growth of aligned arrays of carbon nanofibers with desired functionality is the ultimate goal that will likely remain a challenging research area for the foreseeable future.

Chapter 3 Experiment

Three types of PECVD-grown vertically aligned carbon nanofibers (VACNFs) have been studied in this work: dc PECVD carbon nanofibers grown by Dr. Vladimir I. Merkulov of our group, inductively coupled PECVD fibers provided by NASA Ames Research Center, and low-pressure inductively coupled PECVD fibers grown by Dr. John B.O. Caughman of the Fusion Energy Division in the Oak Ridge National Laboratory. All the fibers were grown in the form of forests, with Ni serving as the catalyst, and Si as substrates.

The experimental plan consisted of four major parts: characterization of as-grown VACNFs both structurally and compositionally, e-beam lithography to define electrodes on VACNFs, photolithography to pattern big pads (~ 600 um), and four probe charge transport measurements.

The first step was to characterize the VACNFs with various techniques, such as SEM, TEM, STEM, Auger and EDX, gaining a basic understanding of the structure and composition distribution of these fibers.

The characterization step was followed by e-beam lithography. VACNFs were removed from the substrate by scratching with a needle and were dropped onto a Si/SiO_2 chip on which alignment marks had been defined. The position of individual VACNFs was mapped relative to the alignment marks by SEM. PMMA was spun onto the substrate, and was then patterned by electron beam lithography and resist removal. After a reactive ion etch (RIE), Ti and Au were deposited on the substrate, and lift-off was performed, leaving patterned electrodes on the fibers.

In order to perform temperature dependence measurements of electric resistance, big square pads with a size of about 600 um were defined by photolithography, followed by e-beam metal evaporation and lift-off prior to dropping the fibers onto the substrates. Electrodes were then patterned by e-beam lithography, as described above.

Four probe charge transport measurements were performed in air at room temperature using a HP analyzer and a Signatone four probe station. Temperature dependence measurements were carried out in an Oxford Instruments refrigerator.

In the following text, the growth conditions of three types of fibers used in this work are presented at first; the four major experiment steps are then explained in detail.

3.1 Growth of three types of VACNFs

Prior to the growth of carbon nanofibers by dc PECVD, 10 nm thick Ni film was deposited onto a Si substrate by e-beam metal evaporation. After dc plasma pre-etching with ammonia at 375^{o}C (ammonia flow rate: 80 sccm), dc PECVD was initiated to grow vertically aligned carbon nanofibers. A mixture of acetylene and ammonia was used in this process (flow rates of acetylene and ammonia: 30 and 80 sccm). Growth temperature was about 720^{o}C, the total gas pressure during the growth was about 3 Torr, the dc glow discharge current was 100 mA, and the discharge voltage was about 510 V. The total growth time was 2 hours. Refer to Figure 2.1 for detailed experimental set up for the dc PECVD process.

A schematic of the ICP reactor is shown in Fig. 2.4. In this growth process, a catalyst film was sputtered onto a silicon substrate by ion beam sputtering. After loading the substrate, purging the chamber with argon and heating the substrate to the desired

temperature, the methane-hydrogen gas mixture was introduced and the reactor pressure was set to the desired value. The capacitive power to the lower electrode and the inductive power to the coil were turned on and a plasma was ignited. For the specific sample studied in this work, the catalyst was 10 nm thick Ni film. The inductive power to the coil was 100 W, and the capacitive power to the lower electrode was 200 W. Both the lower electrode and inductive coil were powered by separate 13.56 MHz rf generators with their associated matching networks. The gas flow rates for C_2H_2 and H_2 were 20 and 80 sccm respectively. The growth temperature was 900^{o}C, the pressure was set at 3.6 Torr, and growth time was 10 minutes, with a bias of -430V.

As to the low-pressure inductively coupled PECVD technique, the set-up of the ICP reactor is very similar to that of the inductively coupled PECVD reactor in Fig. 2.4. The major difference between these two growth methods is that an inductively coupled plasma source operates at a very low pressure of ~50 mTorr for the former, in contrast to that of ~ 2-4 Torr for the latter. For the sample studied in this work, the inductively coupled plasma source was operated at 13.56 MHz. A continuous Ni thin film (15 nm thick) was deposited on a buffer layer of tungsten-titanium alloy (100 nm thick). The nickel catalyst was exposed to a pure hydrogen plasma for ~ 6 minutes to remove any native oxide that may have formed. Acetylene and hydrogen were used as the carbon source and etchant gases, respectively. The flow rate of acetylene was 20 sccm and of hydrogen 150 sccm. A source rf power of 1 kW and a substrate bias of -200 V were used for the growth. The growth temperature was ~ 700^{o}C, and the growth time was ~ 2 hours.

3.2 Characterization of VACNFs

Several techniques are employed to characterize the three types of VACNFs. Scanning electron microscopy (SEM) (Hitachi 4700) was primarily used to take images of as-grown fibers and measure the fiber heights. To investigate the detailed interior structures of individual VACNFs, transmission electron microscopy (TEM, HF 2000) was utilized. Scanning transmission electron microscopy (STEM, HD 2000) was employed to map the elemental distribution along individual fibers. In addition to STEM, Auger electron spectroscopy (AES) was also used to investigate compositional variation along the fibers.

Samples for TEM and STEM studies were prepared in the same way. The fibers were scratched off from the substrates and dropped onto a TEM copper grid laced with carbon film. Auger electron microscopy sample preparation was done by scratching fibers from the substrate and dropping them on a chip with pre-defined alignment marks.

3.3 E-beam lithography

3.3.1 Overview

E-beam lithography, a special technique for creating very fine patterns, was used in this work to pattern electrodes on individual laid-down carbon nanofibers. This technique employs a beam of electrons scanning across a surface covered with a resist film sensitive to those electrons, thus depositing energy in the desired pattern in the resist film. Several unique features of this technique are: (1) it can produce patterns with very high resolution down to 20 nm or less without using a mask; (2) it can be used on various materials and writes almost any arbitrary patterns; (3) most of the time it needs specially designed

alignment marks to accurately locate the position of patterns-to-be-written; and (4) due to the scanning mode of electrons to cover an area, it is very slow. Therefore, e-beam lithography is excellent for working on very fine features that cover small areas. It has found a wide variety of applications where the features of e-beam lithography are needed and the drawbacks can be tolerated.

Among the most popular commercial e-beam writing systems are JEOL JBX Gaussian vector scan system and Leica lithography systems. These tools are very expensive and complicated, and they require frequent service to stay properly maintained. However, in this dissertation, all the e-beam lithography work was performed by using a relatively low-cost, flexible and reliable SEM conversion system, the nanometer pattern generation system (NPGS).

3.3.2 Nanometer pattern generation system (NPGS)[44]

NPGS was created by J. C. Nabity in 1988 when he was a PhD student. The main component in this system is a Windows-compatible PC with an ISA bus. A schematic of the PC set-up is shown in Fig. 3. 1. The CPU of this PC reads the DesignCAD data to generate the shape filling data, and feeds these data to a 16-bit wide digital-to-analog converter (DAC), which drives the scan coils of SEM in both X and Y directions. The blanking control board provides the signals for blanking control of electron beams while writing. The writing is carried out in a so-called vector-scan strategy, i.e., the beam is deflected from shape to shape in a writing field.

Other main hardware includes a specially designed SEM sample holder, which has a built-in Faraday cup and gold-coated carbon standard, a picoammeter, which is connected

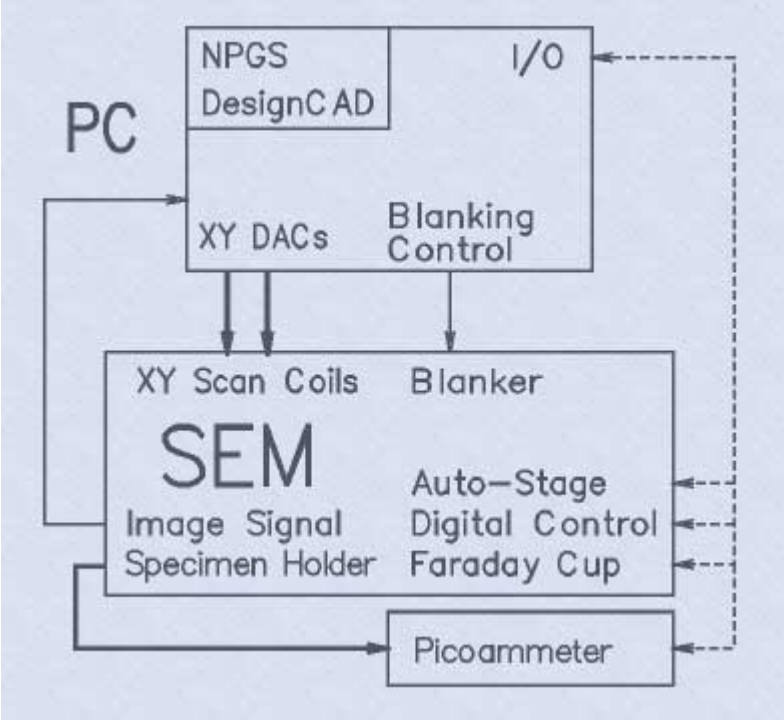

Fig. 3.1 A schematic of experimental set up of NPGS.

to the Faraday cup of the sample holder and used to measure the beam current hitting the sample surface, and a beam blanker, consisting of a pair of plates set up as a simple electrostatic deflector. To turn the beam off, a voltage is applied across the plates. This deflects the beam off the axis and thus avoids hitting the writing area.

There are three basic steps to the pattern generation process: pattern design, parameter run file creation, and pattern writing with alignment for multilevel lithography. First, patterns are generated using DesignCAD, which is capable of handling arbitrary shapes. Patterns can be designed in different drawing layers and different colors according to the exposure conditions. Once the patterns are created, the exposure conditions for different elements, such as alignment condition, dose, beam current, writing sequences, and repeating times of certain elements, are input to a Run File. After a Run File is generated, the pattern can be written using the program NPGS by simultaneously controlling the X-Y scan coils and beam blanking of the SEM. As to the alignment, patterns can be aligned to existing alignment marks without exposing the writing area by using the alignment program.

Several unique features of NPGS system are: 1. Arbitrary polygons can be designed with up to 200 vertices, and the way of filling these polygons can be specified by users; 2. The users have control over the exposure dot-to-dot spacing in both X and Y directions, and can effectively avoid edge roughness of the patterns; 3. A transformation matrix is used to match the existing alignment marks and the designed overlays, which provides more accurate positioning of the pattern; and 4. NPGS can control motorized stages, providing fully automated sample movement and pattern alignment.

Although NPGS has these advantages, there are still some limitations, mainly due to its

close connection to SEM. SEM stages are typically orders of magnitude slower than those of dedicated e-beam tools, and do not provide feedback to the deflection system. The accuracy of the movement of SEM stage is also not comparable to that of dedicated e-beam tools. Another drawback is observed with writing over large areas, when the distortion due to electron optics of the SEM becomes significant. Therefore, NPGS is most suitable to write small patterns with a short period of writing time, instead of large area grating or any application requiring a large substrate.

3.3.3 Process

The e-beam lithography SEM used in this work is a Hitachi-4700, which has a cold field emission filament. The typical SEM set-up for performed e-beam lithography consists of an accelerating voltage of 30 kV with an emission current of 15 μA, a 30 μm aperture, a beam blanker at "external" mode with the voltage of 50 V, and a measured beam current of ~ 20 pA. A specially designed sample holder was used to mount Si/SiO_2 chips with coated resist. The beam current on the sample surface was measured by a Keithley picoammeter, which is in connection with the Faraday cup in the sample holder.

Polymethylmethacrylate (PMMA) (495 k, A8) was used as the e-beam resist. PMMA is a standard positive e-beam resist and remains one of the highest resolution resists available. It is dissolved in anisole with a weight concentration of 8%. As the electrons penetrate the resist, the resist undergoes structural changes, with big molecules breaking into smaller fraction. After development in a MIBK: IPA (1:3), the exposed regions dissolve away. In this work, PMMA and MIBK were both purchased from MicroChem Corporation.

The process for e-beam lihtogrpahy performed in this work is schematically shown in Fig. 3.2. First, VACNFs were removed from the growth substrate by scratching with a needle and dropped onto a Si/SiO_2 chip on which alignment marks had been defined. The position of individual VACNFs was mapped relative to the alignment marks by SEM. Fig. 3.3 presents the selected VACNF with a higher magnification. PMMA was spun at 2300 rpm onto the substrate and baked at 170^{o}C for 15 minutes to achieve a thickness of ~800 nm, and was then patterned by NPGS SEM lithography. The SEM was a Hitachi 4700. The pattern was developed in MIBK: IPA (1:3) for 1 minute. Fig. 3.2 (c) presents an AFM image of a patterned VACNF right after the development. To assure successful four probe measurements, usually five or six electrodes were patterned on an individual CNF. After several seconds of reactive ion etch (RIE) (O_2 flow rate of 50 sccm, power 95 Watts), Ti (200 nm thick) and Au (200 nm thick) were deposited on the substrate, and lift-off was performed to leave patterned electrodes on the fibers. Fig. 3.2 (d) demonstrates a patterned VACNF device with five electrodes.

3.3.4 Problems presented in e-beam lithography

The problems encountered during e-beam lithography in this work mainly originated from three sources: the thick PMMA resist, the SiO_2 layer on top of Si chips, and the cold field emission SEM.

Most VACNFs used in this work had a diameter of about 200 nm, except for the fibers from NASA. The resist thickness has to be at least 4 times of that of the VACNFs, i.e., 800 nm, to assure good quality metal deposition. Such a thick resist caused many problems, especially some feature size errors in the writing process due to forward

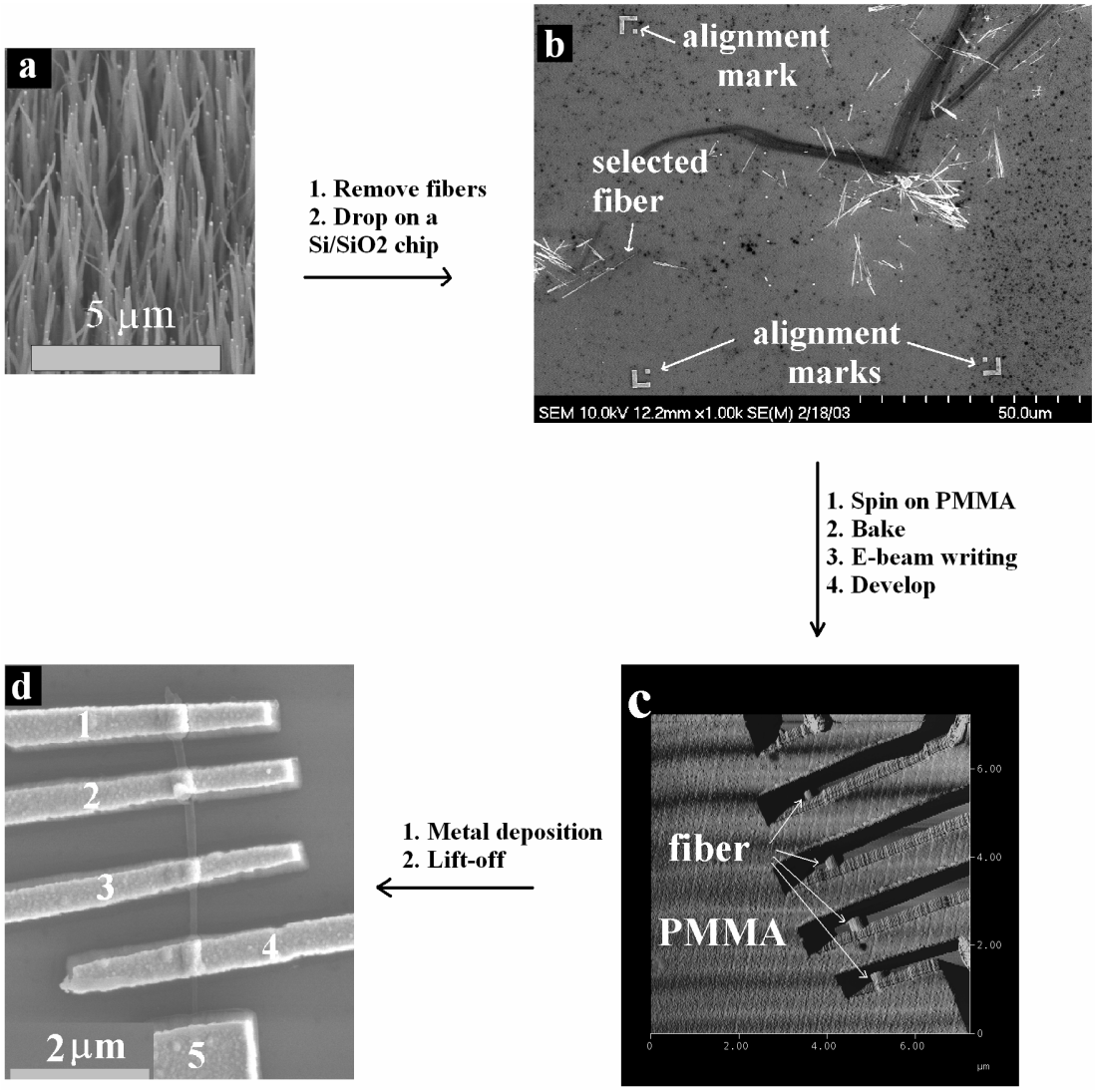

Fig. 3.2 A flow chart of the e-beam lithography process performed in this work. (a) A SEM image of the as-grown dc PECVD VACNF forest. (b) A SEM image of VACNFs dropped onto a Si/SiO_2 substrate. (c) An AFM phase image of a VACNF after e-beam writing and development of PMMA. (d) A SEM image of a patterned VACNF device with 5 electrodes.

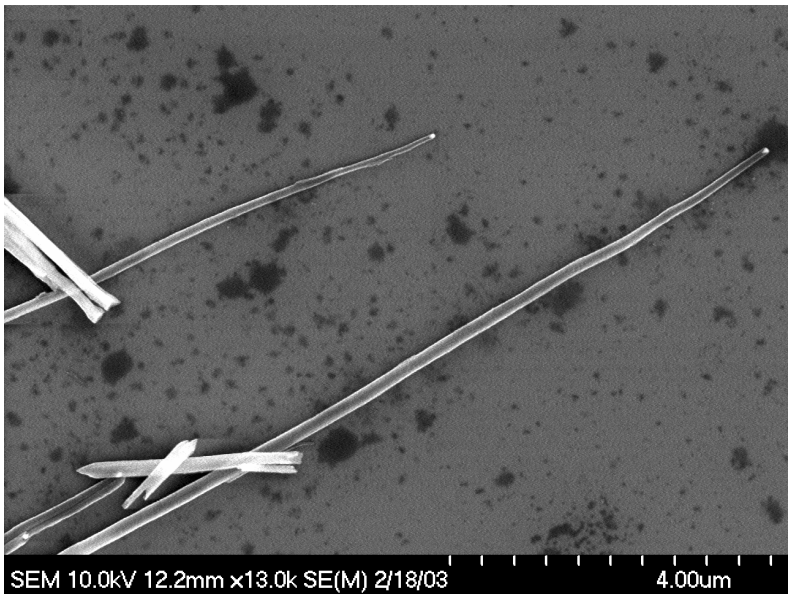

Fig. 3.3 A SEM image of the selected VACNF in Fig. 3.2 (b), with a higher magnification.

scattering of electrons. As the electrons penetrate the resist, they experience forward scattering, which broadens the initial beam diameter, and backward scattering, which causes the proximity effect. For forward scattering, the increase in the beam diameter in nanometers is given in an empirically determined formula $d_f = 0.9\ (R_t/V_b)^{1.5}$, where R_t is the resist thickness in nanometers and V_b is the beam accelerating voltage in kilovolts.[45] For R_t = 800 nm and V_b = 30 kV, with the original beam diameter of ~ 2 nm at the resist surface, the increase in the beam diameter at the bottom of the resist is about 120 nm, accounting for 1/2~1/3 of the width of an electrode to be patterned. Such an enlarged beam inevitably decreases the writing resolution and increases the edge roughness. Another problem presented by the thick resist is due to the backward scattering. Backward scattered electrons may return back through the resist, causing additional resist exposure. As a result, larger areas are exposed than targeted (proximity effect). As the resist becomes thicker, more backward scattered electrons are trapped inside the resist and fewer can escape, causing the size of exposed features larger than those with thin resist. When the designed electrodes are close to each other with the spacing of only 400 ~ 600 nm, it is disastrous to have this proximity effect involved. The electrodes might touch and overlay with each other, resulting in a short circuit.

The SiO_2 layer on top of Si chips, which is to provide an insulating layer for subsequent charge transport measurements, gave rise to feature placement errors during e-beam lithography. Electron beam irradiation on Si/SiO_2 chips often causes charge buildup on the SiO_2 surface. When this happens, only a small fraction of the incident electrons is trapped in the resist, so the dose must be higher to expose the same pattern. Moreover, the excessive accumulation of charge on the sample shifts the beam position,

disturbs placement accuracy, and results in overlay errors. A shifted or distorted pattern, sometimes with a serpentine-shaped line, was often observed in this work after resist development. It is highly recommended to use SiO_2 layers which are as thin as possible to minimize this problem.

In addition to feature size errors and feature placement errors mentioned above, the SEM used in this process (Hitachi 4700) is sometimes blamed for unsuccessful pattern writing. The SEM has a cold field emission filament, which provides very high resolution imaging. However, its beam current is very unstable with regard to short term noise as well as long term drift, therefore creating serious problems for the e-beam lithography system. When the beam current suddenly changes during the writing process, the exposure time, which is calculated by NPGS based on the beam current and area dose input in the Run File, should be different from the original one. However, once the writing of patterns starts, there is no way to change the parameters, such as the exposure time, in the Run File. Consequently, some parts of the pattern get underexposed and cannot be developed away, whereas other parts might be overexposed and widened when the beam current increases or decreases to a certain degree. To make it worse, it is difficult to discern such spots until the sample is metallized and lift-off is done. By then, either a missing metal contact makes the whole device useless, or two electrodes might be found to touch each other and create a short, and it is too late to save the sample. A thermal emission SEM, which can provide very stable beam current for days, would be ideal for this e-beam lithography process.

3.4 Photolithography

Photolithography is used to define pads with relatively large sizes. E-beam lithography could be utilized to write these big pads, but it is very time-consuming. For example, to write a 300- μm square pad using e-beam lithography takes about 40 minutes. To carry out a four probe measurement, at least four pads need to be defined, so the total e-beam writing time would be over 2 hours for a single chip. In contrast to e-beam lithography, photolithography can be utilized to pattern these pads on a whole wafer in very short period of time.

In this work, the photomask was designed as shown in Fig. 3.4. The mask is the same size as the final image on the wafer (1x). Eight pads with the size of 600 um were patterned on one chip.

SPR 220 3.0 was used as photoresist. The resist was spun onto a wafer with predefined alignment marks at the rate of 4000 rpm for 1 minute. The whole wafer was baked at 90^{o}C for 90 seconds. Exposure was carried out on a Karl Suss contact aligner with 7 seconds of exposure time. Post-exposure bake was done at 120^{o}C for 90 seconds. The wafer was then developed in CD 26 for 2 minutes. After descum for 30 seconds, 20 nm thick Ti and Au were deposited onto the wafer through e-beam metal evaporation.

3.5 Charge transport measurements

For charge transport measurements of carbon nanofibers performed in ambient environment, four metal probes (Signatone, SM-35) were loaded on a Signatone station. With the aid of an optical microscope, these sharp probes were placed on four metal pads connected to electrodes, which were patterned on carbon nanofibers by e-beam

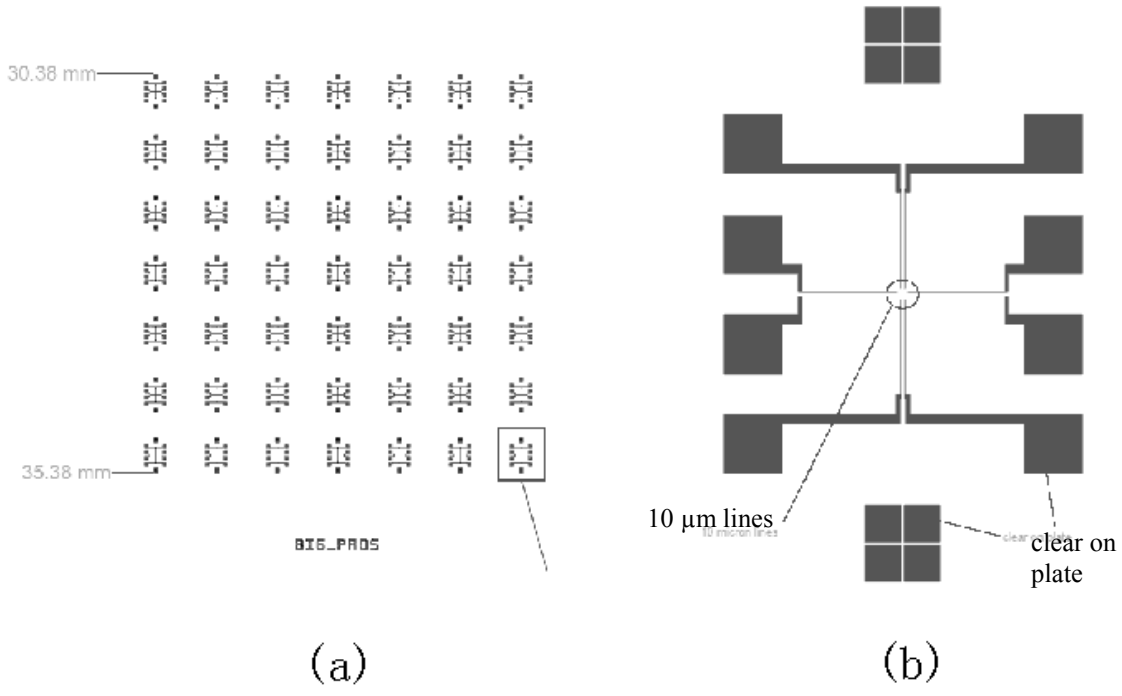

Fig. 3.4 Photomask design. (a) An overview of the 7x7 arrays. (b) The detailed layout of the unit in the square in (a).

lithography. A precision semiconductor parameter analyzer (HP 4156A) was utilized to apply voltage and record I-V characteristics.

For temperature dependence measurements of resistivity, the wires were glued to metal pads using silver paint, then the whole chip was placed into an Oxford Instruments refrigerator. The temperature range is from about 1K to room temperature.

Chapter 4 Structure and composition of dc VACNFs

As structure and composition are directly related to properties of VACNFs, much effort has been devoted in this work to studying the detailed structure and compositional distribution of Ni, Si, N and C along dc VACNFs. Scanning electron microscopy (SEM), transmission electron microscopy (TEM), Auger electron spectroscopy (AES) and energy dispersive X-ray analysis (EDX) have been utilized to characterize these fibers, and gain a basic understanding of the structure and composition distribution of these fibers.

4.1 Structure of dc VACNFs

Fig. 4.1 shows a SEM image of the dc VACNF forest. The height of the fibers was ~ 10 μm. The catalyst particles were encapsulated at the tips of fibers. Most fibers were straight, but a small portion of wavy fibers was also observed. Almost all the fibers were conical to some extent rather than cylindrical. The base diameter of fibers was ~ 200 nm, but at the tip, the diameter reduced to ~ 80 nm or less.

4.1.1 Interior structure of dc VACNFs

TEM studies revealed more details of the interior structure of dc VACNFs. The fibers had a highly defective herringbone-like structure with a central hollow region, and the Ni catalyst particles were completely encapsulated at the tip of the fibers (Fig. 4.2 (a)). It was also observed that the carbon layer formed beneath the catalyst resembles the shape of the bottom of the catalyst particle (Fig. 4.2 (b)). The fiber surface was free of amorphous carbon, and covered by many open edges of graphitic planes, as shown in Fig.

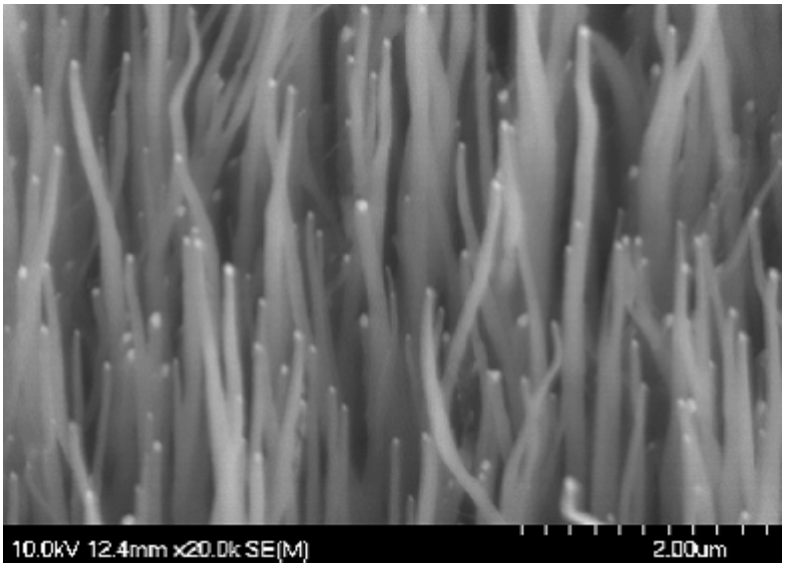

Fig. 4.1 A SEM image of dc VACNF forest.

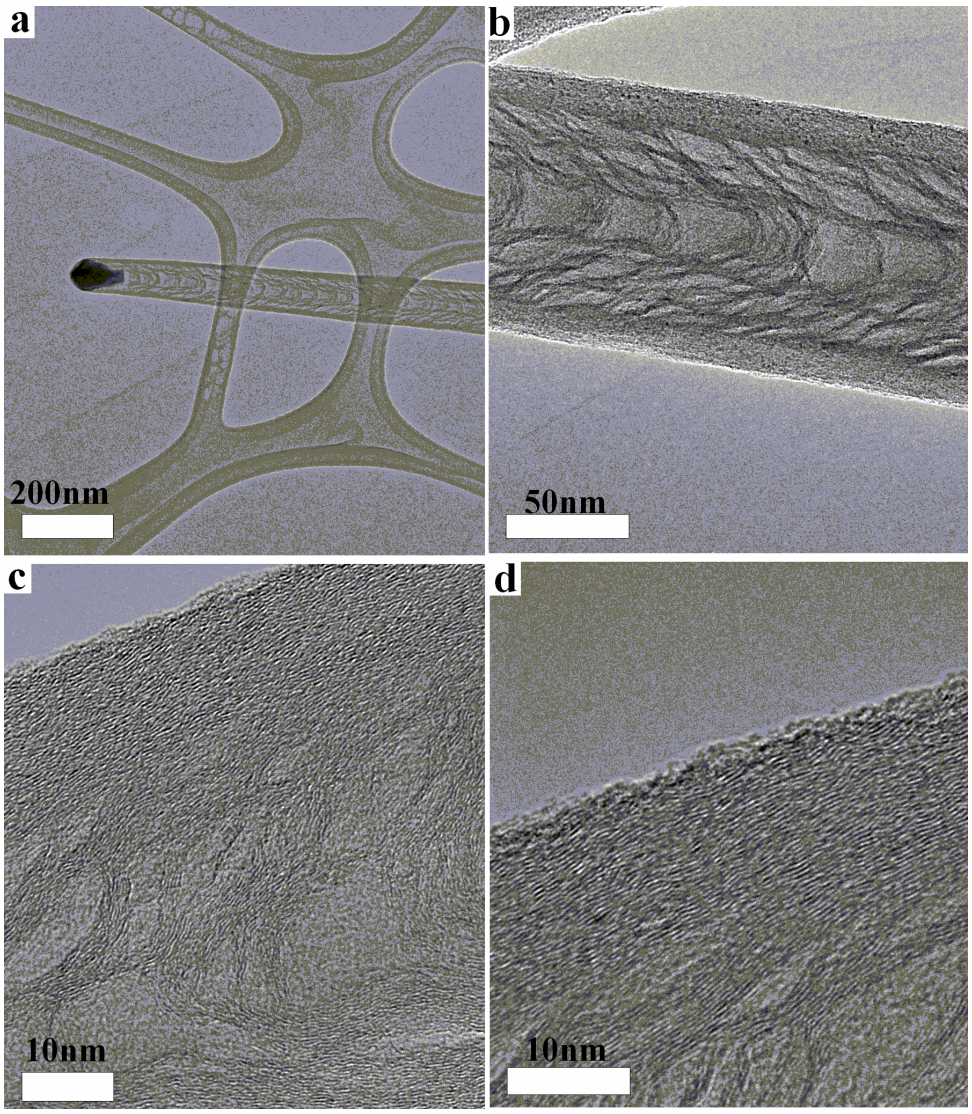

Fig. 4.2 TEM images of dc VACNF with a low (a) and a higher (b) magnification. (c) A high resolution TEM image of the detailed structure of a dc VACNF. (d) A high resolution TEM image. The open edges in the outer layer of dc VACNF can be readily observed.

4.2 (c) and (d). A graphitic outer layer was readily observed, which consisted of 30-45 semi-graphitic shells, and was generally 10-15 nm thick. High resolution TEM images revealed that in this layer the graphitic planes were not always parallel to the fiber axis but were often twisted and broken (Fig. 4.2 (d)). Some graphite structures perpendicular to the fiber axis were also visible, as shown in Fig. 4.3. Such "cross-struts" did not always continuously extend into the outer layer of the fiber, as they were often broken at various locations. Between the graphitic outer layer (region A in Fig. 4.4) and "cross-struts" (region C in Fig. 4.4), there was another layer with darker contrast (region B in Fig. 4.4). The darker layer became thinner toward the fiber tips. A schematic representation of the trunk structure of VACNFs is presented in Fig. 4.5. Mechanisms of these two regions are as follows: Region B most probably forms as a result of carbon precipitation due to supersaturation of carbon in the Ni particles, and thereby possesses a catalytic growth nature. In contrast, region A, the outer layer, may originate mainly from precipitation of carbon from glow discharge when a slight excess of acetylene is provided. This is in agreement with the growth mechanism of conical dc VACNFs proposed by Merkulov and coworkers.

It is also worth noting that most of the graphitic planes of region A were a continuation of those of region B, which implies that the outer layer was grown epitaxially from region B. In other words, the structure was composed of a herringbone-like core and an epitaxially grown outer layer. The occurrence of epitaxy can be attributed to the high growth temperature (~700^{o}C) and relatively long growth time (~2 h); the combination of both factors provides an environment similar to annealing. As the C ions and neutrals were captured by the sidewall of the fibers, they had enough

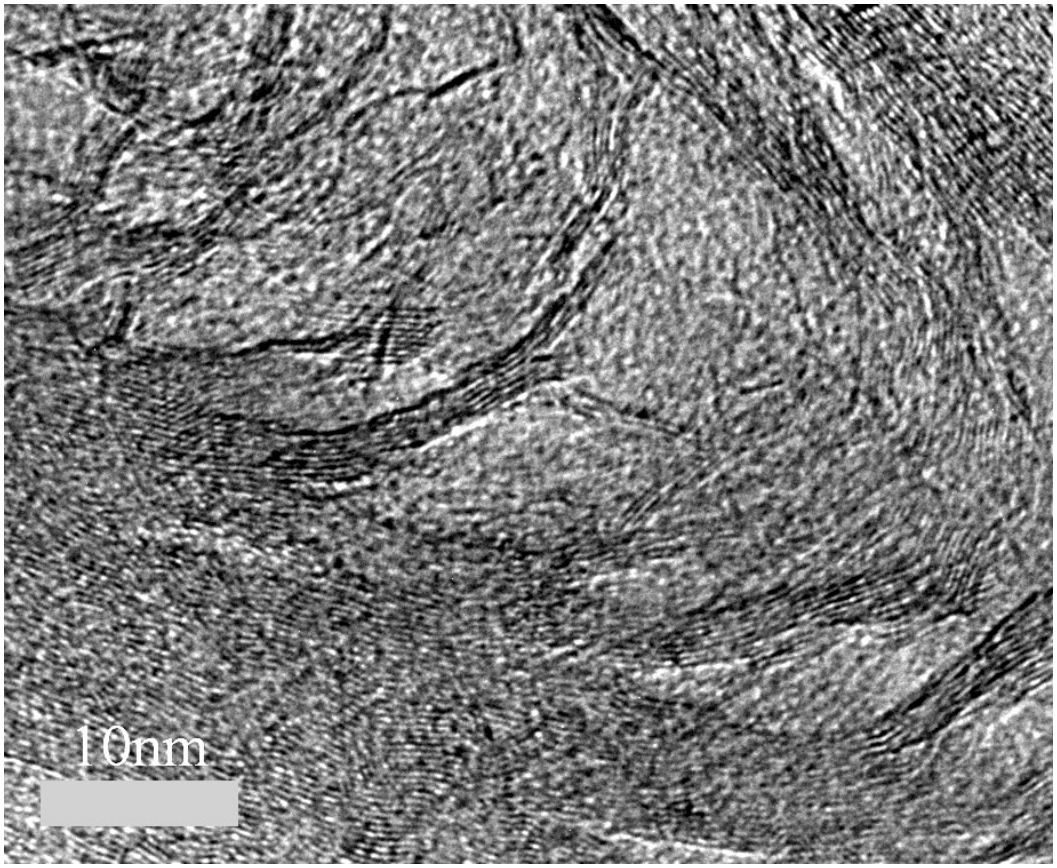

Fig. 4.3 A HRTEM image of the central "cross-struts'. The "cross-struts" were often discontinuous.

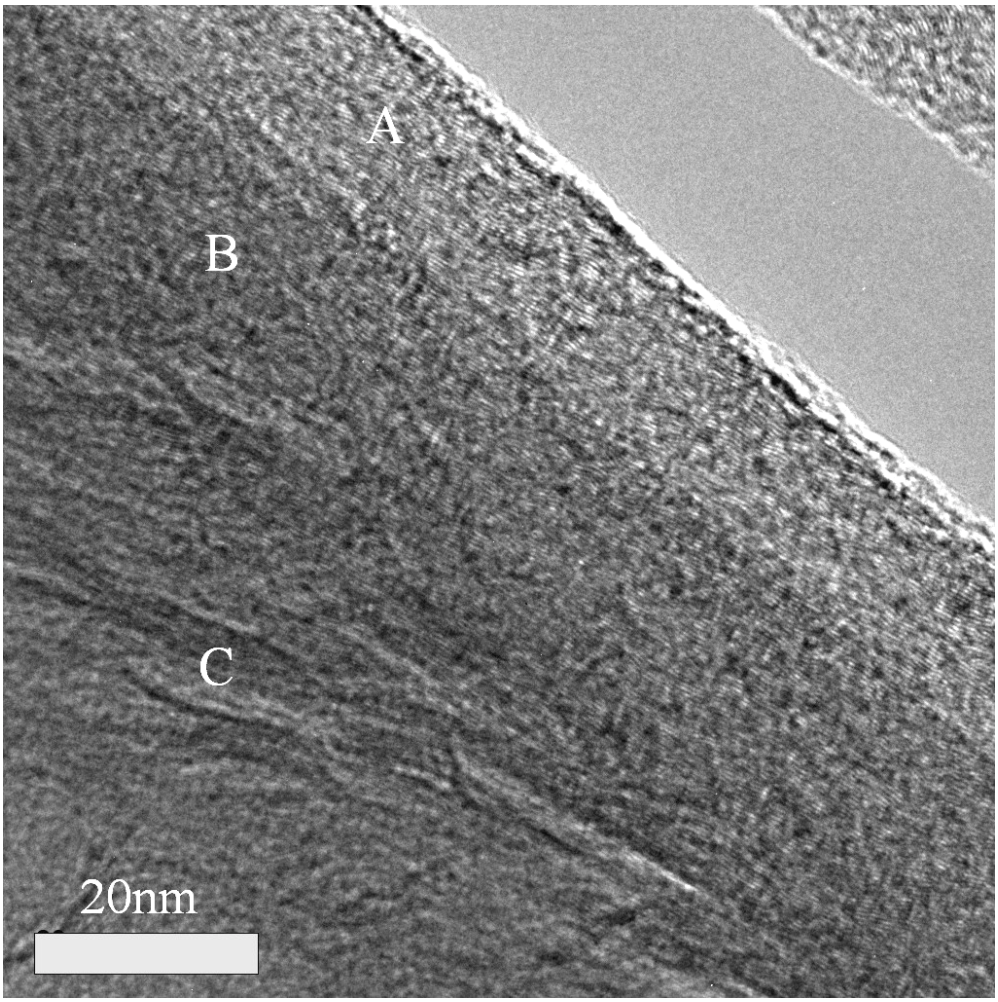

Fig. 4.4 A TEM image of a dc VACNF segment with a diameter of 120 nm. Region A: graphitic outer layer; region B: the layer with darker contrast; and region C: central "cross-struts".

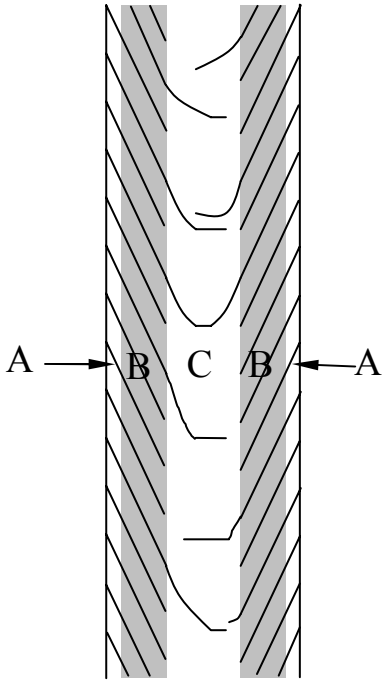

Fig. 4.5 A schematic representation of dc VACNF structure. Region A is the outer layer, region B has darker contrast, and region C contains the so-called “cross-struts”.

thermal energy and time to continue the growth of the already existing graphitic planes, keeping the energy of the whole system at a minimum.

As for the central cross-struts, their shapes changed frequently at various locations along the fiber length, and sometimes were discontinuous or only a portion of the particle contour. This indicates at least the shape of the bottom of Ni particles was frequently changed during the growth process, as the shape of the cross-struts is a replica of the Ni particle. The reason for the shape changing of Ni particle will be discussed in greater detail in a subsequent section of this text.

4.1.2 Tip of dc VACNFs

As for the tip of dc VACNFs, HRTEM studies indicated that the whole Ni particle was encapsulated by graphitic thin film and some amorphous carbon, as shown in Fig. 4.6. Between the teardrop shaped Ni particle and the graphitic thin film, there was a region with different contrast, as indicated by arrows in Fig. 4.6. Since the spacing of lattice fringes in this region was different from that of graphite and the Ni particle, it was most probably another material, say, some compound of Ni and C.

4.1.3 Wavy dc VACNFs

Wavy fibers were observed during the TEM studies; these fibers accounted for about one tenth of the whole fiber group. While wavy in morphology, they kept the overall alignment by growing upwards and perpendicular to the growth substrate. In these fibers, “cross-struts” still followed the contour of the catalyst particles, but the structure was twisted. Fig. 4.7 shows TEM images of one of these fibers. STEM studies indicated that

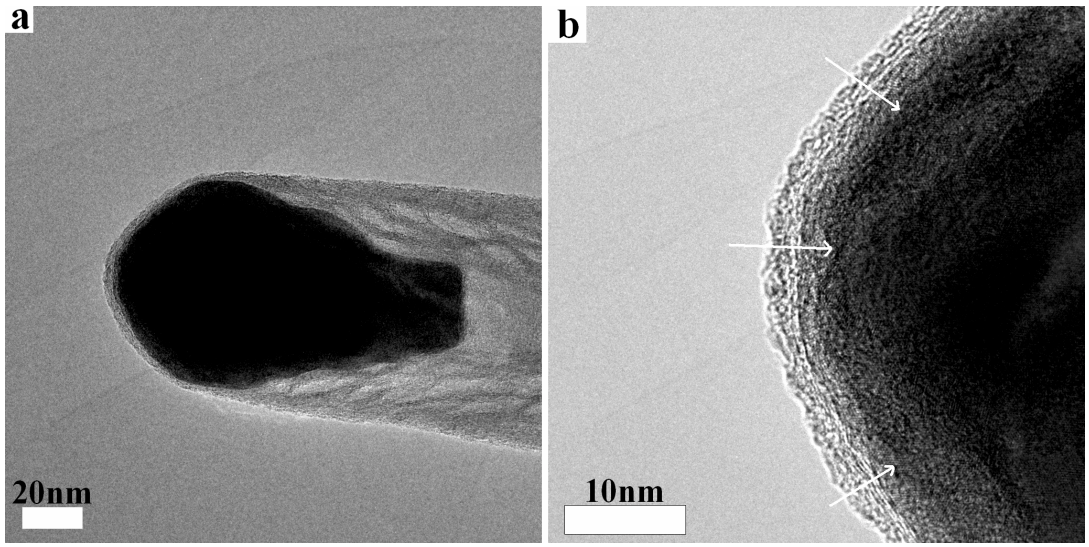

Fig. 4.6 (a) TEM image of a Ni particle at a dc VACNF tip. (b) HRTEM image of (a). Arrows indicate the regions that might be a compound of Ni and C.

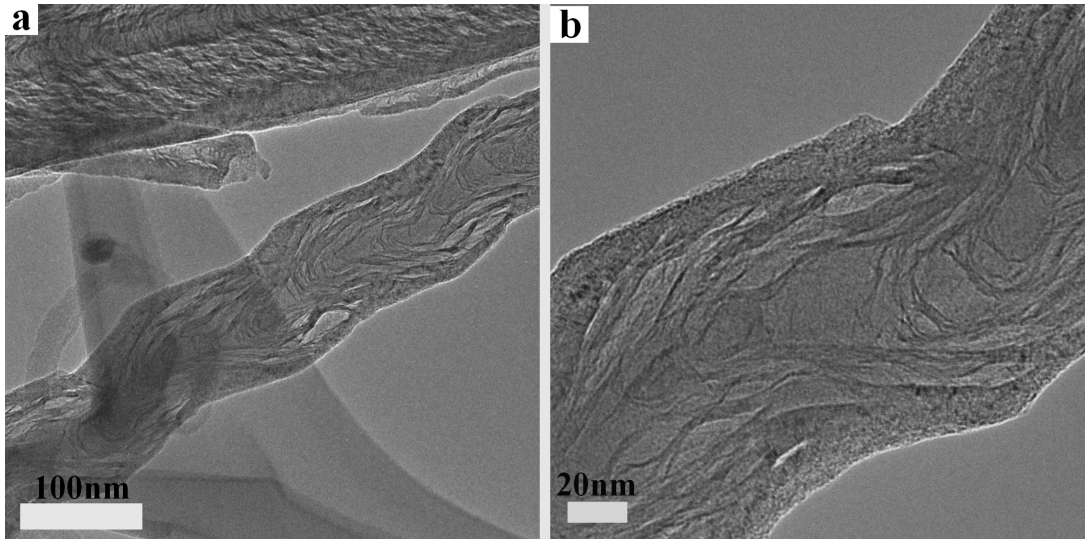

Fig. 4.7 TEM images of wavy dc VACNFs.

for these wavy fibers, small particles of Ni (diameters ranging 5 ~ 15 nm) were trapped in the middle of the fiber trunk, with spacing of 240 ~ 300 nm (refer to Fig. 4.8). It appears that the formation of these fibers was closely related to the presence of trapped Ni particles in the fiber body, as shown in Fig. 4.8. We propose the following explanations for the wavy fiber growth mechanism. After the growth of fibers was initiated, Ni particles were lifted off the growth substrate. As the growth continued, carbon precipitated out of Ni and formed graphitic layers beneath and around the catalyst. Ni was elongated and stretched at this moment, and the surface tension between Ni and carbon layer helped to hold Ni in place at this moment. As more and more carbon precipitated out, the surface tension could not hold the Ni particle any more. The Ni particle then jumped forward and left a hollow space behind. At certain locations around the Ni particle, most possibly highly defective regions, the surface tension between Ni and carbon layers was especially strong so that Ni and carbon layers were attached to each other to a great extent. While the major body of Ni struggled and jumped free, a portion of the Ni particle was torn off and trapped inside the fiber body. During this process, the large part of Ni did not move smoothly and follow exactly the direction of electrical field perpendicular to the substrate, but rather became oriented in another direction, due to the force generated during the torn-off process. This resulted in a slightly bent fiber. Under this circumstance, the electrostatic force F at Ni particle created nonuniform stresses (part tensile, part compressive) at the particle/nanofiber interface, as illustrated in Fig. 2.7 (c). These opposing stresses favored subsequent C precipitation at the interface experiencing tensile stress and led to higher growth rate at the interface; this negative feedback then acted, leading to the overall nanofiber

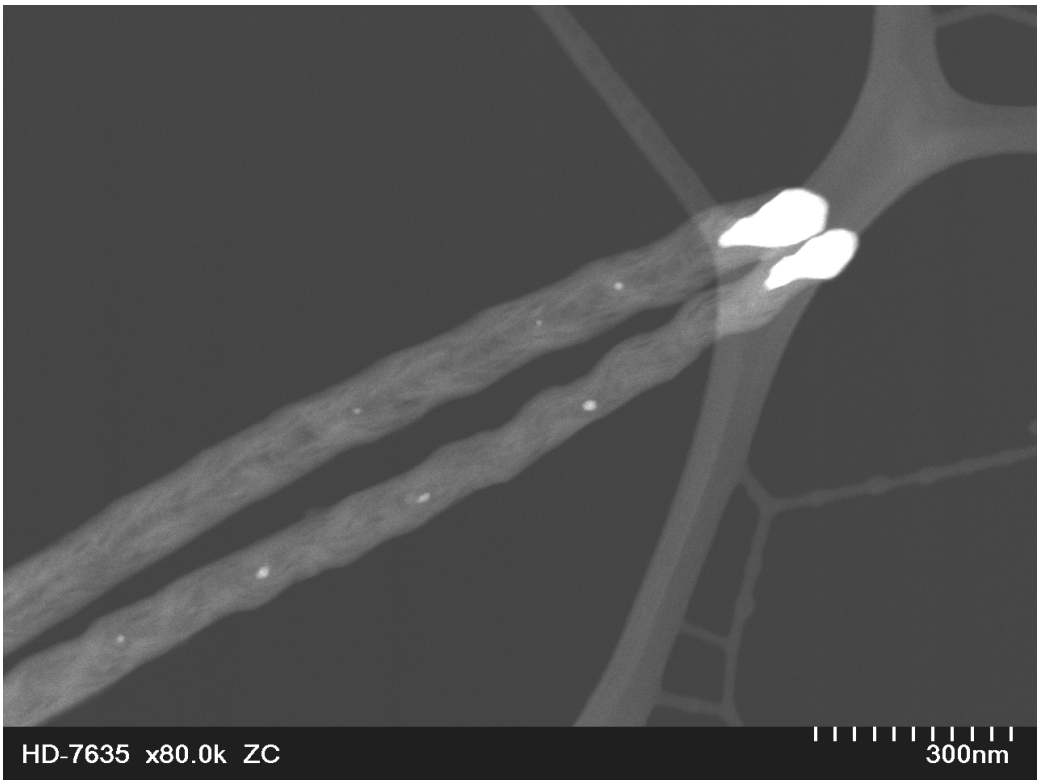

Fig. 4.8 Z-contrast STEM image of two wavy dc VACNFs. The white dots trapped in VACNFs are Ni.

alignment.[29] The whole process then repeated, winding up with a still vertically aligned carbon nanofiber but with wavy regions.

4.2 Composition of dc VACNFs

C, N, Ni, Si, and H are the elements involved in the dc VACNF growth. As dc VACNFs are composed of graphene sheets, carbon must be the dominant element. As ammonia is used in the growth process of dc VACNFs, it is expected that N becomes incorporated into the fiber body. Ni is mainly located at the fiber tip. Si may also be present in the trunk of fibers due to the use of Si substrates. Still, more efforts are needed to carry out detailed compositional studies of dc VACNFs. In this work, we systematically investigated this subject, and found that N, Si, Ni and O, were all present in the carbon fiber body. Why and how these elements became incorporated into the fibers will be discussed in this text.

EDX studies were conducted along the fiber length to get a better understanding of the elemental distribution along the fiber. The EDX instrument used in this work was attached to a STEM (HD 2000) with drift correction. This means that x-rays are collected solely from the fiber body, and without the drifting effect involved, the results are reliable and accurate.

First, an EDX point check was performed. Fig. 4.9 presents typical EDX spectra for an individual dc VACNF from different points. C, N, Ni and Si peaks can be discerned from all the spectra. The weight and atomic percent of each element is listed in Table 4.1. It can be clearly seen that C was the dominant element, and accounted for over 95% of the fiber. N was the second most prevalent element with the atom percentage over 1%. Si

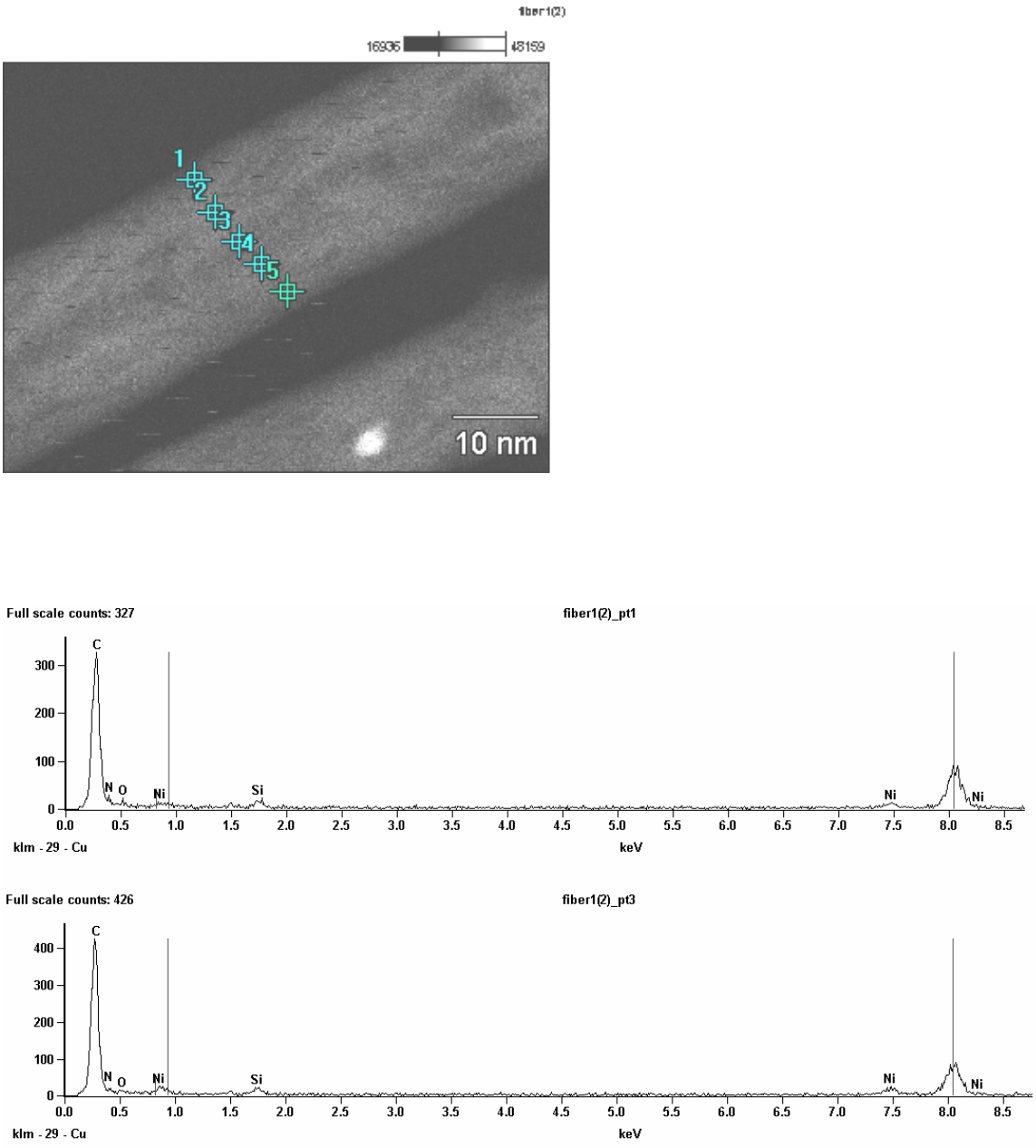

Fig. 4.9 EDX spectra for an individual dc VACNF from different points as indicated. Top image is a TEM image of the investigated VACNF. Top and bottom spectra were from point 1 and 3, respectively. Spectra from other points were similar to them.

Table 4.1 Composition of a dc VACNF (shown in Fig. 4.9) at five different points, as indicated by numbers.

	POINT 1		**POINT 2**		**POINT 3**		**POINT 4**		**POINT 5**	
	atom%	Wt.%	atom%	Wt.%	atom%	Wt.%	atom%	Wt.%	atom%	Wt.%
C	98.13	97.16	97.39	96.18	98.02	96.84	97.83	96.56	97.25	95.64
N	1.55	1.79	2.30	2.65	1.59	1.84	1.67	1.92	1.68	1.92
O	0.01	0.02	--	--	--	--	0.13	0.17	0.36	0.47
Si	0.19	0.44	0.13	0.30	0.21	0.48	0.17	0.40	0.60	1.37
Ni	0.12	0.59	0.18	0.87	0.17	0.84	0.20	0.95	0.13	0.60

and Ni were present, but in very small amounts. There was oxygen present in such a small amount that it can be neglected in most cases.

EDX line scanning across the fiber was also performed. Fig. 4.10 presents the elemental distribution result. To further clarify the locations of these elements, EDX mapping of Ni, Si and N was conducted. The results are demonstrated in Fig. 4.11. All the results confirm that Ni, Si and N were all incorporated in the fiber body.

O, N, Si and Ni may become incorporated into dc VACNFs through different mechanisms. The presence of a small amount of oxygen might result from the storage of sample in air after growth, since oxygen and water in air can be absorbed on the fiber. The incorporation of N is more complicated. N can either originate from the ammonia used in the growth process or nitrogen in air due to sample storage. Exact mechanisms of the incorporation of N during growth process are not completely understood at this moment. Implantation of atomic nitrogen, continuous absorption, and the attachment of nitrogen-containing carbon species onto the VACNFs are several possible mechanisms. In addition, the open edges of graphitic planes along the fiber length may make it easier for both N and O to be absorbed.

The presence of Ni along the whole VACNF length, though, is surprising. It has never been reported for VACNFs grown by dc PECVD. For a catalyst, it is thermodynamically impossible to expend it in an ideal chemical reaction. But as clearly shown by this work, Ni was not only observed in the fiber tips, but spread out along the whole fiber length. What concerns us is the mechanism by which Ni became incorporated

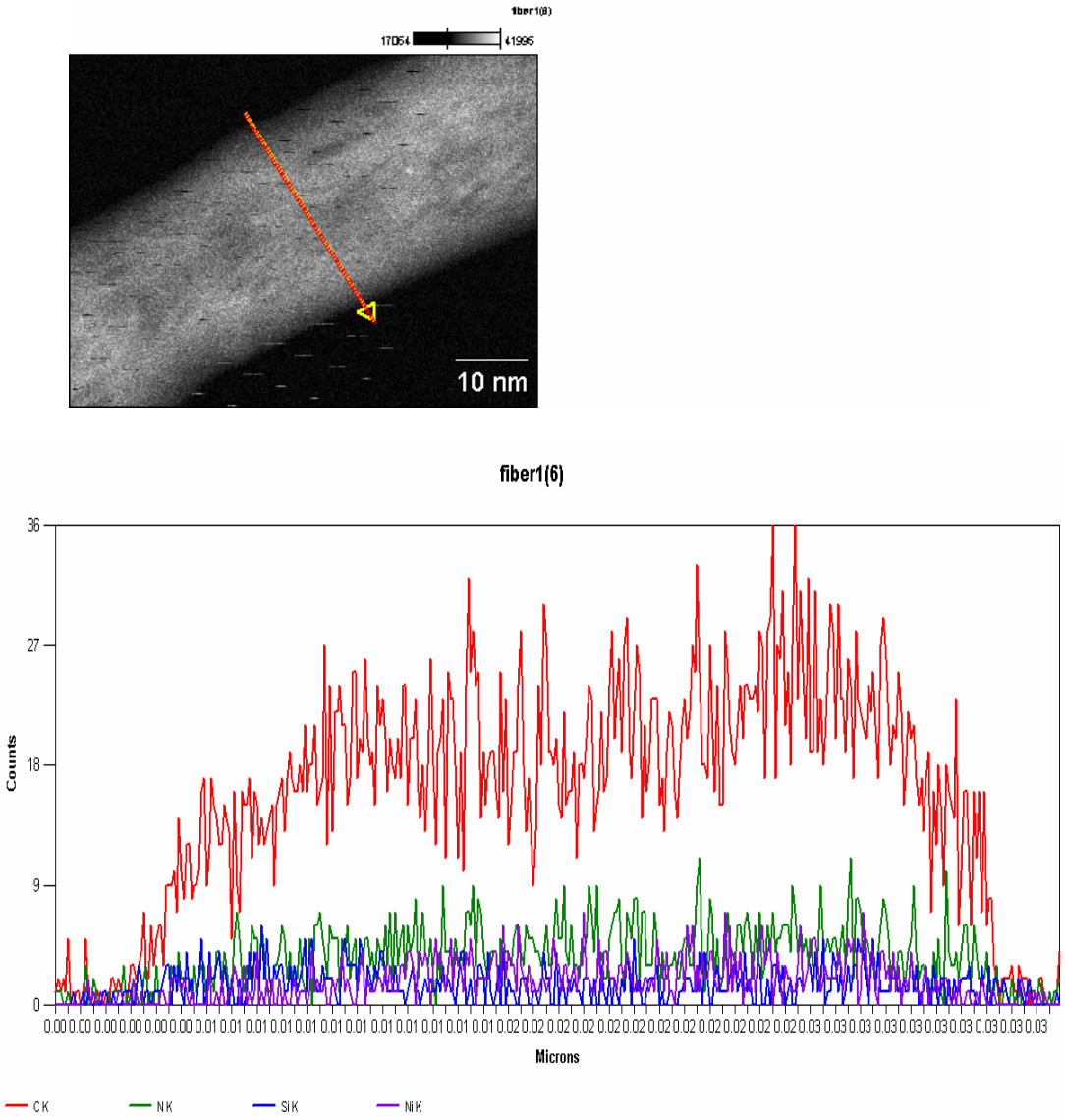

Fig. 4.10 Top image shows the dc VACNF studied for elemental distribution. Lower image presents the distribution of C (red), N (green), Si (blue) and Ni (purple) along the arrow direction in top image.

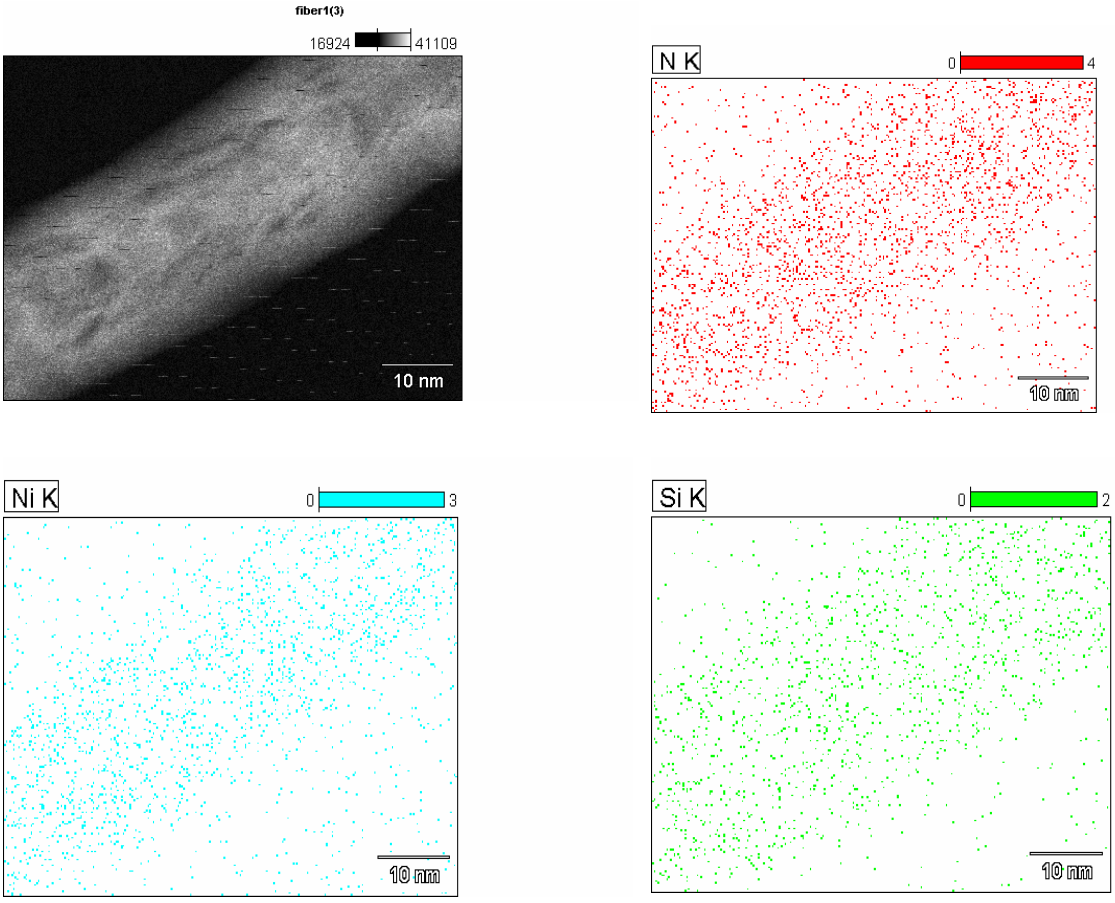

Fig. 4.11 EDX mapping of N, Ni and Si along a dc VACNF body.

into the fiber length. Another issue awaiting clarification is where Ni is located along the fiber: only in the outer layer, deeply embedded in the inner structures, or both.

To address the first concern, let us examine the source of Ni first. The sole source of Ni came from the 10 nm thick Ni film deposited on the growth substrate, which later broke into small discrete particles after pre-etching by ammonia at 375^{o}C. These Ni particles were later lifted off from the substrate and located at the fiber tips. During the whole process, Ni had two possible paths to get into the fiber body. One path is through the gaseous carrier as tiny particles, which was gradually sputtered off by energetic ion bombardment and might get charged in the plasma. This could take place at the first pre-etching step, in which some Ni might be set free into plasma as the whole Ni film is broken into small particles with plasma initiated. It was also observed by Merkulov and coworkers that some Ni was gradually sputtered off by ion bombardment after Ni took the tip position.[30] The sputtered-off Ni from probably both steps, carried by carbonaceous gas, precipitated with carbon at the outer walls of fibers during growth. This gave rise to Ni all along the fiber length, but mainly on the fiber surfaces, or the outer layer (region A in Fig. 4.4).

Another possible path of Ni getting into the fiber body may be through the Ni-C interaction at Ni fiber tips. It has been widely acknowledged that carbon precipitates out after it becomes supersaturated in Ni. In the presence of ammonia and acetylene, though, the precipitated carbon might not be pure carbon, but C with Ni and/or N, if provided with certain pressure and temperature. If this path with catalytic nature was effective, Ni would be observed in the center region of VACNFs (region B and C in Fig.4.4).

As two different paths of Ni would result in different locations of Ni in VACNFs, it is of great importance to determine how Ni is distributed laterally along these fibers. Unfortunately, EDX collects x-rays not only from the fiber surface but also fiber bulk, thereby offers little to solve this problem. To shed more light on this issue, AES was utilized, since it is very surface specific. Auger electrons fail to emerge with their characteristic energies if they start from deeper than about 5 to 10 nm into the surface.

Fig. 4.12 shows AES results for individual VACNFs. Fig. 4.12 (a) shows a typical line scan spectra from a VACNF undergoing a very short sputtering cycle (less than one minute). It can be seen that Ni was spread out in the fiber surface. After 4 minutes of sputtering, by sharp contrast, the Ni signal was very weak at most places, and only occasionally high at the fiber edge. These AES results indicate that Ni was primarily located in fiber walls, not in the center catalytic part. Therefore, it can be concluded that Ni became incorporated into the fiber body largely through the sputtered-off mechanism.

As for Si, the only source of Si was the substrate. During the growth process, the Si substrate was bombarded by ions, Si was sputtered off and carried into the growth atmosphere by gaseous phases, then precipitated at fiber outer walls. Since the VACNFs were crowded, not much Si surface was exposed. As a result, only small amount of Si became sputtered off and incorporated into fiber bodies. In the case of growth of segregated and discrete VACNFs, higher Si amounts have been observed, which is in agreement with our proposed mechanism.

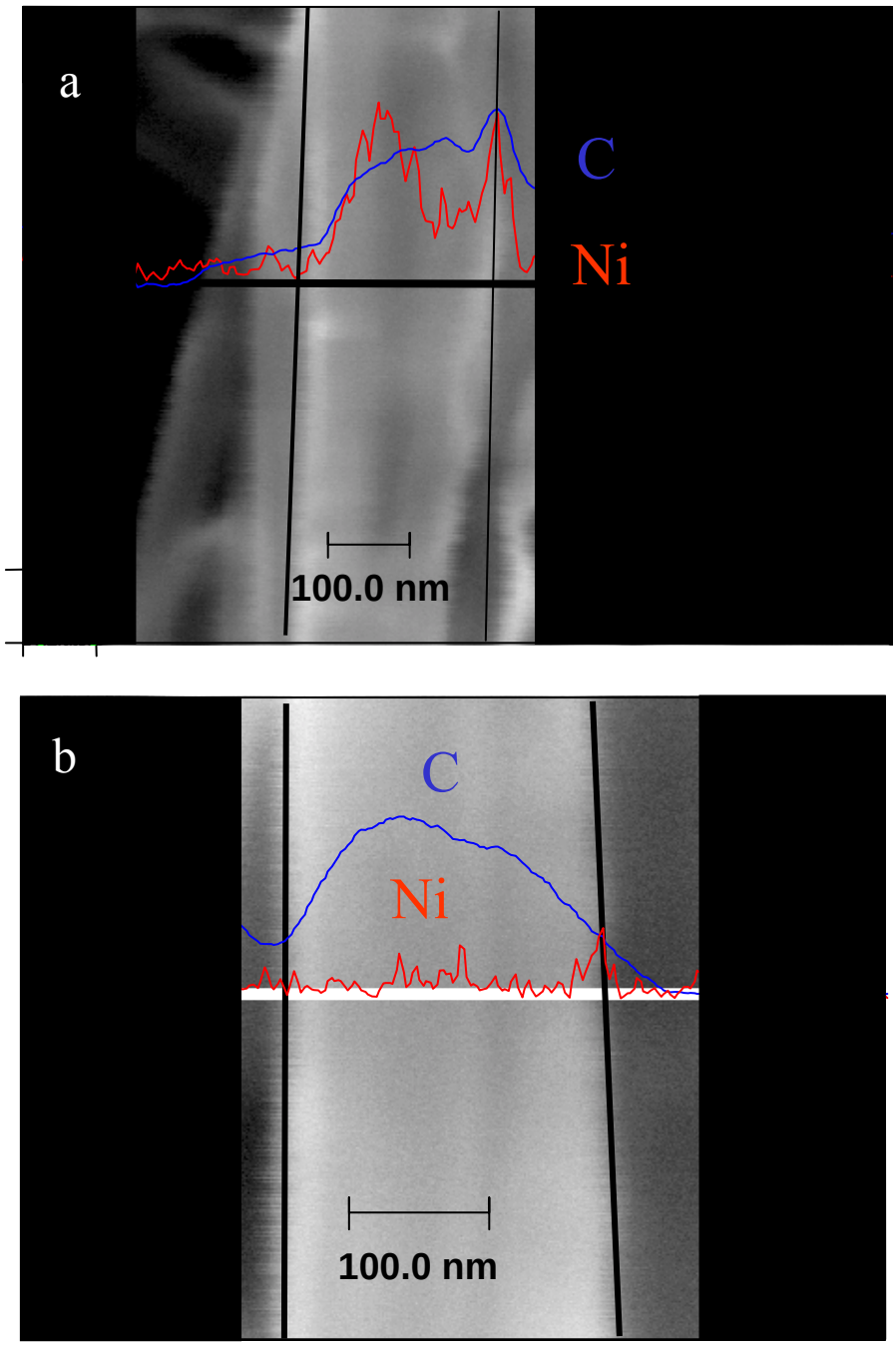

Fig. 4.12 Auger linescan for C (blue) and Ni (red) across (a) a dc nanofiber sputtered for less than one minute and (b) a nanofiber sputtered for 4 minutes. Vertical black lines show the edges of nanofibers. A mask was placed over the sides of the image to highlight the nanofiber of interest.

Chapter 5 Intrinsic charge transport properties of dc VACNFs

To carry out intrinsic charge transport properties of dc VACNFs, it is essential to obtain low-resistance ohmic contacts between VACNFs and metal electrodes. The first part of this chapter, therefore, describes the technique used in this work to define ohmic contacts between dc VACNFs and various metal electrodes. Four-probe charge transport results are presented in the second part of this chapter. The manner in which the outer layer of dc VACNFs determines the metallic charge transport properties of these fibers is discussed as well.

5.1 Define ohmic contacts between dc VACNFs and various metals

5.1.1 Overview of various techniques to define ohmic contacts on carbon nanotubes

Low-resistance ohmic contacts between carbon nanostructures and metal electrodes are highly desirable for successive charge transport measurements and future electronic applications of these nanostructures. For carbon nanotubes, much research has been conducted in this area, and ohmic contacts have been achieved in different ways.

Contact between a carbon nanotube and metal can be fabricated in two ways. One is the so-called "metal-on-tube" approach, which usually involves e-beam lithography, focused ion beam or a shadow mask to expose segments of a carbon nanotube, followed by metal deposition to form metal electrodes on top of these uncovered segments. The other is a "tube-on-metal" approach, in which carbon nanotubes are randomly placed on predefined metal electrodes so that the contact occurs at the circumference of the tube wall.

For the "metal-on-tube" scheme, it has been reported that reliable and robust low-resistance contacts were made by positioning a W wire on top of a MWCNT as a shadow mask, followed by Ti/Au deposition. In this case, CNTs experienced the least chemical handling, thereby offering a clean surface for contacts[46]. J.O. Lee and coworkers used e-beam lithography and achieved stable low-resistance ohmic contacts between MWCNT and Ti/Au by a rapid thermal annealing method at 600-800^{o}C for 30 seconds. They proposed that the formation of such contacts was attributed to the formation of Ti-carbides at the interface of the CNT and Ti/Au interface.[47] Pd and Ti contacts on metallic SWCNTs were found to be ohmic after annealing at 220^{o}C in Ar for 10 minutes, as reported by Dai and coworkers.[48]

For the "tube-on-metal" approach, several ways of achieving low-resistance ohmic contacts have been reported. Zhang and coworkers fabricated low-resistance ohmic contacts between Ti and SWCNTs by a high temperature annealing ($800^{o}C \leq T \leq 1000^{o}C$) for 20 minutes. It was found that the low-resistance contacts originated from the formation of TiC at the interface, which is a good conductor at room temperature.[49]. Batchtold *et al.* achieved low-resistance ohmic contacts between Au and MWCNTs by selectively exposing the contact areas to the electron beam in a SEM,[50] although the exact mechanism of the formation of ohmic contacts remained unclear.

For all the method mentioned above, the low-resistance ohmic contacts were achieved at the expense of additional chemical/mechanical/thermal treatment of CNTs, which might exert considerable effect on their intrinsic charge transport properties .

5.1.2 Define ohmic contacts between dc VACNFs and metal eletrodes

In this work, defining low-resistance ohmic contacts is especially challenging due to the presence of thick PMMA (~ 800 nm) spin coated on top of dc VACNFs. Usually, the best e-beam lithography results are achieved when the width of patterned electrodes is no less than the thickness of resist. In this case, however, it is not realistic to pattern several such wide electrodes on a VACNF with a limited length (~ 4-5 um). Instead, we defined narrower Ti/Au electrodes (200- 400 nm) to put as many electrodes as possible on the fiber in order to assure successful four-probe charge transport measurements. This may cause a multitude of problems. One major problem is that some resist residue may be left at the VACNF sidewall surface, leading to errors in the subsequent electrical measurements. This problem may be exacerbated for PECVD grown VACNFs, whose structures are highly defective, leading to high reactivity at the outer surfaces. In this study, prior to metal deposition, we used O_2 plasma reactive ion etch (RIE) (O_2 flow rate of 50 sccm, power 95 W, 12 seconds) to remove this residue, allowing the formation of ohmic contacts with low contact resistance between the VACNF and Ti/Au metal electrodes. The typical resistance of contacts defined by this method ranged from 0.2 kΩ to several kΩ. This method is reliable and easy to apply, and has never been reported before by other research groups.

Fig. 5.1 demonstrates AFM images of a patterned electrode before and after exposure to O_2 plasma. It is evident that O_2 plasma effectively removed PMMA residue on this VACNF and on the side walls of electrodes, producing a clean open area for subsequent metal deposition.

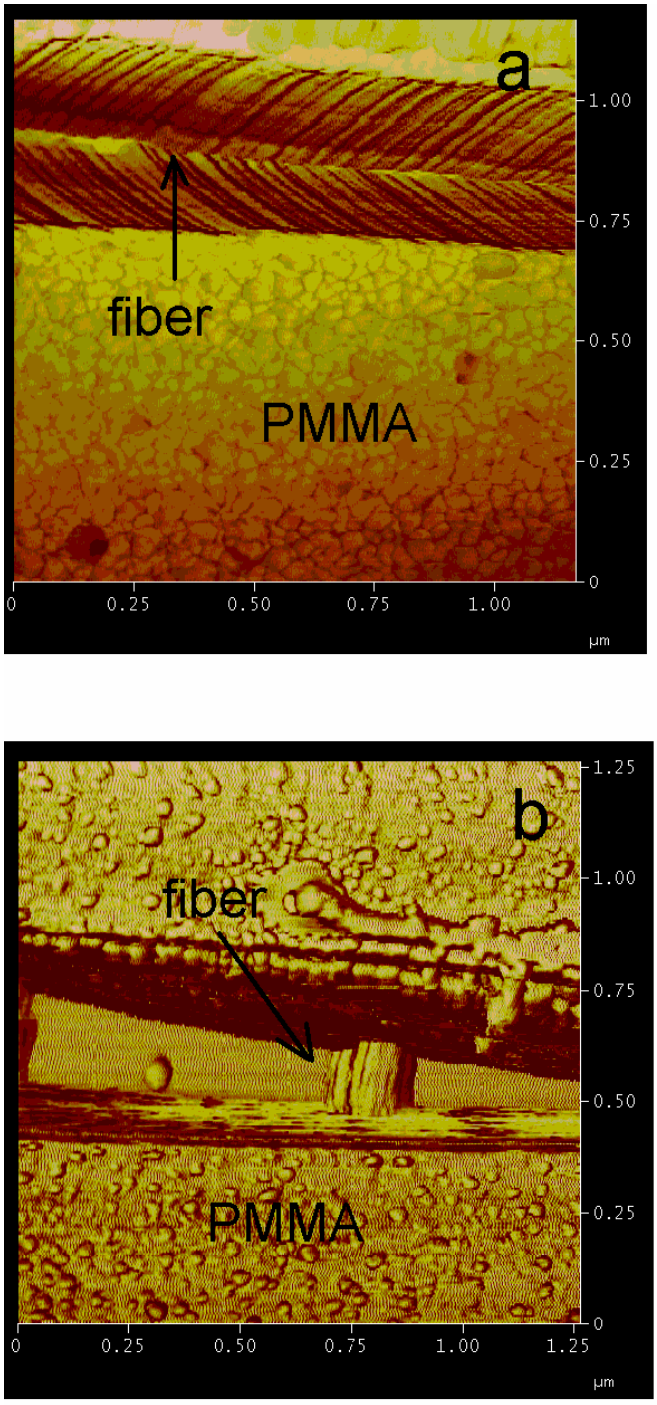

Fig. 5.1 AFM images of a patterned electrode (a) before and (b) after 12 seconds of RIE.

Without the RIE treatment, a two-probe dc VACNF device with 200 – 400 nm wide electrodes (Fig. 5.2 (a)) typically exhibited non-linear I-V behavior, and the contact resistance can be up to several mega-ohms (Fig. 5.2 (b)). Such a device carried very low current. The I-V curves were usually not repeatable as well. By sharp contrast, after RIE with optimized time, I-V curves of these devices were linear and invariably reproducible (Fig. 5.2 (c)). The contact resistance can be reduced by a magnitude of 1000 to several kilo-ohms compared to the case without RIE. For this device, it carried current as high as 0.5 mA, which corresponded to a current density of 3.5×10^{10} A/m^2. Excessive RIE, though, led to non-linear I-V behavior again (solid-triangle line in Fig. 5.2 (b)). The effect of excessive O_2 plasma etching on the nanofiber structure will be addressed in section 5.2.

An optimized etching time is key to this O_2 plasma etching process. To determine the premium RIE time, the sample was put into RIE chamber for a few seconds of etching. AFM imaging was performed afterwards. If the fiber segment could not be seen, more RIE time was required until all the fiber segments in the pattern were clearly visible. AFM is an ideal tool for this task, since the imaging is non-destructive and reveals many submicron details. Fig. 5.3 demonstrates a patterned dc VACNF ready for metal deposition.

The optimized etching time was different for different widths of patterned electrodes, as observed in this work. A wider electrode usually needs shorter RIE time. Preferably, all electrodes should have identical widths so that the optimized etching time is the same for all of them, otherwise some VACNF/metal electrode contacts are ohmic and some are not in the same device. Fig. 5.4 presents a VACNF device with six contacts, which was

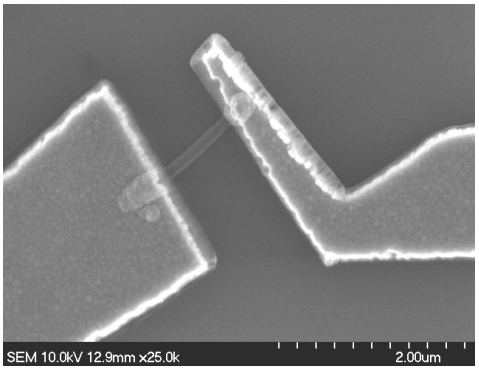

(a)

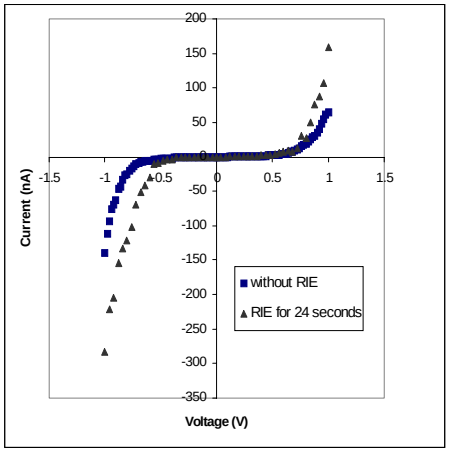

(b)

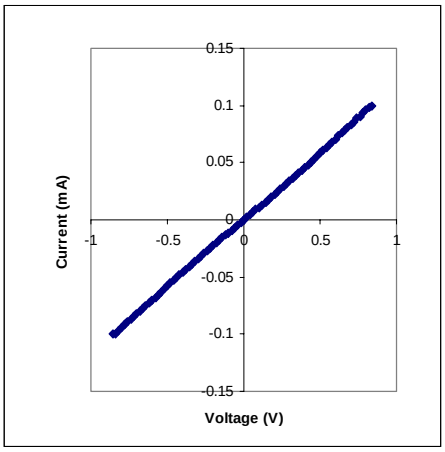

(c)

Fig. 5.2 (a) A SEM image of a two-probe dc VACNF structure. (b) Typical I-V curves for two-probe VACNF structures experiencing no RIE (solid square) and excessive RIE (24 seconds) (solid triangle). (c) I-V curve of a two-probe dc VACNF structure subjected to RIE with optimized time (12 seconds). The resistance of the structure was 6.6 KΩ.

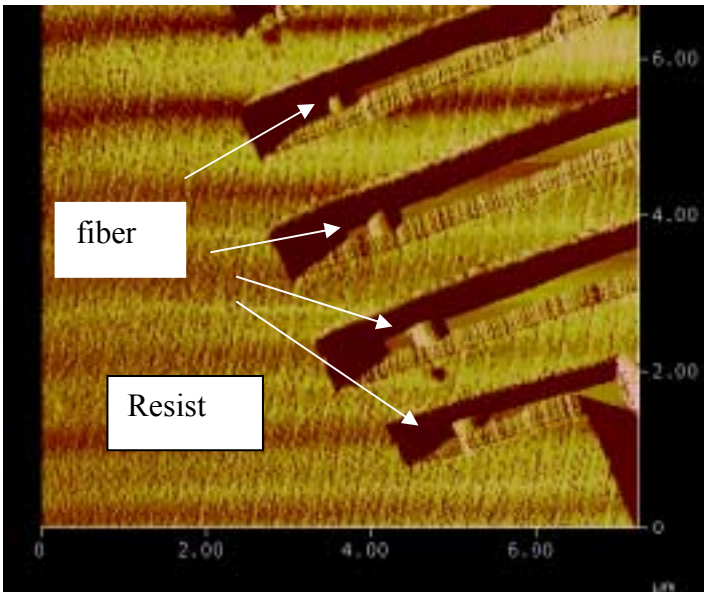

Fig. 5.3 An AFM image of a patterned dc VACNF ready for metal deposition. All the fiber segments are clearly visible.

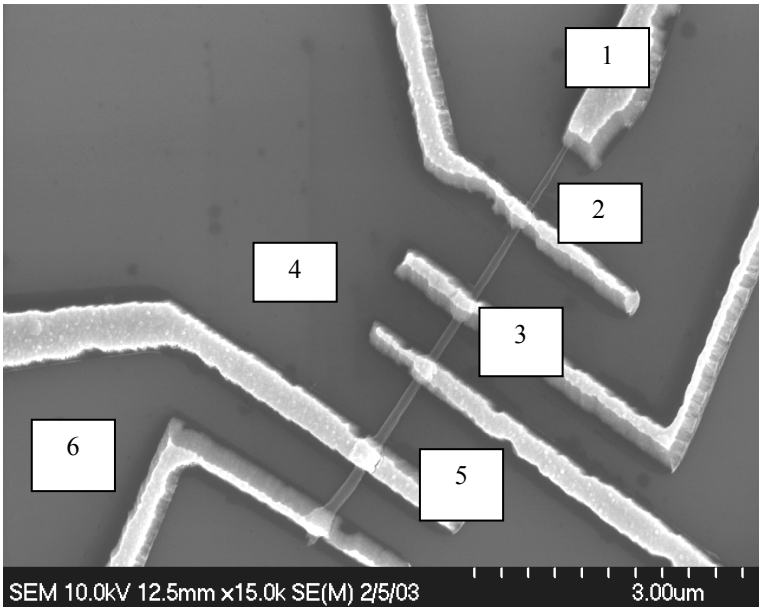

(a)

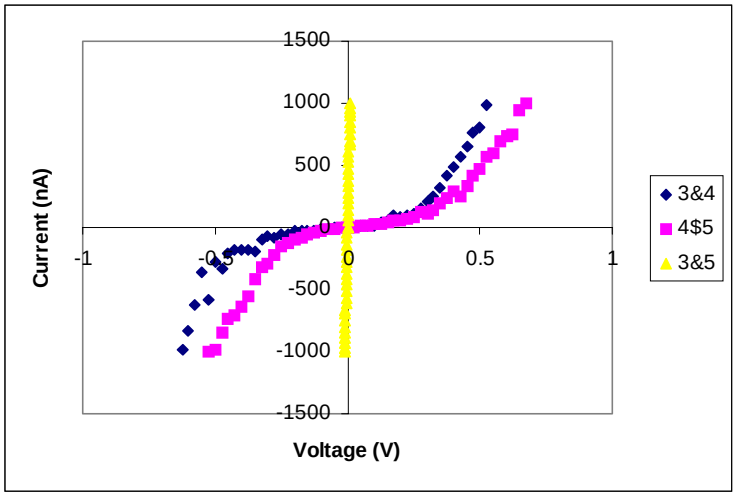

(b)

Fig.5.4 (a) A SEM image of an individual dc VACNF with 6 electrodes, which underwent 11 seconds of RIE. (b) I-V curves measured between 3&4, 4&5, and 3&5 in (a).

subjected to 11 seconds of RIE. I-V curves measured between contacts 3 & 4 and contacts 4 & 5 were non-linear, indicating very high resistance of the two-probe structures (contact 3-VACNF segment-contact 4, and contact 4-VACNF segment-contact 5). By sharp contrast, the I-V curve measured between contacts 3 & 5 was perfectly linear, indicating that contacts 3 and contact 5 were ohmic, but contact 4 was not. The occurrence of such mixed contacts may be attributed to the smaller width of electrode 4, since apparently11 seconds of RIE did not sufficiently remove the PMMA residue on this contact. Still, more work needs to be done to determine strict electrode width versus optimized RIE time relationship.

5.1.3 Various dc VACNF/metal contacts

Through the O_2 plasma etch method, ohmic contacts between dc VACNFs and Ag/Au, Cd/Au, and Cr/Au electrodes were achieved in addition to Ti/Au electrodes. Linear I-V curves were observed for all these metal electrodes. Fig. 5.5 demonstrates a patterned dc VACNF with Cd/Au electrodes, and correspondent I-V curve from electrodes 1 and 2. The resistance of this structure (electrodes 1 and 2, dc VACNF segment in between) was 1.4 kΩ. I-V curves measured from all other possible combinations of two electrodes were all linear, which indicates that all contacts on the patterned CNF in Fig. 5.5 were ohmic. Magnesium is an exception, though. All the samples patterned (3 samples, 14 electrodes) with Mg/Au electrodes exhibited non-linear behaviors, with current in the order of fA. This high contact resistance may be due to the formation of MgO at the fiber/Mg interface, since Mg is prone to oxidation even in air. The adhesion between Mg and Au was not very good either, as can be observed in Fig. 5.6.

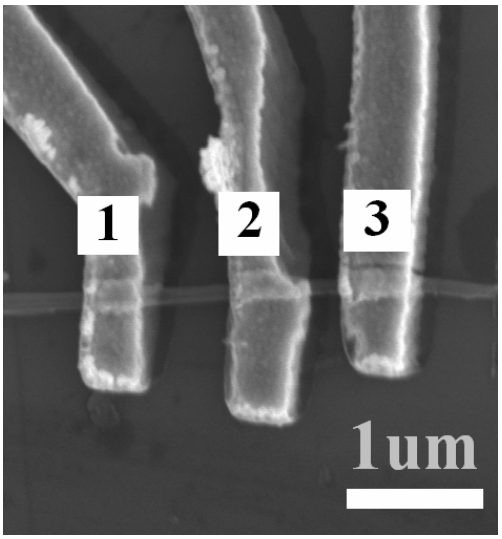

(a)

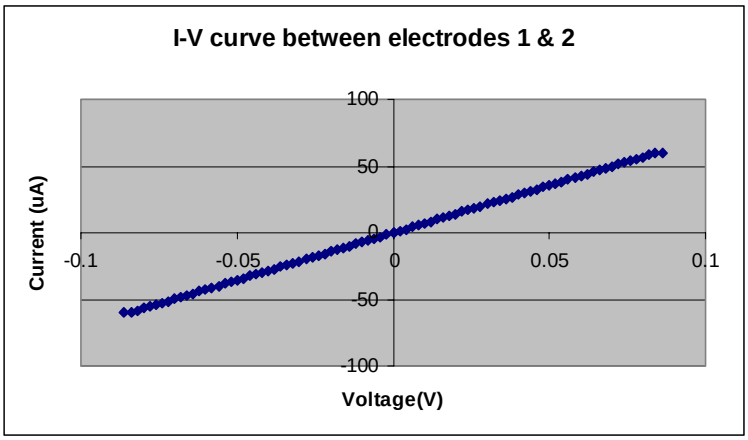

(b)

Fig. 5.5 (a) A patterned dc VACNF with Cd/Au (200 nm each) electrodes. (b) I-V curve measured between electrodes 1 & 2 in (a). I-V curves measured between two electrodes in all possible combinations were all linear.

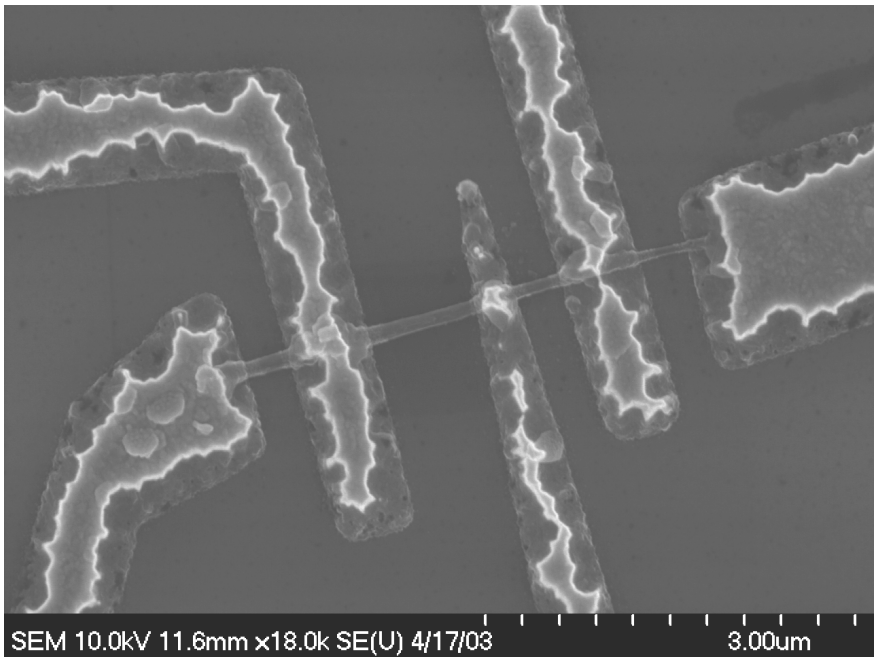

Fig. 5.6 A patterned dc VACNF with Mg/Au electrodes.

These facts eliminate the possibility of using Mg as a contact metal for dc VACNFs.

To choose a suitable metal for electrodes, several factors need to be considered in addition to the ohmic behavior of contacts, although this remains the most important issue. The chosen metal has to be compatible with SiO_2 to assure good adhesion. It also needs to bond very well with Au to achieve a flat surface on the measuring pads. Among all the metal electrodes tested in this work, by far, Ti/Au is the best candidate for contacts on dc VACNFs in terms of Ti/dc VACNF ohmic contact quality, compatibility with SiO_2 and Ti/Au adhesion.

5.2 Four probe charge transport measurements of dc VACNFs

5.2.1 I-V characteristics of dc VACNFs

After successfully fabricating ohmic contacts with low contact resistance, four-probe charge transport measurements were carried out. Fig. 5.7 presents a SEM image of a completed dc VACNF structure with five metal electrodes (200 nm each of Ti/Au) contacting the nanofiber. The VACNFs exhibited linear I-V behavior, as shown in Fig. 5.8. Two probe measurements on substrates without a nanofiber showed a leakage current in the pA range, and therefore had negligible effect on the transport measurements. The resistance of the segment of fiber between contacts 2 and 3 was 2.7 kΩ. The diameter and length of this fiber segment were approximately 135.5 nm and 0.880 μm, giving a fiber resistivity of 4.4×10^{-3} Ω·cm ($\rho = R \times S/L$). A two-probe I-V curve of this nanofiber segment is also included in Fig. 5.8, from which the contact resistance of 1.3 kΩ was

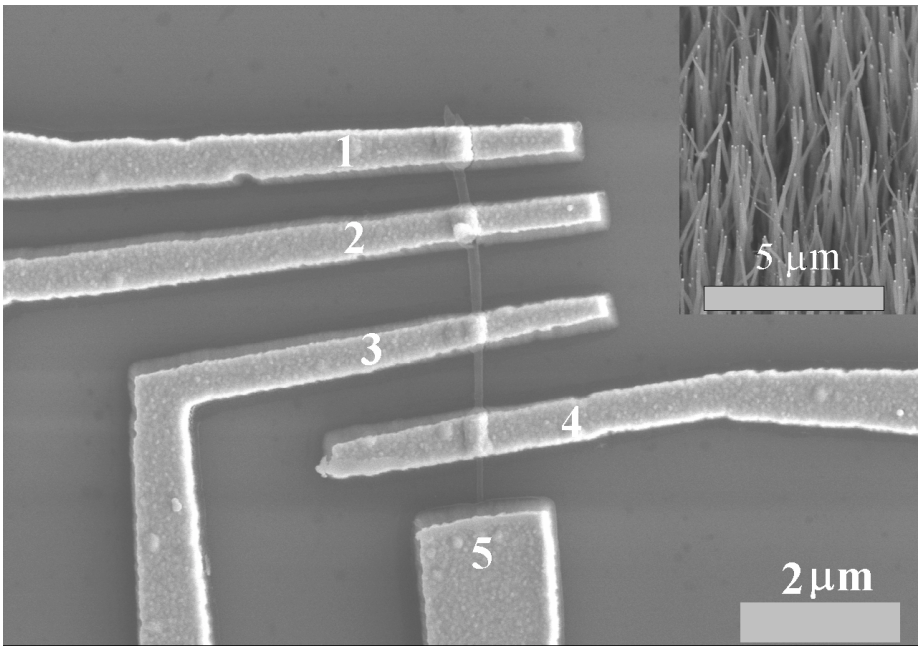

Fig. 5.7 SEM image of a completed dc VACNF structure with 5 metal electrodes (200 nm each of Ti/Au) contacting the nanofiber. Inset is a SEM image of the as-grown VACNF forest.

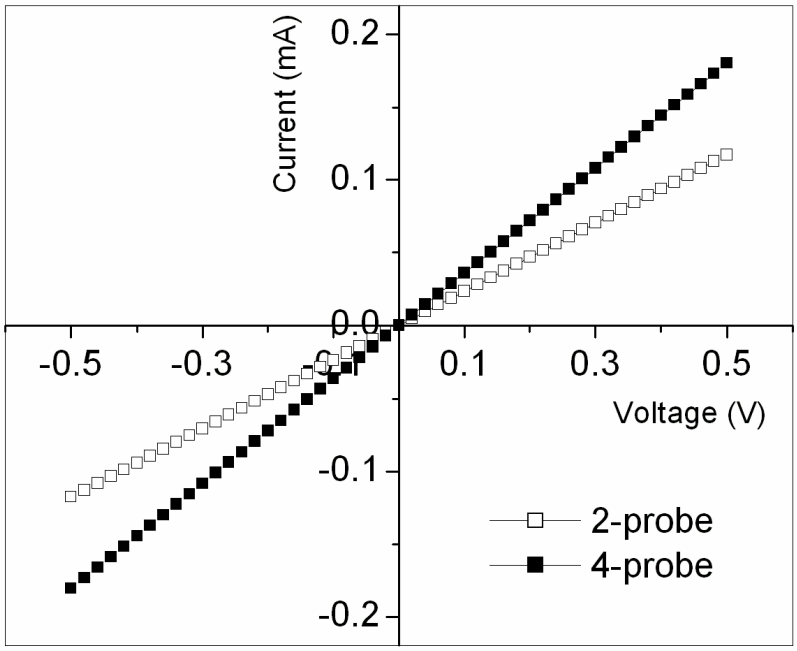

Fig. 5.8 I-V curves for the 4-probe (electrodes 1, 2, 3 and 4 of the device in Fig. 5.7) and 2-probe (electrodes 2 and 3) measurements.

found. Measurements on 11 different fibers yielded similar results, with resistivity ranging from 3.2 x10^{-3} Ω·cm to 4.6 x10^{-3} Ω·cm (Fig. 5.9), and all the I-V curves (both 2-probe and 4-probe measured) were linear. The I-V behaviors of the devices were carefully checked for gate effects using the heavily doped Si chip as a back gate. No gate effects were seen for gate voltages between –5 and 5 volts, consistent with metallic VACNFs behavior.

5.2.2 Charge transport model of dc VACNFs

The observation that the average VACNF resistivity (4.2x10^{-3} Ω·cm) lies in between that of graphite parallel to the basal plane (4x10^{-5} Ω·cm) and perpendicular to the basal plane (4x10^{-2} Ω·cm) is consistent with a simple model of charge transport where electrons travel mainly from one graphitic plane to another along the length of the nanofiber. It is well known that VACNFs are composed of graphitic "funnels" and cones, in what is known as a "herringbone" and "bamboo-like" structure surrounded by an outer layer, as shown in chapter 4. Fig. 5.10 (a) shows a schematic representation of such a structure. Applying a graphitic plane charge transport model to such a structure and taking the graphitic planes as the basal planes of graphite, resistivity is given by[2]

$$\rho(\theta) = \rho_a \sin^2\theta + \rho_c \cos^2\theta, \qquad (5.1)$$

where θ is the angle of current flow to the axis perpendicular to the basal plane of graphite (Fig. 5.10 (a)), ρ_a is the resistivity parallel to the basal plane, and ρ_c is the resistivity perpendicular to the basal plane.

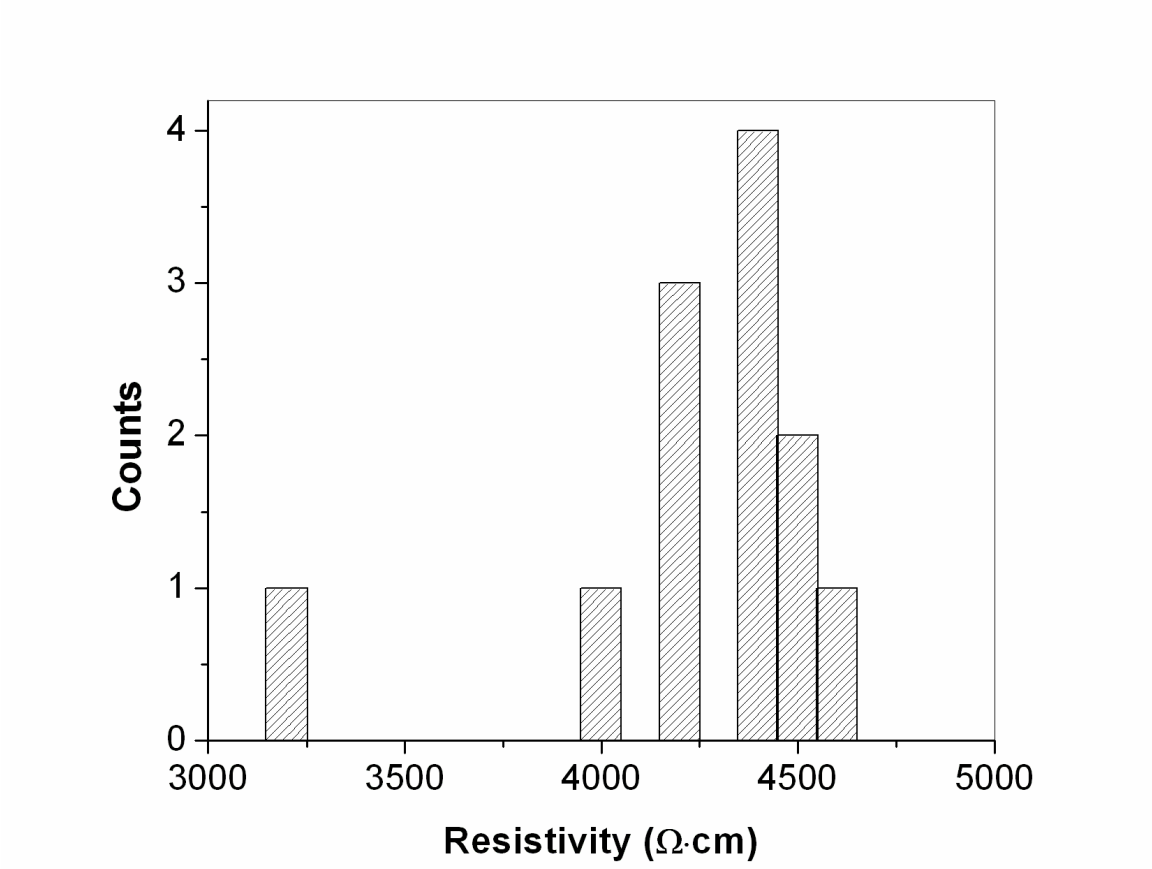

Fig. 5.9 Histogram of the 4-probe measured resistivity of 12 VACNFs. The resistivity ranged from 3.2×10^{-3} Ω·cm to 4.7×10^{-3} Ω·cm. The average resistivity was 4.2×10^{-3} Ω·cm.

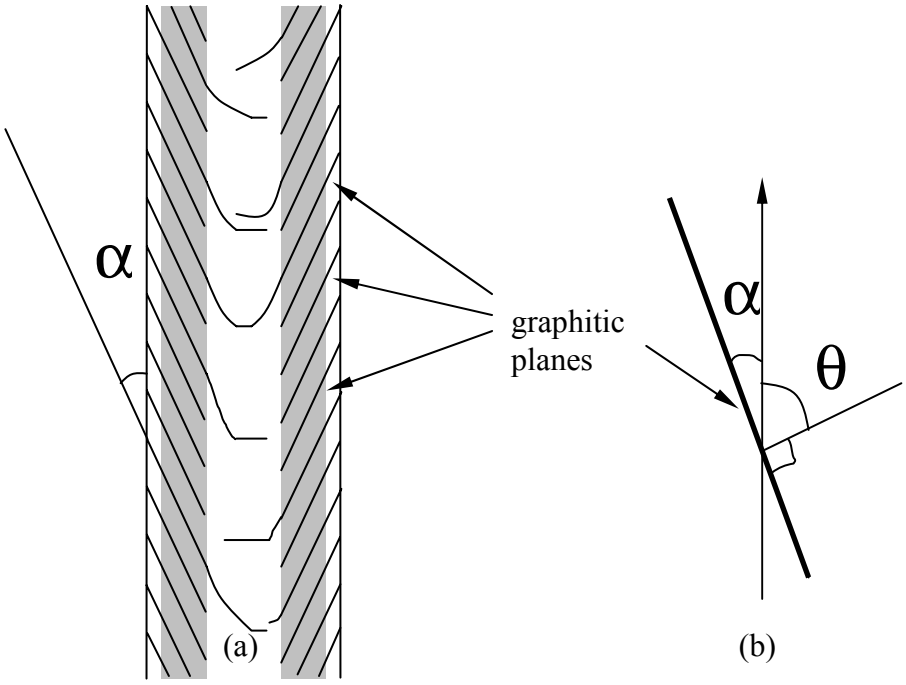

Fig. 5.10 (a) A schematic representation of VACNF structure where α is the angle between the graphitic planes and the axis along fiber length. (b) The relationship between α and θ with $\theta = 90^{o}-\alpha$.

α was shown in Fig. 4.2 (c) and (d) to be about 20^o , giving a θ of approximately 70^o. For the values of ρ_a and ρ_c given above, equation (1) yields $\rho = 4.7x10^{-3}$ Ω·cm for the nanofibers used here, in good agreement with our experimental measurements.

5.3 Outer layer-determined charge transport properties of dc VACNFs

In the last section, it has been demonstrated that dc VACNFs are metallic, and the resistivity has been calculated. Still, it remains unclear which substructures of the dc VACNFs control the charge transport properties. Here in this section we report that the graphitic outer layer of VACNFs determines the intrinsic metallic charge transport properties of the fibers as demonstrated by the measurement of transport before and after removal of this 12-15 nanometers thick layer with an O_2 plasma etch. Before this treatment, the dc VACNFs exhibit a linear I-V characteristic, while after the etch, fibers exhibit non-linear I-V behavior. Our study demonstrates that this outer layer governs the metallic charge transport in dc VACNFs, and also suggests that by varying the extent of graphitization and structure of this layer, it is possible to achieve controllable charge transport properties for dc VACNFs.

5.3.1 I-V characteristics of dc VACNFs before and after RIE

Fig. 5.11 shows a SEM image of a completed VACNF structure with 4 electrodes. To investigate the changes in the intrinsic charge transport properties of the fibers, four-probe measurements were performed in air at room temperature using an HP precision semiconductor parameter analyzer (4156A) before and after each etch. Two successive 5-sec. O_2 plasma reactive ion etch (RIE) steps (O_2 flow rate of 50 sccm, power 95 Watts)

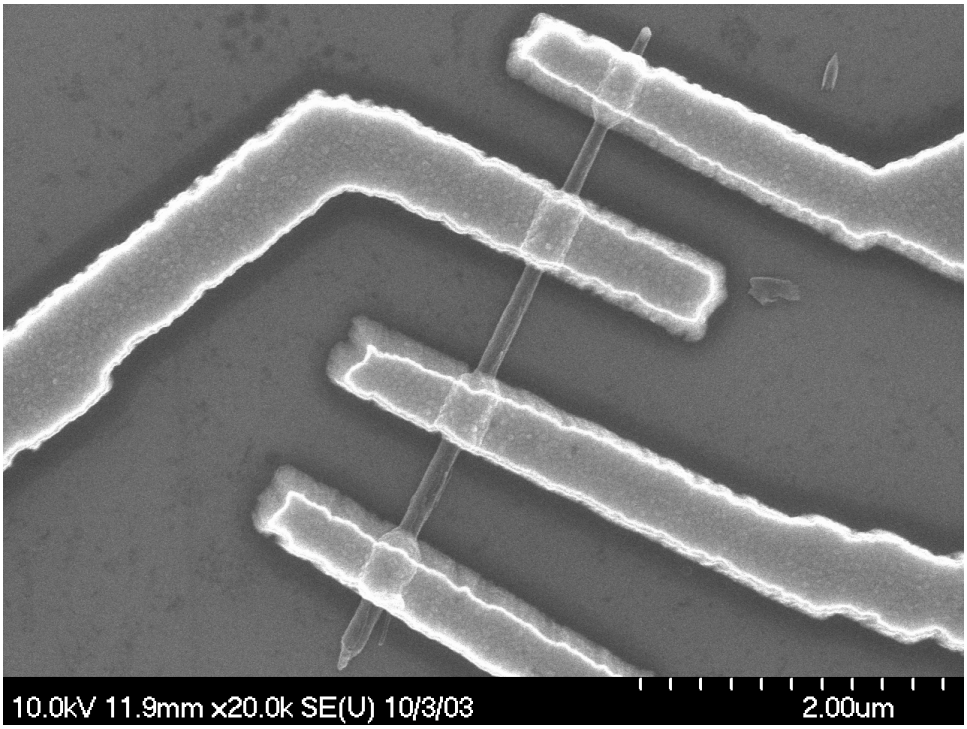

Fig. 5.11 A patterned dc VACNF with four electrodes (200 nm Ti/Au).

were performed on the nanofibers. Fig. 5.12 shows typical I-V curves taken before and after each etch step. The fiber exhibited linear metallic I-V behavior before RIE, as we previously reported[8]. After the first 5 seconds of RIE, there was little or no change in the I-V characteristic. However, after the second RIE step (total RIE time = 10 sec.), the fiber exhibited linear behavior for the first voltage sweep, but thereafter displayed rectifying behavior, with the current magnitude dramatically decreasing for each subsequent voltage sweep. After several voltage sweeps the fiber was irreversibly damaged. Similar I-V behavior has been observed repeatedly on other fibers from the same forests subjected to the same etch processing. Unfortunately, as the I-V curves differed for each voltage sweep, it was not possible to test modulation of the nanofiber current using the heavily doped Si chip as a back gate.

5.3.2 Structure difference of dc VACNFs before and after RIE

The results above suggest that regions of the nanofibers important to charge transport were being modified by the RIE processing, and we used HRTEM to determine the structure of individual fibers before and after the etch steps. VACNFs from the same forest were removed from the growth substrate and placed onto 3 TEM grids. One grid received no RIE processing; the other two grids were subjected to 5 and 10 seconds of RIE respectively. Fig. 5.13 demonstrates how the typical structures of the VACNFs changed before and after RIE. Note that all the images were taken at the fiber segment with a diameter of ~ 120 nm, which was the same as that of the fiber segment used in the four-probe charge transport measurements.

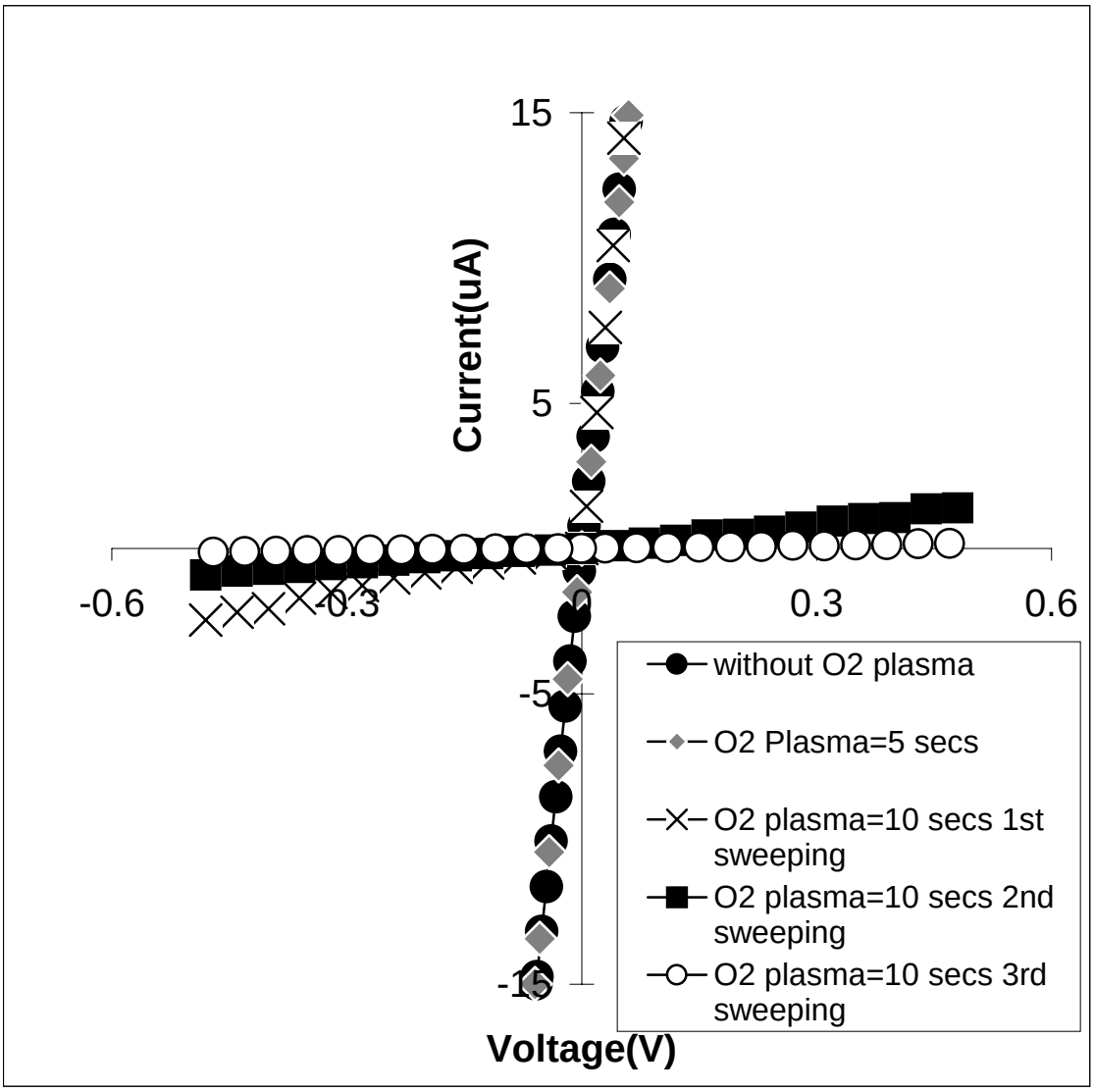

Fig. 5.12 I-V curves for the four-probe measurements on the fiber in Fig. 5.11 before and after O_2 plasma reactive ion etch.

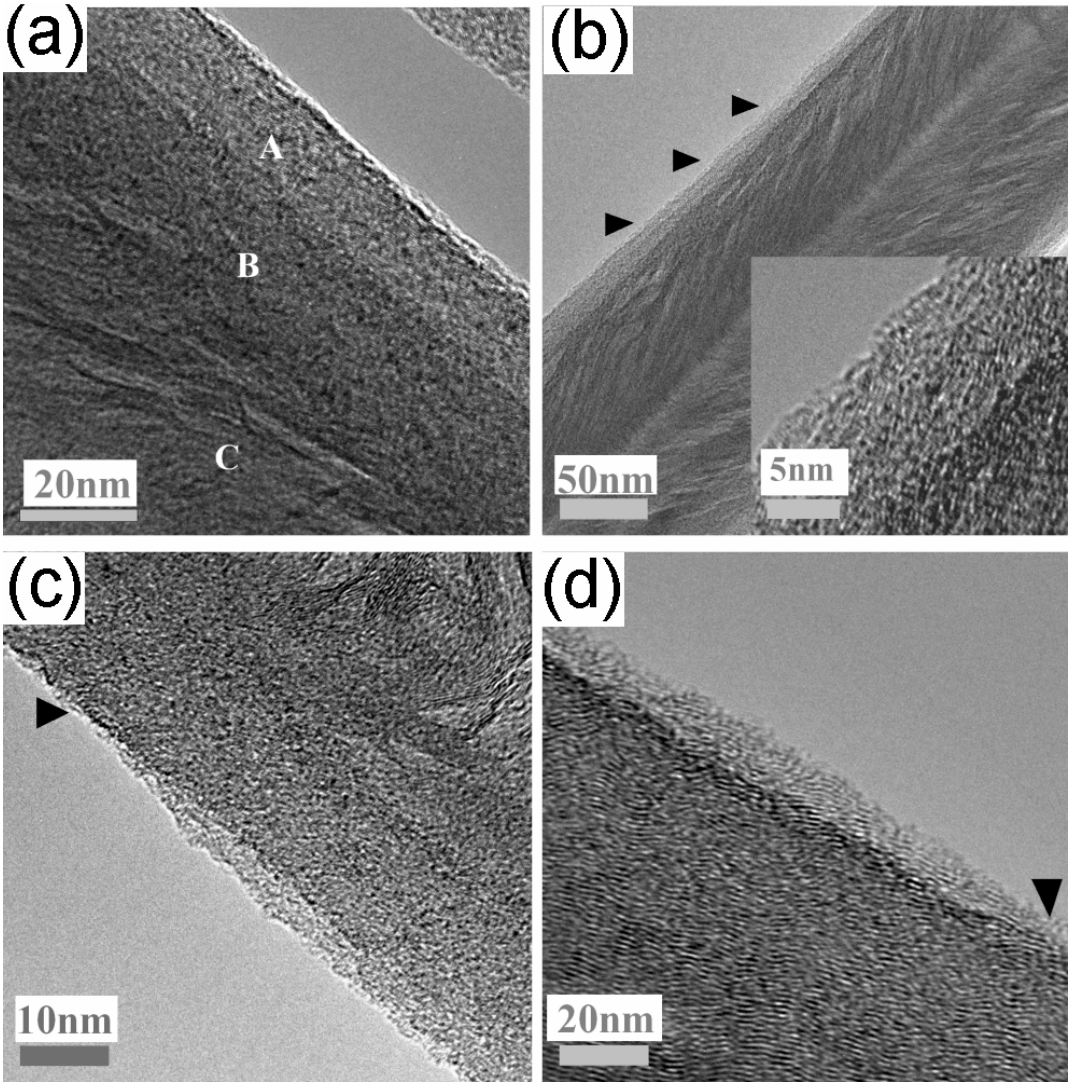

Fig. 5.13 (a) TEM image of a dc VACNF segment with a diameter of ~120 nm. Region A: graphitic outer layer; region B: the layer with darker contrast; region C: central "cross-struts". (b) TEM image of a VACNF segment subjected to 5 seconds of O_2 plasma. This fiber segment had a diameter of ~120 nm. The arrows indicate the outer layer, which thickened along the fiber length. Inset shows a HRTEM image of the outer layer of this fiber. (c)-(d) TEM images of VACNF exposed to 10 seconds of RIE. Arrows indicate where the outer layer is completely (c) and partially (d) stripped off.

For fibers not seeing any O_2 plasma, details of the structure can be refered to in Fig. 4.2. VACNFs with the structure described above uniformly exhibited metallic I-V behavior.

After the fibers were exposed to 5 seconds of O_2 plasma, the graphitic outer layer was partially stripped away, but still covered the entire length of the fiber (Fig. 5.13 (b)). However, close to the tip region, the remaining semi-graphitic layer was thinner, becoming gradually thicker along the fiber length. Such a structure is illustrated schematically in Fig. 5.14 (b). It appeared that O_2 plasma was more aggressive to the outer layer of the thinner part of the fibers than of the thicker part, which may imply compositional or other differences within the outer layer along the fiber length. The fibers still offered linear I-V curves after this period of etching.

The second 5-second O_2 plasma exposure left the fiber only partially covered by the semi-graphitic layer, leaving the inner layers (darker contrast) exposed at various parts of the fiber (Fig. 5.13 (c) and (d)). The outer graphitic structure was still present on some portions of the fiber, forming a net-like outer skin, as illustrated in Fig. 5.14 (c). The fact that only some portion of the semi-graphitic layers was removed might be due to the highly defective nature of this layer. The dramatic difference in the I-V characteristics for these fibers would seem to be correlated with the structural modification of this outer graphitic layer, indicating that the graphitic outer layer governed the intrinsic metallic behavior of the VACNFs.

The metallic behavior of the graphitic outer layer is similar to that of graphite with Bernal structure, rhombohedral graphite and simple hexagonal graphite, in the sense that they are all dominated by the two-dimensional in-plane interactions. The rectifying

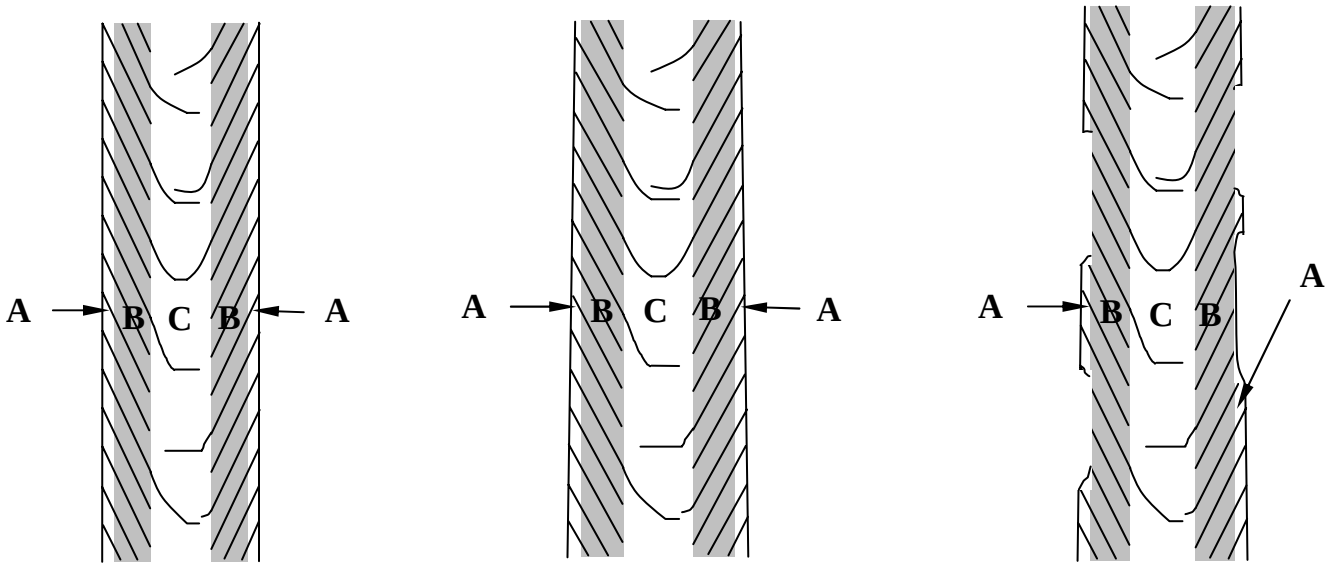

Fig. 5.14 (a)-(c): Schematic representations of dc VACNF structure with 0, 5 and 10 seconds of exposure to O_2 plasma etch respectively. Region A: graphitic outer layer; region B: the layer with darker contrast; region C: central "cross-struts".

behavior of the fiber after removal of the graphitic outer layer is an intriguing result. Perhaps it can be attributed to the possible compositional difference in layers A and B (refer to Fig. 5.13(a)).

5.4 Temperature dependence of dc VACNF resistivity

Four-probe temperature dependence of resistivity was measured for dc VACNFs. The resistance versus temperature curve is shown in Fig. 5.15. There is no apparent increasing or decreasing trend for resistance for the temperature range from 200 to 300 K. Overall, the resistance does not vary appreciably as the temperature changes. This indicates that thermal activation does not play a dominant role in this temperature range; otherwise, a decreasing resistance would have been observed as temperature increased. The high-density defects in the dc VACNFs could account for the observed temperature-independent behavior. Electrons scatter on these defects so intensely that the mean free path of electrons does not change much as temperature changes. In addition, the hopping of electrons between graphitic planes may also not be considerably affected by temperature.

Three-contact resistance, which includes the contribution from both the resistance of the nanofiber itself and that from one contact, decreased as temperature increased, as shown in Fig. 5.16. Since the resistance of dc VACNF itself shows little change over the temperature range, it is apparent that the contact resistance decreases as temperature increases. It is possible that elevated temperature helps electrons transfer between the metal and dc VACNFs.

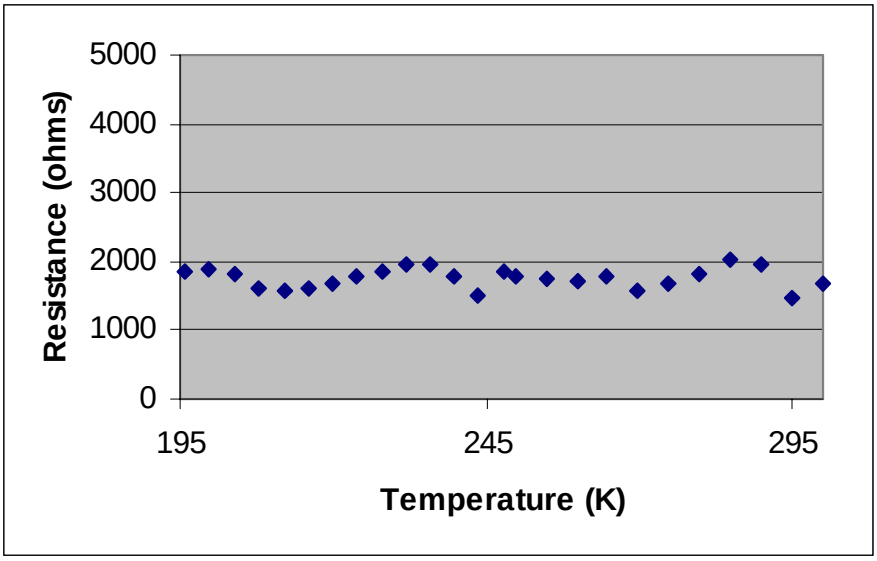

Fig. 5.15 Temperature dependence of the four-probe resistance.

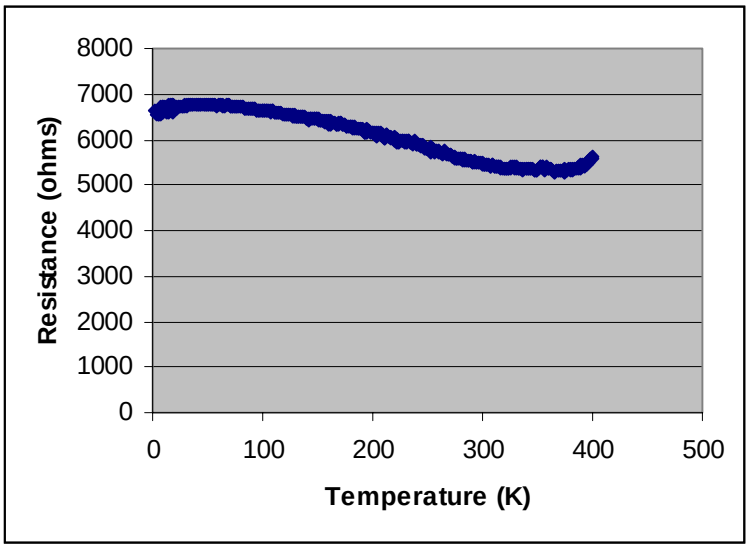

Fig. 5.16 Temperature dependence of the three-contact resistance.

Chapter 6 Inductively coupled PECVD VACNFs

VACNFs grown by inductively coupled PECVD (ICP VACNFs) represent an important group of aligned carbon nanofibers. In this work, ICP VACNFs grown at normal pressure (3.6 Torr) and very low pressure (50 mTorr) have been studied in terms of structure, composition, and charge transport properties. C_2H_2 and H_2 were used for both growth processes, and Ni film served as catalyst particles.

6.1 Structure of ICP VACNFs

The forests of ICP VACNFs grown at normal and low pressure are shown in Fig. 6.1. The ICP VACNFs (normal pressure) were ~ 2-3 μm tall with diameters ranging from 50-100 nm. Low pressure ICP VACNFs had heights of ~ 4 μm, and larger diameters (~ 200 nm). These forests all presented good alignment to the growth substrate.

Fig. 6.2 demonstrates the interior structure of both forests. Both types of nanofibers had a bamboo-like structure with a central hollow channel, with Ni particles located at the tip. Some Ni was trapped in the central channels; this was especially true for normal pressure ICP VACNFs. The spacing between central cross struts was different from nanofiber to nanofiber, and was not a constant even in the same fiber. By high resolution TEM studies, it was evident that the graphitic planes were at an angle to the axis and extended to the fiber surface, forming open edges at the surface (refer to Fig. 6.3 and Fig. 6.4). The spacing between graphitic planes was approximately 0.34 nm, in agreement with that of graphite. Both types of fibers contained quite a few defects, which were more prominent at locations closer to the fiber surfaces, as shown in Fig. 6.3 and 6.4.

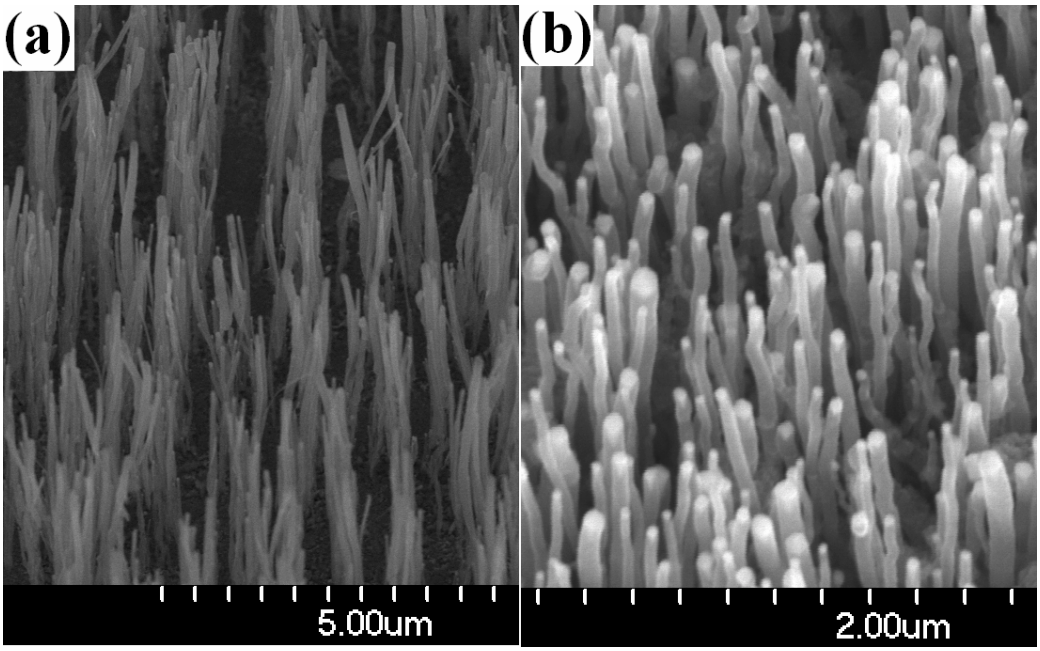

Fig. 6.1 SEM images of ICP VACNFs grown at low pressure (a) and normal pressure (b).

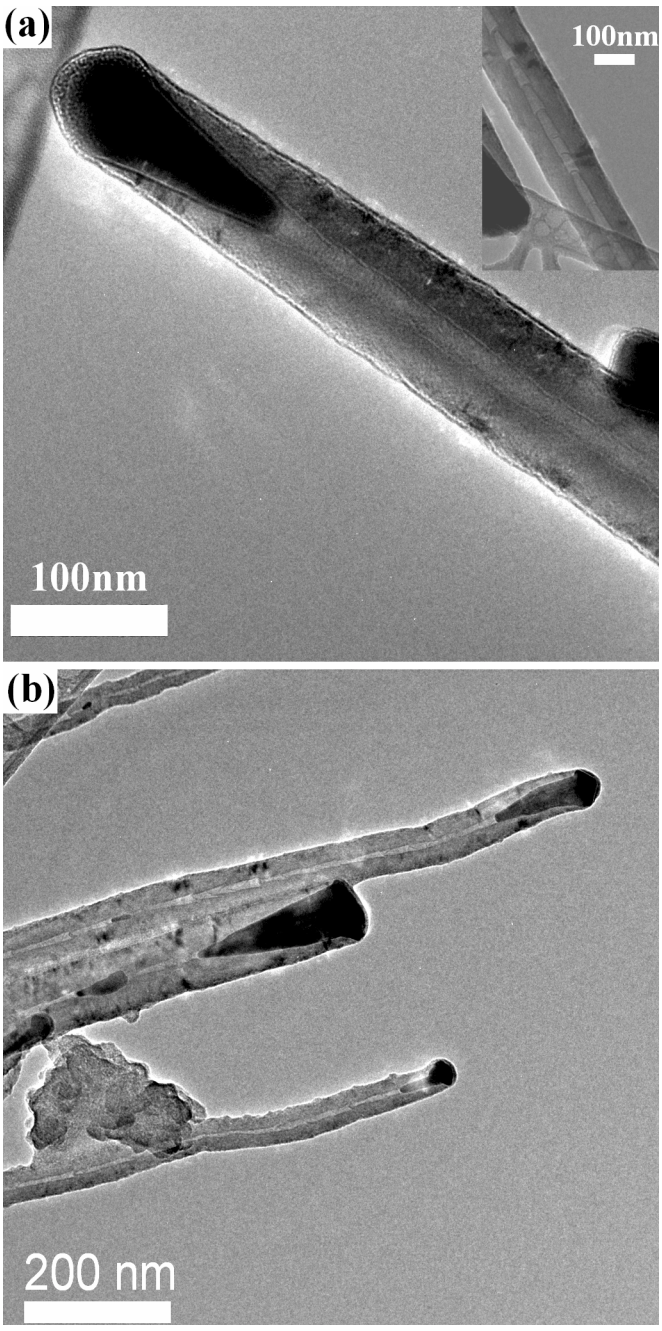

Fig. 6.2 TEM images of ICP VACNFs grown at low pressure (a) and normal pressure (b). Inset in (a) shows the typical bamboo-like structure of low pressure ICP VACNFs.

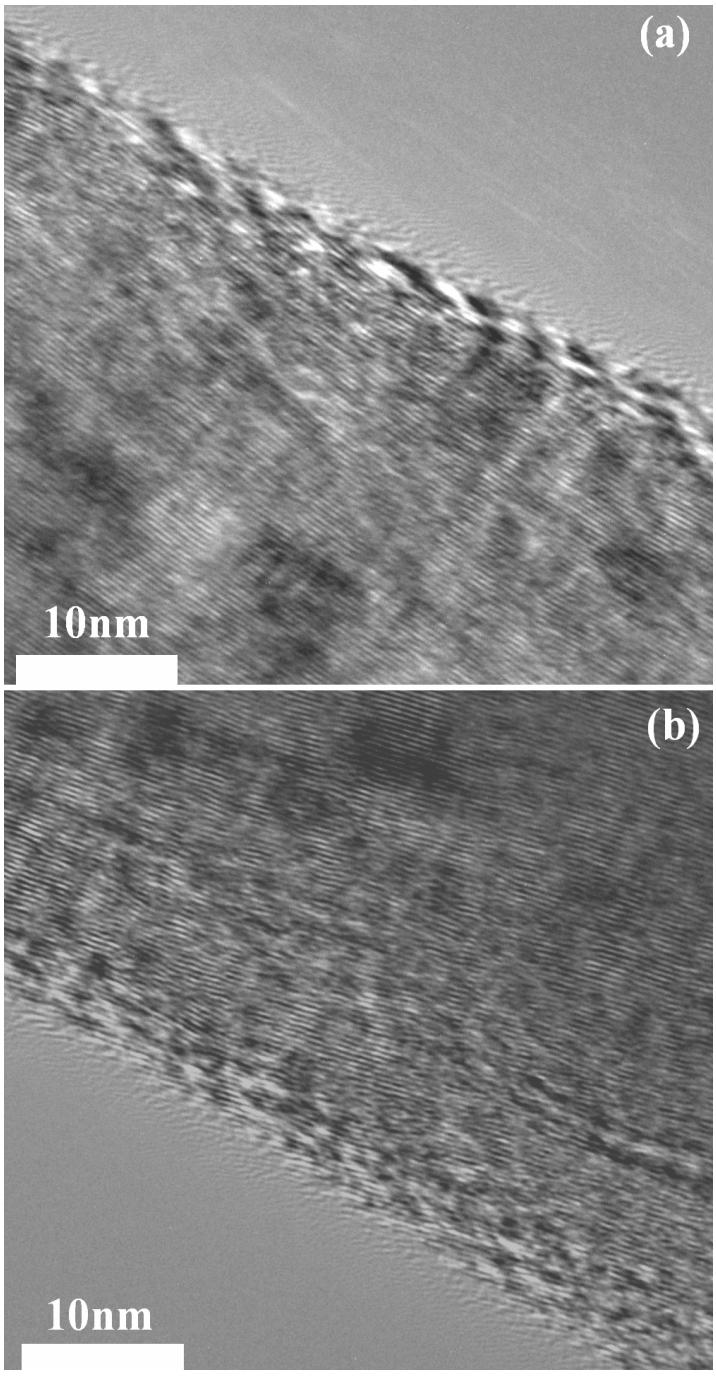

Fig. 6.3 HRTEM images of low pressure ICP VACNFs. The open edges at the nanofiber surface are clearly visible.

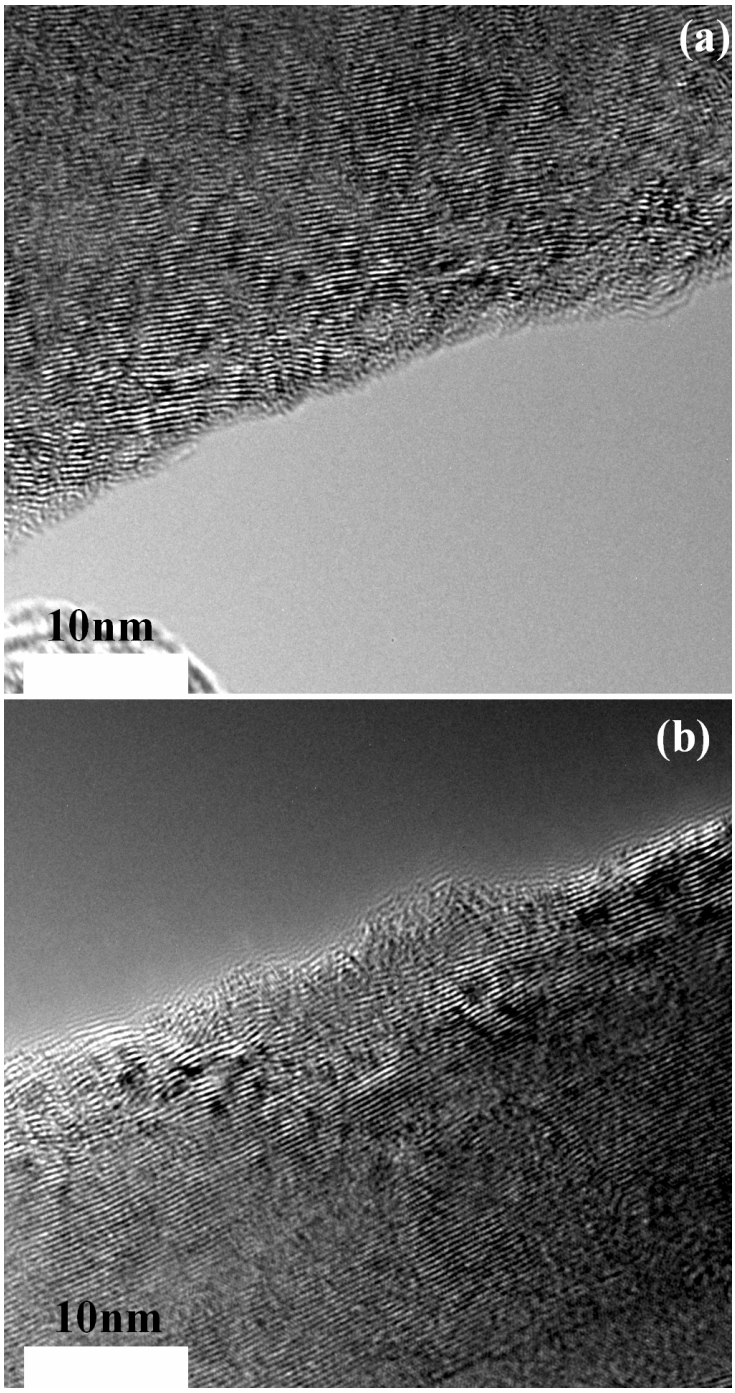

Fig. 6.4 HRTEM images of normal pressure ICP VACNFs.

The whole fiber body, therefore, can be identified by an outer layer with more defects and a more crystalline core. The outer layer may originate from carbon precipitation, whereas the inner core was formed through catalytic growth.

Although sharing many similarities, normal and low pressure ICP VACNFs exhibit many differences. The surface of low pressure nanofibers was free of amorphous carbon, and had open edges extending for quite a long length (up to 5 nm) from the fiber surface, forming a greater angle to the fiber axis than the graphitic planes (refer to Fig. 6.3). By contrast, the normal pressure nanofibers had amorphous carbon occasionally scattered on the fiber surfaces, and as demonstrated by Fig. 6.4, the open edges did not extend very far out of the fiber surfaces. Normal pressure ICP VACNFs were less defective and had better crystalline graphitic planes in the core of these fibers (Fig. 6.5); this perhaps was associated with the higher growth temperature of these nanofibers (900^{o}C).

The major difference of these two types of fibers lay in the shape of the catalyst particles at the nanofiber tips. It resembled the shape of a water drop for the low pressure ICP VACNFs, but was rather like a thumbtack for the normal pressure ones. HRTEM work revealed interesting features of the catalyst particles of the latter. The thumbtack shaped Ni particles had two parts: the cap and the needle (or shaft). The graphitic planes exactly followed the shape of the catalyst at the needle part, as shown in Fig. 6.6 (a). Between the graphitic planes and Ni, there was a region with different lattice fringes from both graphite and Ni (Fig. 6.6 (b), region A), most probably some Ni carbide. Approaching the cap region, the graphitic planes did not extend to surround the Ni cap, but ended in the bottom of the cap (Fig. 6.6 (c)). The cap was covered by the

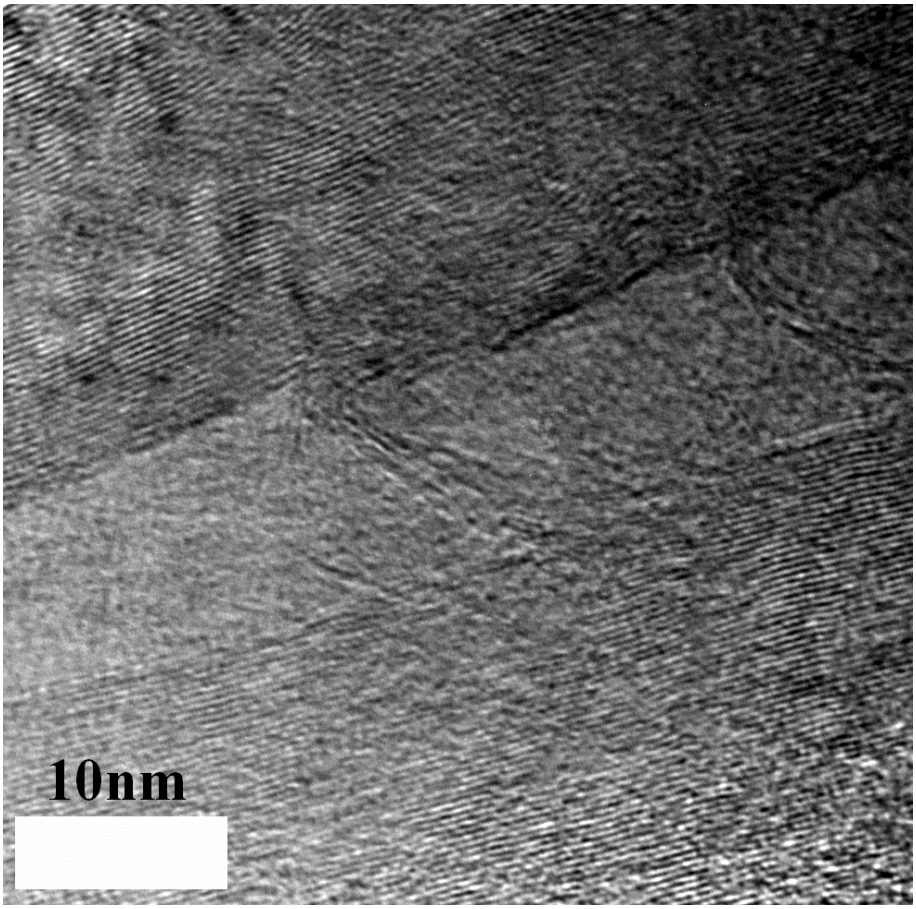

Fig. 6.5 A HRTEM image showing the interior structure of a normal pressure ICP VACNF.

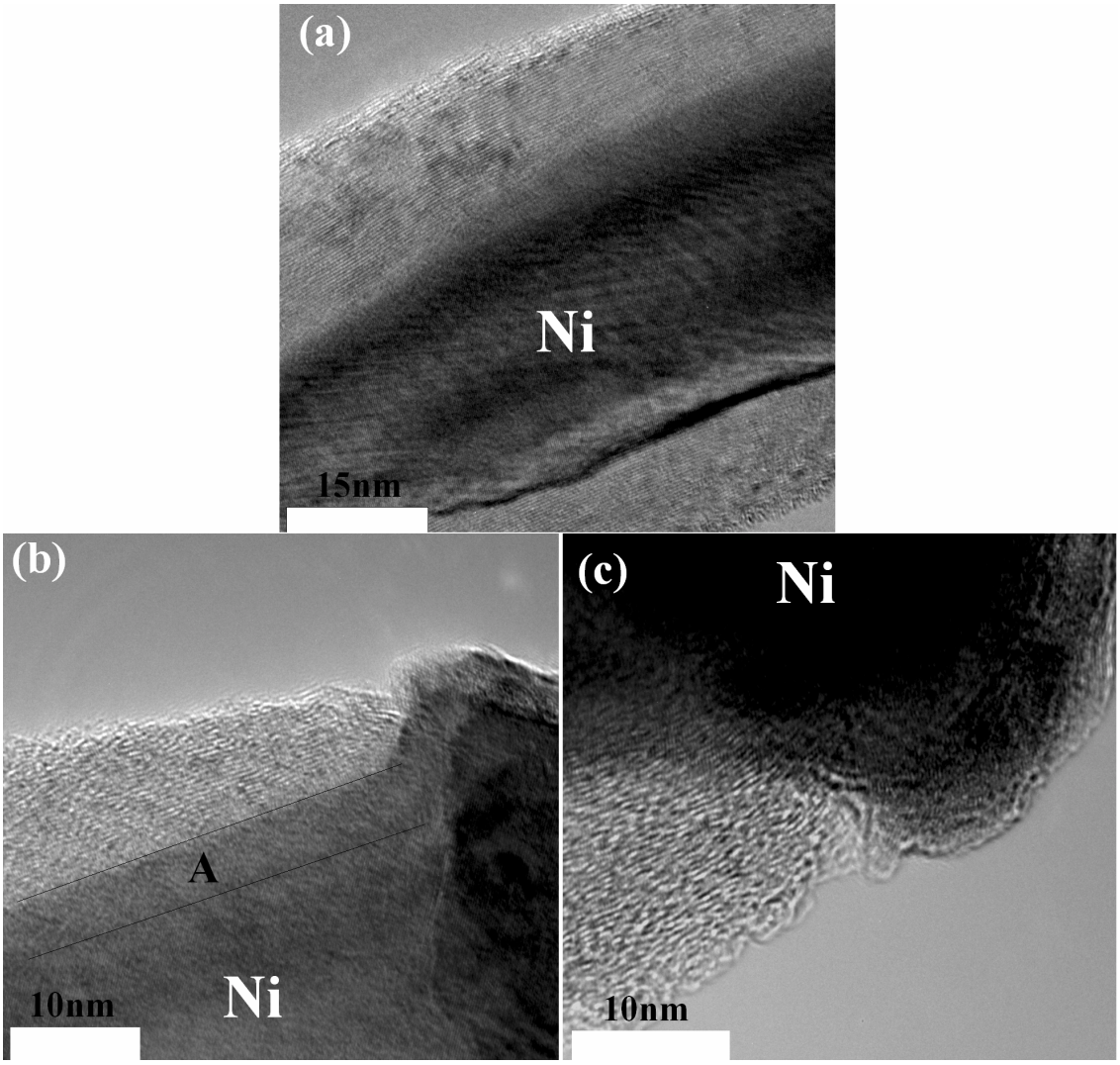

Fig. 6.6 HRTEM images of a normal pressure ICP VACNF tip. (a) At the needle region, the graphitic planes follow the shape of the needle part of Ni. (b) Located between graphitic planes and Ni, region A may be some Ni carbide. (c) Graphitic planes end at the bottom of the cap.

same material as that of region A in Fig. 6.6 (b), and maybe one or two discontinuous graphitic planes. This may imply that the cap of the Ni particle was exposed during the growth process, and that the unknown material was formed when the sample was cooled to room temperature. Why Ni took this particular shape is not clear at this point, perhaps it was related to the buffer layer of catalyst film. With this shape, carbon can diffuse through the cap and reach the flat bottom region of the cap at a relatively fast rate; this may account for the fast growth rate of this nanofiber forest. As for the detail structure around the catalyst particles of low pressure ICP VACNFs, it was similar to that of dc VACNFs with Ni completely encapsulated in graphitic planes, as described previously.

6.2 Composition of ICP VACNFs

EDX results suggested that both types of ICP VACNFs were predominantly made of carbon. For both types of VACNFs, there was very small amount of Si present along the nanofiber body, and Si was richer at the nanofiber edges (Fig. 6.7 and Fig. 6.9). This implies that a small amount of Si became incorporated into the fiber body primarily by very slight sputtering-off of the silicon substrate. Ni was only observed in the nanofiber tips, not along the fiber body, except at the central channel where some Ni particles were trapped. Since Ni caps were most probably exposed during the growth process, as discussed in the last section, this result indicates that there existed only very slight ion bombardment and sputtering-off of the substrate and catalyst materials.

A relatively higher amount of N was also observed along the fiber length, as indicated by the elemental mapping in Fig. 6.8 and Fig. 6.10. As the gases ($C_2H_2/H_2/Ar$)

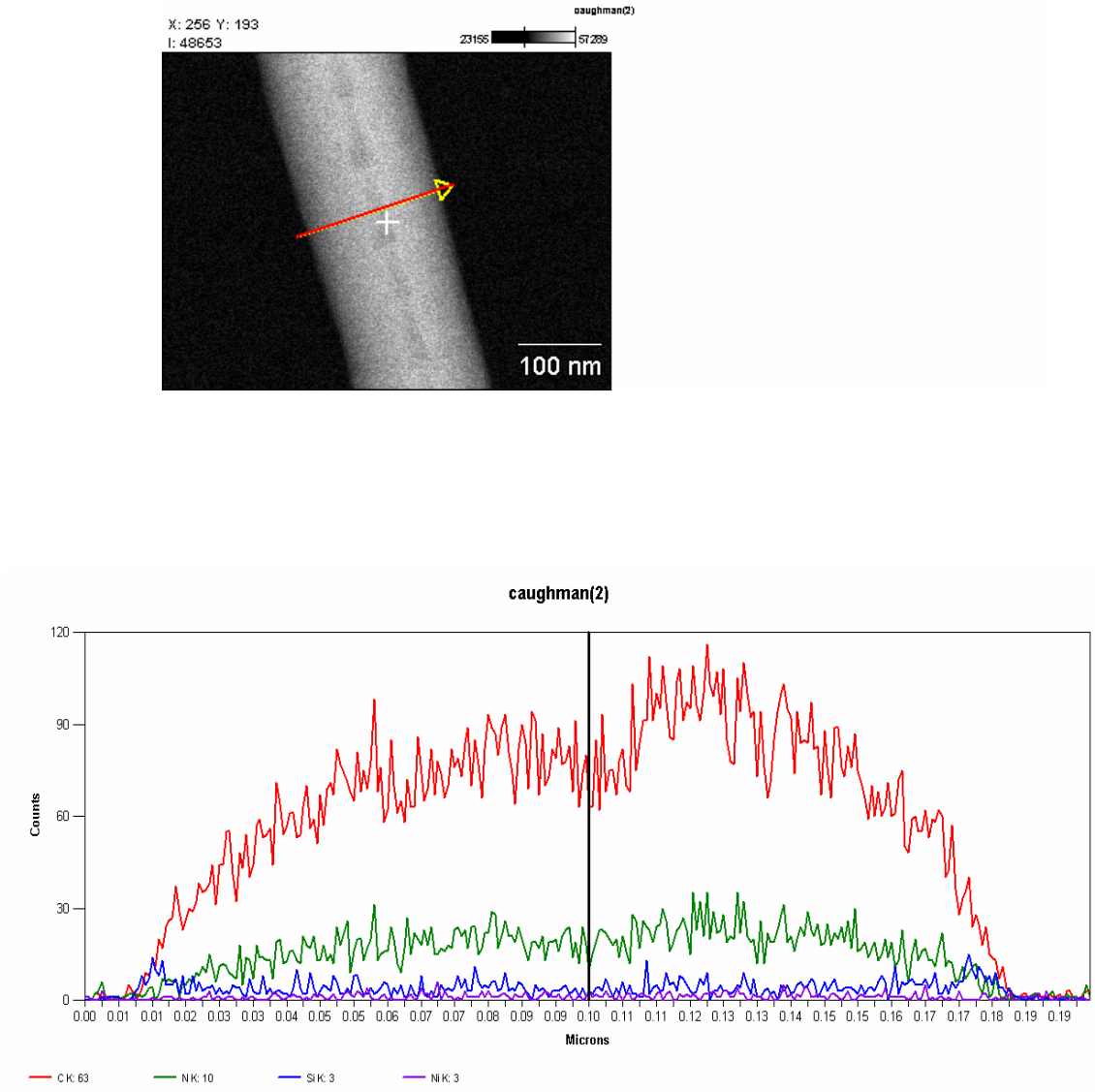

Fig. 6.7 Compositional distribution of C (red), N (green), Si (blue) and Ni (purple) for a ICP VACNF (low pressure).

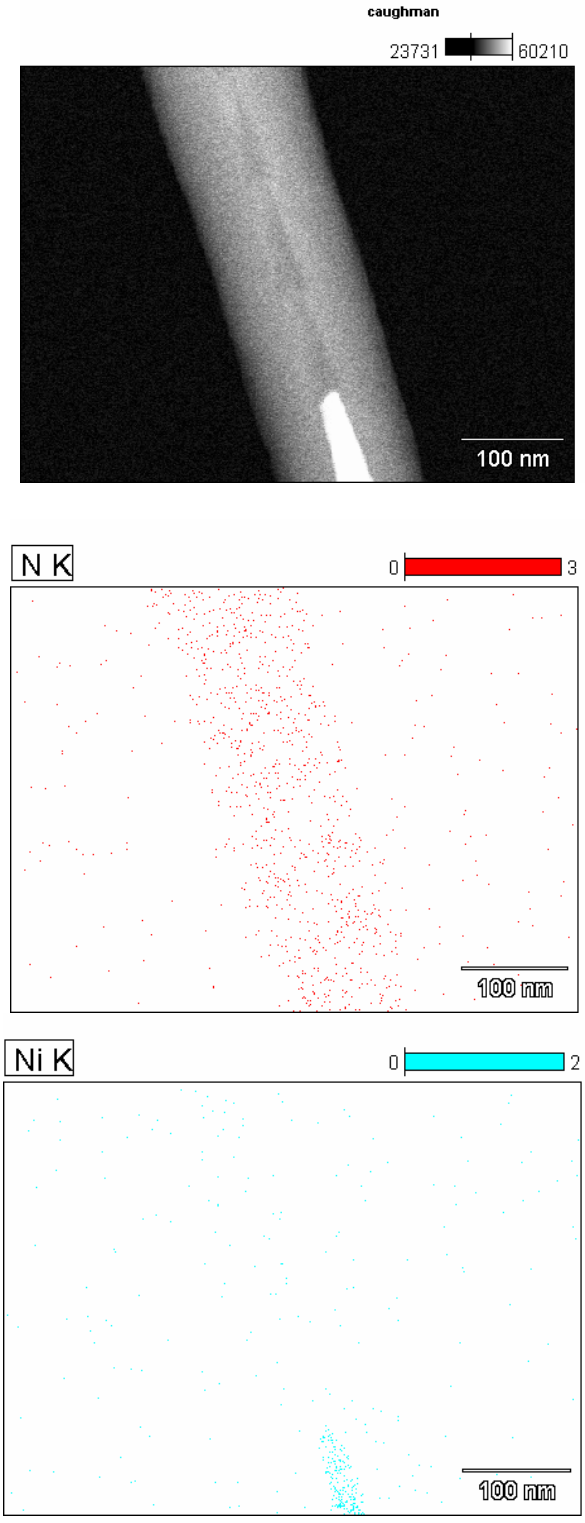

Fig. 6.8 Elemental mapping of N and Ni along ICP VACNFs (low pressure).

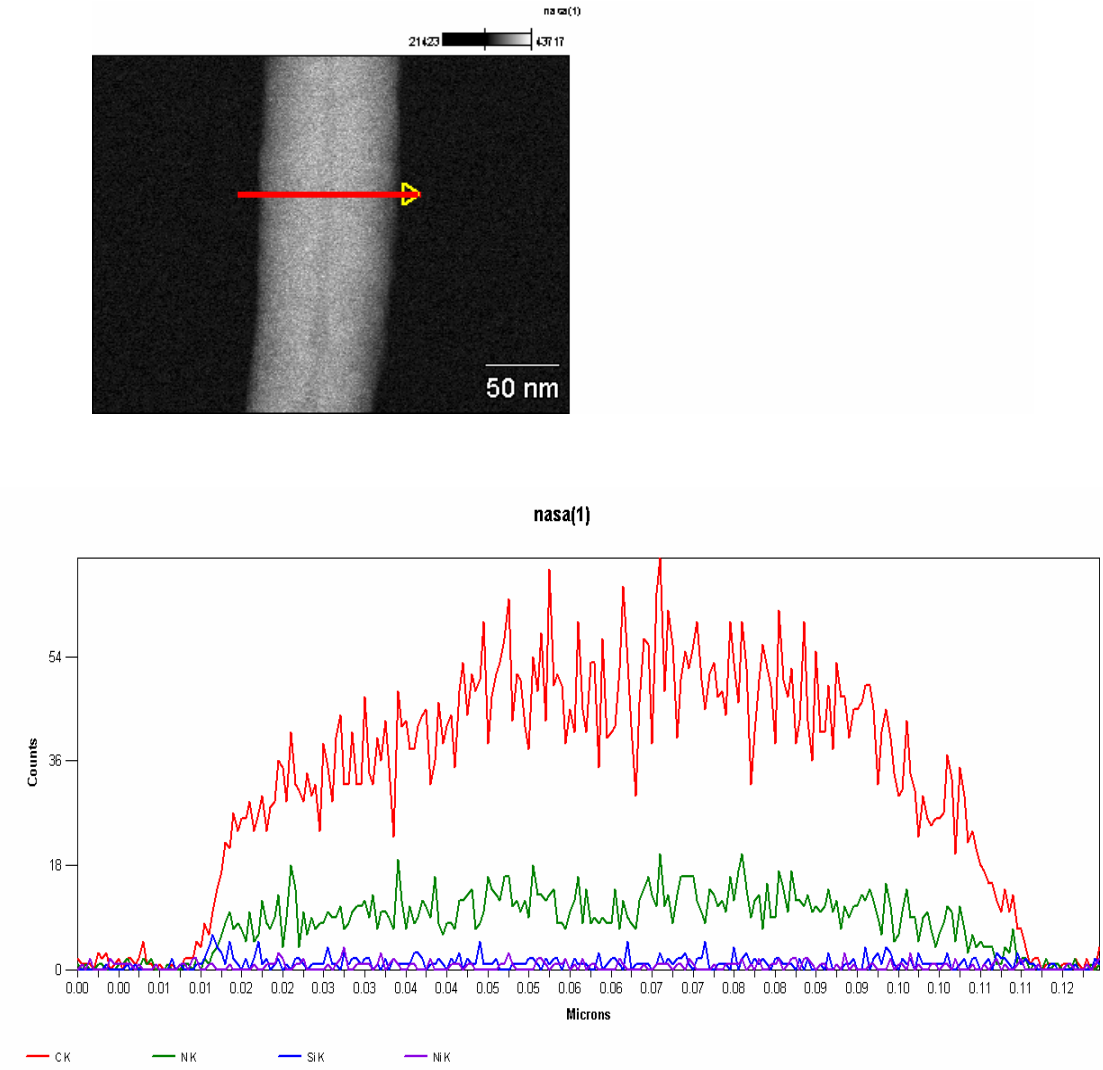

Fig. 6.9 Compositional distribution of C (red), N (green), Si (blue) and Ni (purple) for a ICP VACNF (normal pressure).

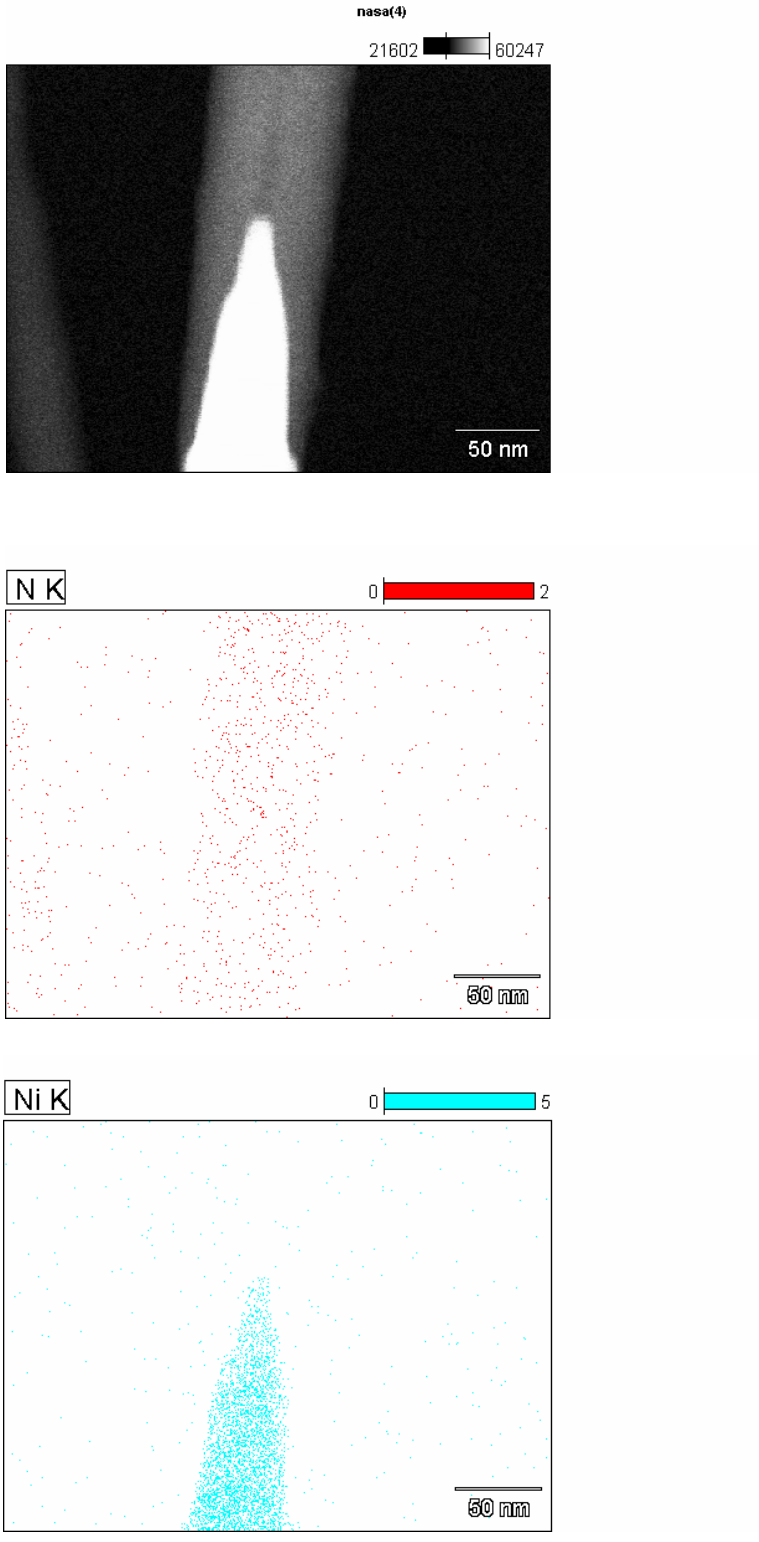

Fig. 6.10 Elemental mapping of N and Ni along ICP VACNFs (normal pressure).

introduced during the growth processes did not contain any nitrogen, it might be absorbed through sample storage in air.

6.3 Charge transport measurements of ICP VACNFs

For both types of ICP VACNFs, only two-probe measurements were performed. Although four electrodes could be patterned on these nanofibers, all attempts to carry out four probe measurements failed.

The electrodes were patterned onto the ICP VACNFs in the same manner as for the dc VACNFs. Prior to the metal deposition, several seconds of O_2 plasma etch was carried out. In this way, ohmic contacts were achieved for both types of ICP VACNFs, between nanofibers and Cd/Au, Ti/Au electrodes.

Fig. 6.11 demonstrates a patterned low pressure ICP VACNF and the corresponding I-V curves between two electrodes. All the I-V curves were linear, and the resistance of these two probe structures was 1 kΩ for an approximately 500 nm long fiber segment. The structure can sustain a current of 0.8 mA, corresponding to a current density on the order of 10^{10} A/m^2. The resistivity can be estimated to be between 10^{-2} to 10^{-3} Ω·cm.

Similar results were obtained for normal pressure ICP VACNFs. The I-V curves were linear for all possible combinations of two electrodes. This particular nanofiber shown in Fig. 6.12 could carry current up to 0.4 mA, which corresponded to a current density of 1.4×10^{11} A/m^2. The resistivity can be estimated to be between 10^{-3} to 10^{-4} Ω·cm.

To check on the gate effects of these nanofibers, the heavily doped Si chip was used as a back gate and gate voltage was applied, but no gate effects were observed for both

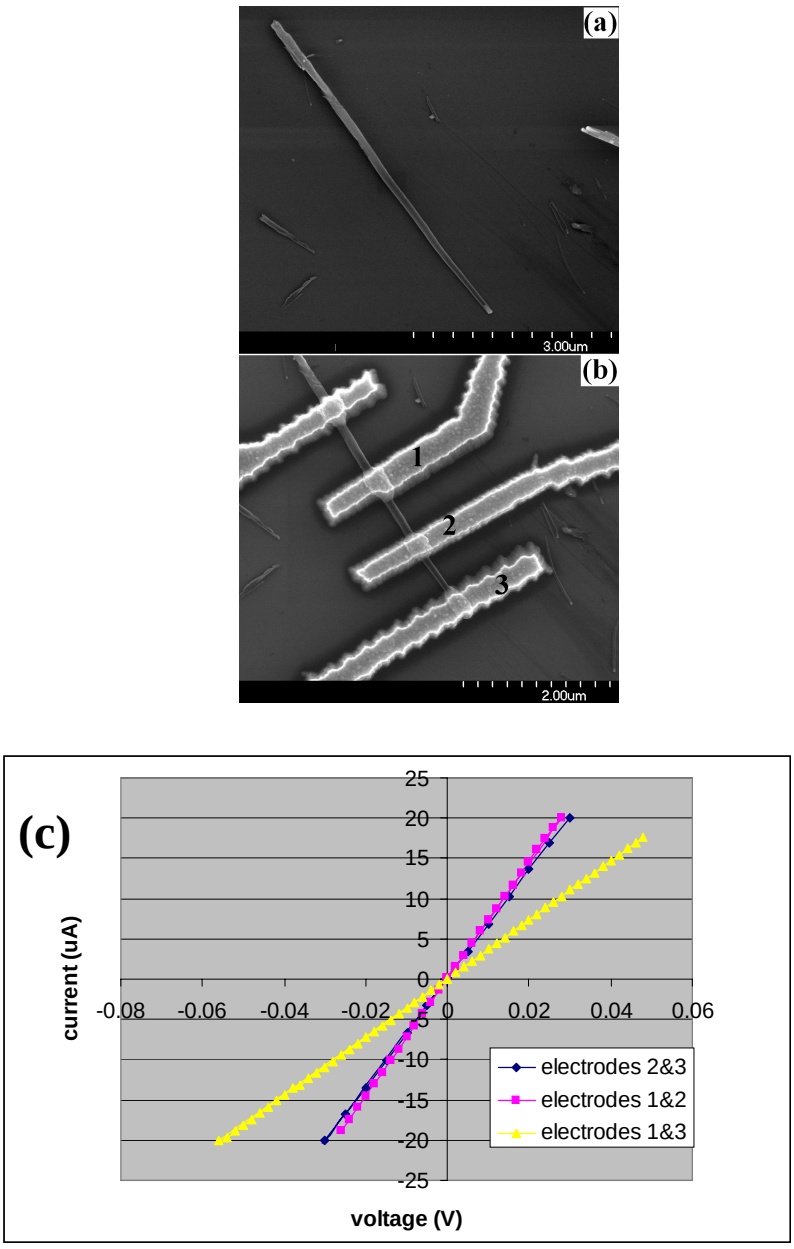

Fig. 6.11 (a)-(b) SEM images of a low pressure ICP VACNF before (a) and after (b) patterned with electrodes (200 nm Ti/Au). The unlabeled electrode had a bad contact with this nanofiber. (c) I-V characteristics measured between two electrodes. Resistance between electrodes 1&2, 2&3, 3&4 was 1.3 kΩ, 1.5 kΩ, and 2.7 kΩ respectively. The contact resistance of contact 2 can be calculated to be ~ 0.05 kΩ.

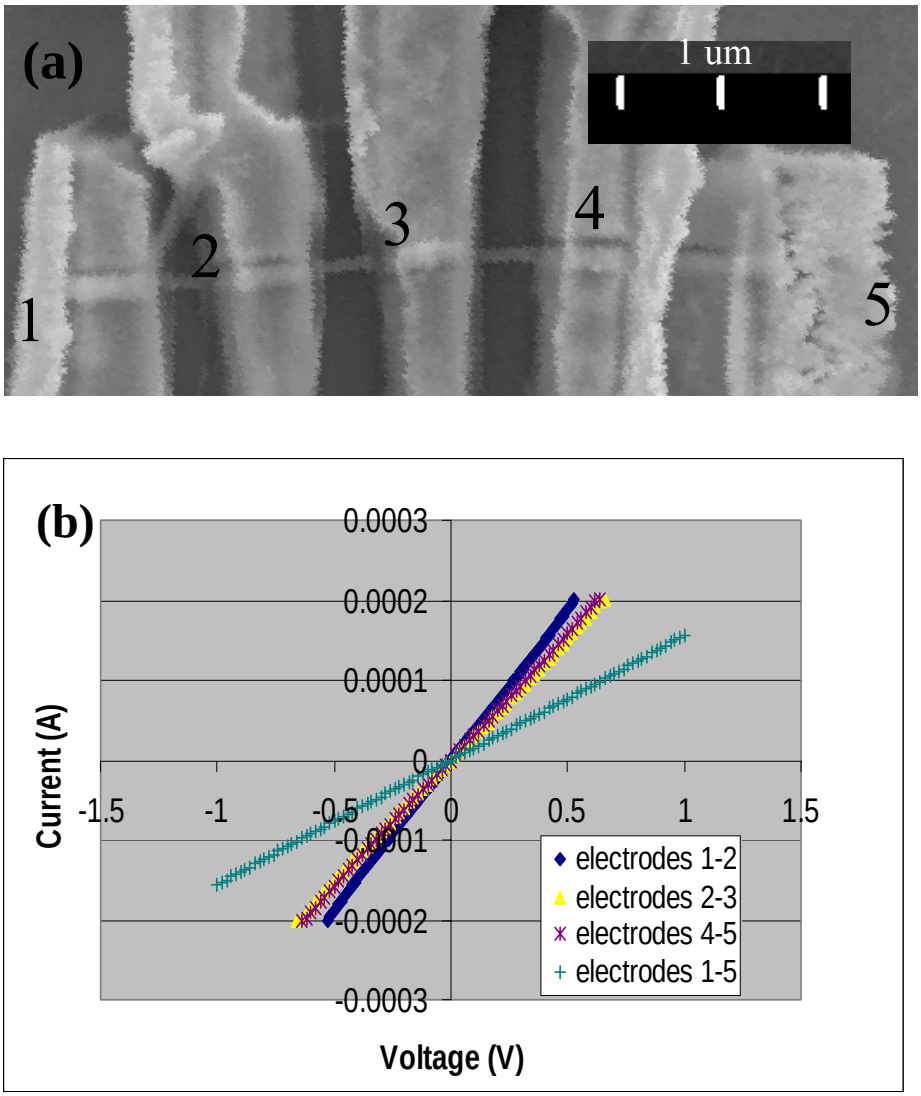

Fig. 6.12 (a) SEM image of a patterned normal pressure ICP VACNF (Cd/Au, 200 nm each). (b) I-V curves measured from (a). The resistance between electrodes 1&2, 2&3, 4&5, 1&5 was 2.8 kΩ, 3.4 kΩ, 3.2 kΩ and 6.6 kΩ respectively.

types of ICP VACNFs.

6.4 Comparison of dc and ICP PECVD VACNFs

6.4.1 Structure

The structure of these three types of nanofibers share many common features. All these VACNFs are composed of graphitic planes which, as presented in this work, form a nonzero angle with the fiber axis. They extend to the nanofiber surface and result in the formation of many open edges. These graphitic planes are discontinuous at many locations, giving rise to many defective regions. These defects are more prominent at locations closer to the fiber surfaces. Two different parts of the fibers can thereby be identified: a more defective outer layer and a more crystalline fiber core. The outer layer may originate from carbon precipitation, whereas the inner core is formed through catalytic growth. The catalyst particles are all located at the nanofiber tips, and some Ni is trapped inside the central part of the nanofibers.

The structural differences of these three types of fibers are also obvious. The dc VACNFs have a herringbone-like structure, but the ICP VACNFs possess a structure more like that of bamboo. There is more entangling and discontinuity of graphitic plane ribbons in the dc VACNFs, and these nanofibers have a more defective structure than the ICP VACNFs. Since the graphitic planes resemble the shape of catalyst particles, at locations close to the central part of dc VACNFs (refer to Fig. 4.2 (b)), the heavy entangling and discontinuity of cross-struts indicates that the Ni particle changed its shape frequently during the growth process. For ICP VACNFs, the structure was more crystalline, took similar shapes at various locations, and the central structure was

continuous most of the time. Therefore, the Ni particle did not vary its shape as frequently as in dc VACNFs.

The reason for shape changing of the Ni particle for dc VACNFs, we propose, was possibly associated with the bombardment of N ions or other ions containing N, which kept sputtering off Ni at the fiber tip. While some Ni was sputtered away from the tip, the total volume of Ni was different so that the Ni particle had to reshape to keep the energy at a minimum. As a result, facets were probably created at certain locations, and the shape of the Ni particle changed.

Additionally, the shape of Ni particles is different for dc VACNFs and normal pressure ICP VACNFs,. Ni particles had a teardrop shape with a flat bottom for dc VACNFs. They were completely encapsulated in the nanofiber tip and surrounded by graphitic planes. But for ICP VACNFs, Ni particles were shaped more like a thumbtack, and the cap was not covered by graphitic planes, but something else (probably Ni carbide). Different shapes of Ni catalyst might affect the diffusion process of carbon in Ni, and the thumbtack shape appears to help achieve a higher growth rate for normal pressure ICP VACNFs. Why Ni took this peculiar thumbtack shape is not clear at this point, but it may be related to the higher growth temperature of this sample (900^{o}C).

6.4.2 Composition

All these VACNFs are predominately made of carbon. The open edges at the nanofiber surfaces allow the absorbance of certain amount of N into the nanofiber body. Although they share these similarities, these nanofibers also exhibit a few differences. The major differences in composition for dc and ICP VACNFs are the content and distribution of Ni

and Si along the fiber body. For dc VACNFs, Ni and Si were distributed along the whole dc VACNF length, with a signal intensity comparable to N (Fig. 4.10). Both Ni and Si had higher peaks in the fiber edges. In contrast to dc VACNFs, Ni was only observed at nanofiber tips and sometimes partially trapped in central channels for ICP VACNFs. The amount of Si was negligibly small. In our opinion, the incorporation of Ni and Si in dc VACNFs is the result of bombardment of N ions or other ions containing N on catalyst particles and the growth substrate. For ICP VACNFs, H was too light to result in considerable sputtering off of Ni.

6.4.3 Charge transport properties

All three types of VACNFs exhibited linear I-V behavior, and no gate effects were observed. The resistivity of dc VACNFs (4.2×10^{-3} Ω·cm) may be the highest among these VACNFs; as for ICP VACNFs, the resistivity was estimated to be in the same order or lower. The VACNF resistivity lies in between that of graphite parallel to the basal plane (4×10^{-5} Ω·cm) and perpendicular to the basal plane (4×10^{-2} Ω·cm) is consistent with a simple model of charge transport where electrons travel mainly from one graphitic plane to another along the length of the nanofiber. Take $\theta = 78^{o}$ and 81^{o} for ICP VACNFs grown at low and normal pressure respectively, as observed in Fig. 6.2, 6.3 and 6.4, this model yields resistivity of 1.7×10^{-3} and 1.0×10^{-3} Ω·cm. These values are in agreement with our experimental results.

Chapter 7 Conclusions and future work

7.1 Conclusions

In this work, charge transport properties have been measured for three types of vertically aligned carbon nanofibers (VACNFs), namely VACNFs grown by direct current PECVD and inductively coupled PECVD grown at both normal pressure and low pressure. The structure and composition of these nanofibers have also been investigated, as the charge transport properties are directly related to them. Particular attention has been paid to direct current VACNFs in this work.

Direct current VACNFs have a highly defective herringbone-like structure with a central hollow region, and the Ni catalyst particles are completely encapsulated at the tip of the fibers. The fiber surface is covered by many open edges of graphitic planes. The fiber body consists of three parts: a 10-15 nm thick graphitic outer layer, cross-struts, and a layer with darker contrast in between. The darker layer most probably forms as a result of carbon precipitation due to supersaturation of carbon in the Ni particles, and thereby possesses a catalytic growth nature. In contrast, the outer layer may originate mainly from precipitation of carbon from glow discharge when a slight excess of acetylene is provided. The formation of wavy nanofibers, which accounts for about one tenth of the whole fiber group, is closely related to the presence of trapped Ni particles in the fiber body.

Compositional studies reveal that C, N, Si, Ni and O are all present in the dc VACNF body. Carbon is the dominant element, and accounts for over 96% of the atomic percentage of the fiber. Nitrogen is the second most prevalent element with an atomic

percentage of over 1%. Silicon and Ni are present and distributed along the entire nanofiber body, but in very small amounts. Oxygen is also present in small amounts. These elements may become incorporated into dc VACNFs through different mechanisms. The presence of a small amount of oxygen might result from storage of the sample in air after growth. Nitrogen can either originate from the ammonia used in the growth process or nitrogen in air due to sample storage. The open edges of the graphitic planes along the fiber length may make it easier for both N and O to be absorbed.

The presence of Ni along the whole VACNF length, though, is first reported in this work for VACNFs grown by dc PECVD. Auger electron spectroscopy results indicate that Ni is primarily located in fiber walls, not in the center catalytic part. Therefore, it can be concluded that Ni becomes incorporated into the fiber body largely through the sputtered-off mechanism from the Ni particle located on the fiber tip. Silicon may get into the fiber body by being sputtered-off from the Si substrate.

After investigating the structure and composition of dc VACNFs, four-probe I-V measurements on individual nanofibers have been conducted. These measurements have been enabled by the fabrication of multiple metal ohmic contacts on individual fibers that exhibited resistance of only a few kΩ. An O_2 plasma reactive ion etch method has been used to fabricate ohmic contacts between the nanofibers and Ag/Au, Cd/Au, and Cr/Au electrodes in addition to Ti/Au electrodes. This method is simple and easy to apply, and has never been reported before by other research groups.

Four-probe measurements demonstrate that dc VACNFs exhibit linear I-V behavior at room temperature, with a resistivity of approximately 4.2×10^{-3} Ω·cm. Gate effect is not observed when the heavily doped Si substrate is used as a back gate. Our measurements

are consistent with a dominant transport mechanism of electrons traveling through intergraphitic planes in the dc VACNFs. The resistivity of these fibers is almost independent of temperature, and the contact resistance increases as temperature decreases.

Further studies reveal that the 10-15 nm thick graphitic outer layer dominates the charge transport properties of dc VACNFs. This is demonstrated by comparison of charge transport properties of as-grown VACNFs and VACNFs with the outer layer partially removed by oxygen plasma reactive ion etch. The metallic behavior of the fibers does not vary as this outer layer becomes thinner, but displays a drastic shift to a rectifying behavior when this layer is completely stripped away from some regions of the nanofiber. Our results imply that by varying the extent of graphitization and structure of the outer layer, it may be possible to achieve controllable charge transport properties for dc VACNFs.

VACNFs grown by inductively coupled PECVD at normal and low pressure have similar structure as dc VACNFs. They possess a more defective outer layer and a crystalline inner core. The composition of these fibers is predominately carbon,,and Ni is not observed along the fiber body. Nitrogen is present as a result of sample storage in air. Two-probe charge transport measurements indicate linear I-V behavior, and the resistivity of both types of inductively coupled PECVD grown VACNFs (normal and low pressure) is on the order of 10^{-3} to 10^{-4} Ω·cm, which agrees with the transport mechanism of electrons traveling through intergraphitic planes. It is possible that the outer layers of these inductively coupled PECVD grown VACNFs also play a key role in the charge transport measurements of these fibers.

7.2 Future work

Future work can be carried out in several directions. Firstly, the growth mechanisms of dc VACNFs can be further clarified if carbon nanofibers grown for different periods of time can be studied in detail through TEM and EDX. For example, we can examine the carbon nanofibers just after these fibers begin to emerge from the substrate; after putting these nanofibers back to growth for about 10 minutes, we can scratch off some nanofibers and reexamine their interior structure, especially the outer layer. The compositional information can also be obtained during this step. It will be interesting to know whether Ni presents at this stage. This process can be repeated until the growth of nanofibers finally stops. In this way, the structural and compositional development of nanofibers can be discerned step by step in a time-resolved fashion. The mechanisms of how nickel, silicon and nitrogen become incorporated into the fiber body may be understood better.

Secondly, more work needs to be done on the charge transport measurements of VACNFs as the composition of these nanofibers, especially of the outer layer, varies. The resistivity of nanofibers can be a function of the angle between the graphitic planes and the fiber axis, as discussed preliminarily in this dissertation. The resisitivity may also depend on the composition of the outer layer, particularly silicon and nitrogen.

The temperature dependence measurements of resistivity for inductively coupled PECVD grown VACNFs can also be helpful to shed more light on the charge transport mechanisms of the VACNF group. Our results indicate that at room temperature these IC VACNFs exhibit linear I-V behavior; as temperature changes, these behaviors can be radically different. Other mechanisms for charge transport properties, such as the thermal activation, may also play a role.

List of references

List of references

1. Adapted from http://www.chem.ox.ac.uk/icl/heyes/structure_of_solids/Lecture1/Lec1.html.
2. B.T. Kelly, Physics of graphite, Applied Science, 1981.
3. H. Dai, Acc. Chem. Res., 35, 1035 (2002).
4. J.W. Mintmire, B.I. Dunlap, and C.T. White, Phys. Rev. Lett., 68, 631 (1992).
5. J.W. Mintmire and C.T. White, Carbon, 33, 893 (1995).
6. S. Tans, A. Verschueren, and C. Dekker, Nature, 393, 49 (1998).
7. R. Martel, T. Schmidt, H.R. Shea, T. Hertel, and Ph. Avouris, Appl. Phys. Lett., 73, 2447 (1998).
8. Ph. Avouris, Acc. Chem. Res., 35, 1026 (2002).
9. A. Bachtold, M.S. Fuhrer, S. Plyasunov, M. Forero, E.H. Anderson, A. Zettl, P.L. McEuen, Phys. Rev. Lett., 84, 6082 (2000).
10. S. Frank, P. Poncharal, Z.L. Wang, and W.A. de Heer, Science, 280, 1744 (1998).
11. Topics Appl. Phys. 80, edited by M. S. Dresselhaus et al., Springer-Verlag Berlin Heidelberg, 2001, pp329-391.
12. J. Appenzeller, R. Martel, Ph. Avouris, H. Stahl, and B. Lengeler, Appl. Phys. Lett., 78, 3313 (2001).
13. Carbon Nanotubes: Synthesis, Structure Properties and Applications, Edited by M. S. Dresselhaus et al.; Springer-Verlag: Berlin, 2001.
14. Z. Yao, C.L. Kane, and C. Dekker, Phys. Rev. Lett., 84, 2941 (2000).

15. P. Poncharal, C. Berger, Y. Yi, Z.L. Wang, and W.A. de Heer, J. Phys. Chem. B, 106, 12104 (2002).
16. D. Mann, A. Javey, J. Kong, Q. Wang, and H. Dai., Nano Lett., 3, 1541 (2003).
17. P.G. Collins, M.S. Arnold, and P. Avouris, Science, 292, 706 (2001).
18. V. Derycke, R. Martel, J. Appenzeller, and Ph. Avouris, Nano Lett., 1, 453 (2001).
19. J. Kong, C. Zhou, E. Yenilmez, and H. Dai, Appl. Phys. Lett., 77, 3977 (2000).
20. M. Bockrath, Phys. Rev. B, R10606 (2001).
21. V. Derycke, R. Martel, J. Appenzeller, and Ph. Avouris, Appl. Phys. Lett., 80, 2773 (2002).
22. J.-Y. Park, S. Rosenblatt, Y. Yaish, V. Sazonova, H. Üstünel, S. Braig, T. A. Arias, P. W. Brouwer, and P. L. McEuen, Nano Lett., 4, 517 (2004).
23. M. Kociak, A. Yu. Kasumov, S. Gueron, B. Reulet, I.I. Knodos, Yu. B. Gorbatov, V.T. Volkov, L. Vaccarini, and H. Bouchiat, Phys. Rev. Lett., 86, 2416 (2001).
24. Z. K. Tang, L. Zhang, N. Wang, X. X. Zhang, G. H. Wen, G. D. Li, J. N. Wang, C. T. Chan, and P. Sheng, Science, 292, 2462 (2001).
25. T.W. Ebbesen, H.J. Lezec, H, Hiura, J.W. Bennett, H.F. Gharmi, and T.Thio, Nature, 382, 54 (1996).
26. V.I. Merkulov, D.H. Lowndes, Y.Y. Wei, G. Eres, and E. Voelkl, Appl. Phys. Lett., 76, 3555 (2000).
27. V. I. Merkulov, M. A. Guillorn, D. H. Lowndes, M. L. Simpson, and E. Voelkl, Appl. Phys. Lett., 79, 1178 (2001).

28. V. I. Merkulov, D. K. Hensley, A. V. Melechko, M. A. Guillorn, D. H. Lowndes, and M. L. Simpson, J. Phys. Chem. B, 106, 10570 (2002).
29. V. I. Merkulov, A. V. Melechko, M. A. Guillorn, D. H. Lowndes, and M. L. Simpson, Appl. Phys. Lett., 80, 476 (2002).
30. V. I. Merkulov, A. V. Melechko, M. A. Guillorn, D. H. Lowndes, and M. L. Simpson, Chem. Phys. Lett., 350, 381 (2001).
31. L. Zhang, A. V. Melechko, V. I. Merkulov, M. A. Guillorn, M. L. Simpson, D. H. Lowndes, and M. J. Doktycz, Appl. Phys. Lett., 81, 135 (2002).
32. L. Delzeit, I. McAninch, B.A. Cruden, B. Chen, J. Han, and M. Meyyappan, J. Appl. Phys., 91, 6027 (2002).
33. M.S. Dresselhaus, G. Dresselhaus, K. Sugihara, I.L. Spain, H. A. Goldberg, Graphite fibers and filaments., Springer Berlin, Heidelberg, 1988.
34. L. Zhang, D. Austin, V.I. Merkulov, A.V. Meleshko, K.L. Klein, M.A. Guillorn, D.H. Lowndes, and M. L. Simpson, Appl. Phys. Lett., 84, 3972 (2004).
35. S.-B. Lee, K.B.K. Teo, M. Chhowalla, D.G. Hasko, G.A. J. Amaratunga, W.I. Milne, and H. Ahmed, Microelectronic Engi., 61-62, 475 (2002).
36. J. Li, R. Stevens, L. Delzeit, H.T. Ng, A. Cassell, J. Han, M. Meyyappan, Appl. Phys. Lett., 81, 910 (2002).
37. X.J. Yang, M. A. Guillorn , D. Austin , A.V. Melechko ,H. Cui, H. M. Meyer III, V. I. Merkulov, J.B.O. Caughman, D. H. Lowndes, and M. L. Simpson, Nano Lett., 3, 1751 (2003).
38. Y. C. Choi, Y. M. Shin, Y. H. Lee, B. S. Lee, G.-S. Park, W. B. Choi, N. S. Lee, and J. M. Kim, Appl. Phys. Lett., 76, 2367 (2000).

39. J.B.O. Caughman, L.R. Baylor, M.A. Guillorn, V.I. Merkulov, D.H. Lowndes, and L.F. Allard, Appl. Phys. Lett., 83,1207 (2003).
40. Y. Saito, Carbon, 33, 979 (1995).
41. V.V. Kovalevski and A.N. Safronov, Carbon, 36, 963 (1998).
42. V. I. Merkulov, A. V. Melechko, M. A. Guillorn, D. H. Lowndes, and M. L. Simpson, Appl. Phys. Lett., 79, 2970 (2001).
43. S. Fan, M. G. Chapline, N. R. Franklin, T. W. Tombler, A. M. Cassell, and H. Dai, Science, 283, 512 (1999).
44. Nanometer Pattern Generation System, Manual, Version 1.0, 2000.
45. M. A. McCord, and M. J. Rooks, SPIE Handbook of Microlithography, Micromachining and Microfabrication, edited by P. Rai-Choudhury, SPIE, Washington, DC 1997, pp158.
46. P.J. de Pablo, E. Graugnard, B. Walsh, R.P. Andres, S. Datta, and R. Reifenberger, Appl. Phys. Lett., 74, 323 (1999).
47. J. Lee, C Park, J. Kim, J. Park, and K. Yoo, J. Phys. D: Appl. Phys., 33, 1953 (2000).
48. D. Mann, A. Javey, J. Kong, Q. Wang, and H. Dai, Nano Lett., 3, 1541 (2003).
49. Y. Zhang, T. Ichihashi, E. Landree, F. Nihey, and S. Iijima, Science, 285, 1719 (1999).
50. A. Bachtold, M. Henny, C. Terrier, C. Strunk, C. Schonenberger, J.-P. Salvetat, J.-M. Bonard, and L. Forro, Appl. Phys. Lett., 73, 274 (1998).

Vita

Lan Zhang received her bachelor's degree in Materials Science and Engineering from Tsinghua University, China in 1995. Four years later, she earned her master's degree in Materials Science from the University of Houston based on her SEM/TEM studies in superconductor tapes. She worked at the IBM SEM laboratory at East Fishkill, New York in 2000, and started her PhD study at the University of Tennessee in 2001.

She has published first-authored papers on Applied Physics Letters, Philosophical Magazine Letters, and other journals. She also coauthored more than 15 papers and a book chapter.